

Emir Hodžić, Dipl.-Ing. BSc

**“Experimental and numerical investigations on the influence of  
natural aging on the formability of Al-Mg-Si alloy blanks”**

**DISSERTATION**

zur Erlangung des akademischen Grades

Doktor der technischen Wissenschaften

eingereicht an der

**Technischen Universität Graz**

Betreuer

Univ.-Prof. Dipl.-Ing. Dr.techn. Christof Sommitsch

Institute of Materials Science, Joining and Forming

## EIDESSTATTLICHE ERKLÄRUNG

Ich erkläre an Eides statt, dass ich die vorliegende Arbeit selbstständig verfasst, andere als die angegebenen Quellen/Hilfsmittel nicht benutzt, und die den benutzten Quellen wörtlich und inhaltlich entnommen Stellen als solche kenntlich gemacht habe. Das in TUGRAZonline hochgeladene Textdokument ist mit der vorliegenden Dissertation identisch.

---

Datum

---

Unterschrift

This page was left blank intentionally.

## Acknowledgments

The present work was conducted during my stay as a university project assistant at the Institute of Materials Science, Joining and Forming at Graz University of Technology. Therefore, I would like to express my sincere gratitude to the head of the institute Mr. Univ.-Prof. Dipl.-Ing. Dr. techn. Christof Sommitsch for supervising me during my PhD. Since I spent my time at the Research Group of Lightweight and Forming Technologies, I am deeply grateful to the group leader Mr. Ass.Prof. DDDipl.-Ing. Dr. mont. Josef Domitner for unlimited support, extensive discussions, and unconditional guidelines, that led to the successful accomplishment of the project and the thesis.

I am deeply grateful to the members of the workshop, Mr. Heinz Karl Fasching and Mr. Nino Müllner, for their support in sample preparation and the conduction of experimental tryouts. I would especially like to thank Mr. Arash Shafiee Sabet for performing the tribological tests and having daily discussions with me, which surely improved the quality of this work.

I would like to offer my special appreciation to the company AMAG (Ranshofen, Austria) for financial support and material delivery. In particular, a special thanks goes to the members of AMAG Rolling GmbH Ms. Angela Thum, Mr. Christian Matters, and Mr. Werner Fragner.

Moreover, I would like to extend my sincere thanks to my colleagues Mr. Besim Helić, Ms. Zahra Silvayeh, Ms. Eva Keinrath, Mr. Peter Auer, and Mr. Andreas Drexler for their help and insightful comments and suggestions.

Finally, but most importantly, I would like to thank my parents, Sead and Besima, my wife Merima, and my brother Semir and his family for their encouragement and moral support.

## Abstract

Minimizing CO<sub>2</sub> emissions is one of the highest priorities of the automotive industry. An efficient way to reduce vehicle mass and fuel consumption is lightweighting through the installation of aluminum components instead of conventional steel components. Aluminum and its alloys are well known for their exceptional corrosion resistance, good strength-to-weight ratio, and good formability. Al-Mg-Si alloy blanks are frequently used for the production of deep-drawn car outer panels. However, the processability of these blanks is limited to 6 months due to alteration of material properties during the storage at room temperature (natural aging). Afterwards, blanks are classified as expired. This work investigates 4 commercial 1 mm-thick Al-Mg-Si alloy blanks differing in chemical composition or lubrication. The formability and the formability-related mechanical properties were investigated within 1-18 months of natural aging. The formability was experimentally and numerically investigated using two deep-drawing tools, i.e., (i) a cross-shaped tool with an open die and (ii) a complex tool with a closed die. The mechanical properties were analyzed by performing the tensile tests and the bendability by performing the plate-bending tests. It was found that increasing the Si and Mg content positively affected the formability of Al-Mg-Si blanks, but the effect of Si was more beneficial. However, the formability enhancement was even more notable by applying an alternative lubricant, which reduced the friction during the deep drawing operation. The obtained formability did not correlate with the tensile ductility nor with  $n$ -values but rather with the planar anisotropy  $\Delta r$ . During the investigated period of natural aging, the yield strength of each of the blanks increased by 19.5-24.5% due to clustering and growth of Mg and Si co-clusters. The kinetic of natural aging was more progressive in Mg-rich alloy blanks and Si only affected the initial yield strength. However, the strengthening did not affect the tensile ductility,  $r$ -values, and formability but  $n$ -values and the bendability decreased constantly during natural aging. A direct correlation was found between  $r$ -values and formability since both remained constant within the natural aging time. The clustering phenomenon likely did not affect the crystallographic texture, which primarily determines  $r$ -values. Moreover, the bendability deterioration was primarily due to decreasing  $n$ -values, which led to the narrowing of the plastic deformation zone and earlier cracking. Moreover, the TriboForm friction models for numerical forming simulations were generated based on the results from the pin-on-plate friction tests. A very good agreement between experimentally and numerically formed components was observed in terms of strains, thinning, forming force, and springback. The application window (shelf-life) can be extended to periods longer than 6 months for investigated Al-Mg-Si alloy blanks. This would have ecological and economical benefits through reduction of scrap rate and avoidance of intense recycling. However, the bendability necessary for hemming operations should be monitored.

## Kurzfassung

Reduzierung der CO<sub>2</sub>-Emissionen gehört zu den höchsten Prioritäten in der Automobilindustrie. Ein erfolgreicher Weg zur Reduzierung der Fahrzeugmasse und des Kraftstoffverbrauchs ist der Leichtbau durch den Einsatz von Aluminiumbauteilen statt konventionellen Stahlbauteilen. Aluminium und seine Legierungen sind bekannt für ihre Korrosionsbeständigkeit, ihr gutes Festigkeit-Gewicht-Verhältnis und ihre Umformbarkeit. Insbesondere Bleche aus Al-Mg-Si-Legierungen werden häufig zur Herstellung tiefgezogener Außenhautbauteile verwendet. Allerdings ist die Verarbeitbarkeit dieser Legierungen aufgrund der Veränderung der Materialeigenschaften während der Kaltauslagerung auf Raumtemperatur nur auf 6 Monate begrenzt. Anschließend werden die Bleche als abgelaufen eingestuft. Diese Arbeit untersucht 4 kommerzielle 1 mm-dicke Bleche aus Al-Mg-Si-Legierungen, die sich in der chemischen Zusammensetzung oder Schmierung unterscheiden. Die Umformbarkeit und die umformbarkeitsbezogenen mechanischen Eigenschaften wurden innerhalb von 1–18 Monaten der Kaltauslagerung untersucht. Die Umformbarkeit wurde experimentell und numerisch mit zwei Tiefziehwerkzeugen untersucht, (i) mit einem kreuzförmigen Werkzeug mit offener Matrize und (ii) mit einem komplexen Werkzeug mit geschlossener Matrize. Die mechanischen Eigenschaften wurden mittels Zugversuchen und die Biegeeigenschaften mittels Plättchenbiegeversuchen analysiert. Es wurde festgestellt, dass sich eine Erhöhung des Si- und Mg-Gehalts positiv auf die Umformbarkeit auswirkt, jedoch war die Rolle des Si-Gehalts wichtiger. Allerdings konnte die Anwendung des alternativen Schmiermittels die Reibung während des Tiefziehens verringern und die Umformbarkeit zusätzlich verbessern. Die erhaltene Umformbarkeit hing nicht direkt mit der Zugduktilität oder  $n$ -Werten zusammen, sondern vielmehr mit der planaren Anisotropie  $\Delta r$ . Während der Kaltauslagerung erhöhte sich die Streckgrenze der Bleche aufgrund von Bildung und Wachstum von gemischten Mg/Si Clusters um 19,5–24,5%. Die Verfestigung war progressiver bei Mg-reichen Legierungen. Die Variation des Si-Gehalts wirkte sich nur auf die initiale Festigkeit aus. Allerdings hatte das Clustering keinen Einfluss auf die Zugduktilität,  $r$ -Werte und die Umformbarkeit, verringerte jedoch  $n$ -Werte und die Biegebarkeit. Es wurde ein direkter Zusammenhang zwischen  $r$ -Werten und der Umformbarkeit festgestellt, da beide während der Kaltauslagerung konstant blieben. Das Clustering hatte keinen wesentlichen Einfluss auf die kristallographische Textur, die  $r$ -Werte bestimmt. Darüber hinaus war der Abfall der Biegebarkeit hauptsächlich auf die sinkenden  $n$ -Werte zurückzuführen, die zu einer Verengung der plastischen Umformzone und folglich zu einer früheren Rissbildung führten. Außerdem wurden die TriboForm-Reibungsmodelle für numerische Umformsimulationen auf Basis der Ergebnisse aus den experimentellen Reibversuchen erstellt. Es wurde eine sehr gute Übereinstimmung zwischen experimentell und numerisch geformten Bauteilen hinsichtlich Formänderungen, Ausdünnung, Umformkraft und Rückfederung festgestellt. Dementsprechend kann das Anwendungsfenster (Haltbarkeit) der untersuchten Al-Mg-Si-Legierungen auf Zeiträume größer als 6 Monaten verlängert werden. Dies könnte ökologische und ökonomische Vorteile durch eine Reduzierung der Ausschussrate und die Vermeidung intensiven Recyclings haben. Allerdings sollte die für Falzarbeiten erforderliche Biegebarkeit überwacht werden.

# Table of content

1	Introduction .....	1
2	State of the art .....	4
2.1	Aluminum alloys .....	4
2.1.1	Tempering designation of wrought aluminum alloys .....	6
2.1.2	Al-Mg-Si alloys for outer panel application .....	7
2.1.3	Aging of Al-Mg-Si alloys .....	8
2.2	Experimental material characterization .....	11
2.2.1	Mechanical material properties .....	11
2.2.2	Strain hardening exponent ( $n$ -value) .....	14
2.2.3	Anisotropy ( $r$ -value).....	14
2.2.4	Yield surface .....	16
2.2.5	Stack compression test .....	17
2.3	Deep drawing fundamentals .....	18
2.3.1	Introduction to deep drawing .....	18
2.3.2	Failures .....	21
2.3.3	Role of the blankholder .....	23
2.3.4	Forming Limit Curve (FLC) .....	24
2.4	Hemming .....	26
2.5	Tribology in deep drawing .....	28
3	Methods .....	33
3.1	Materials .....	33
3.2	Uniaxial tensile test .....	34
3.3	Stack compression test.....	35
3.4	Bendability.....	36
3.5	Forming limits .....	37
3.6	Formability .....	38
3.6.1	A-Tool .....	38
3.6.2	CS-Tool .....	39
3.7	3D optical scanning .....	40
3.8	Pin-on-plate tribometer.....	41
4	Finite element (FE) forming simulations .....	43

4.1	Simulation model.....	43
4.2	Material model.....	45
4.3	Friction model.....	46
5	Material characterization.....	48
5.1	Uniaxial tensile test .....	48
5.1.1	Tensile strength .....	48
5.1.2	Tensile ductility .....	50
5.1.3	Strain hardening .....	53
5.1.4	Anisotropy .....	55
5.1.5	Discussion mechanical parameters.....	57
5.2	Generation of flow curves using stack compression test.....	58
5.3	Influence of NA on the flow curves of Al-Mg-Si blanks .....	59
5.4	Tensile behavior of Al-Mg-Si blanks at elevated strain rates .....	61
6	Formability of Al-Mg-Si alloy blanks.....	65
6.1	Influence of chemical composition, lubrication and natural aging on the formability....	65
6.1.1	Influence of the blank alignment, surface roughness and lubricant amount on the formability .....	69
6.1.2	Formability discussion .....	74
6.2	Influence of NA on the bendability .....	75
6.3	Influence of NA on the forming limits .....	77
7	Pin-on-plate friction tests .....	79
8	Numerical forming simulation .....	81
8.1	TriboForm friction model.....	81
8.2	Forming simulation at low forming velocity of 10 mm/s.....	82
8.2.1	Strains.....	82
8.2.2	Forming forces .....	86
8.2.3	Thickness.....	89
8.2.4	Surface comparison .....	93
8.3	Influence of variable flow curves on the formability of Al-Mg-Si alloys.....	95
8.4	Numerical forming simulations at high forming velocity of 100 mm/s .....	97
9	Conclusions .....	98
10	Outlook.....	100
11	References .....	101

List of figures .....	109
List of tables .....	113

## List of parameters and abbreviations

Symbol	Unit	Description
$a$	-	Hocket-Sherby parameter
$A$	mm <sup>2</sup>	Actual cross-section of tensile test sample
$A_0$	mm <sup>2</sup>	Initial cross-section of tensile test sample
$A_{80}$	-	Fracture strain measure using extensometers with length of 80 mm
$A_g$	-	Uniform strain
$b$	mm	Actual width of tensile test sample
$b_0$	mm	Initial width of tensile test sample
$b_{plate}$	mm	Width of plate for plate bending test
$C$	MPa	Swift parameter
$D_{blank}$	mm	Diameter of circular blanks
$D_{disk}$	mm	Disk diameter
$D_{max}$	mm	Maximum drawing depth
$D_{punch}$	mm	Diameter of punch for cup-shaped tool
$D_{roll}$	mm	Roller diameter
$E$	GPa	Young's modulus
$F$	N	Tensile force
$F_{comp}$	N	Compression force
$F_F$	N	Frictional force
$F_{max}$	kN	Maximum blankholder force for forming of crack-free components
$F_N$	N	Normal force
$h_0$	mm	Initial height of stacked disks
$k$	-	Natural aging kinetics
$k_f$	MPa	True stress
$l$	mm	Actual length of tensile test sample
$L$	mm	Roller distance
$l_0$	mm	Initial length of tensile test sample
$l_{plate}$	mm	Length of plate for plate bending test
$M$	-	Barlat89 parameter
$m$	-	Swift parameter
$p$	-	Hocket-Sherby parameter
$p_{HD}$	MPa	Hydrodynamic pressure
$p_{HS}$	MPa	Hydrostatic pressure
$p_N$	MPa	Normal pressure
$r_0$	-	Normal anisotropy in rolling direction
$r_{45}$	-	Normal anisotropy in diagonal direction
$r_{90}$	-	Normal anisotropy in transverse direction
$R_a$	μm	Arithmetic average surface roughness based on line measurement
$r_f$	mm	Flanging radius
$r_m$	-	Average normal anisotropy
$R_m$	MPa	Ultimate tensile strength

$R_{p0.2}$	MPa	Yield strength measured at 0.2% of plastic strain
$r_{tip}$	mm	Punch tip radius
$s$	mm	Actual thickness of tensile test sample
$S$	mm	Punch distance
$s_0$	mm	Initial thickness of tensile test sample
$S_a$	$\mu\text{m}$	Average surface roughness based on surface measurement
$t_{NA}$	h	Natural aging time
$v$	mm/s	Velocity
$x$	mm	Compression distance
$\alpha$	$^\circ$	Bending angle
$\alpha_{maxl}$	$^\circ$	Maximum bending angle
$\beta_0$	-	Drawing ratio
$\gamma$	-	Weighting factor
$\Delta r$	-	Planar anisotropy
$\varepsilon$	-	Engineering strain
$\varepsilon_0$	-	Swift parameter
$\varepsilon_{pl}$	-	Plastic engineering strain
$\lambda$	-	Specific film thickness
$\mu$	-	Coefficient of friction
$\sigma$	MPa	Actual engineering stress
$\sigma_0$	MPa	Engineering stress calculated for initial cross-section area
$\sigma_{1h}$	MPa	Yield strength after 1 hour of natural aging
$\sigma_{ini}$	MPa	Hocket-Sherby parameter
$\sigma_n$	MPa	Normal stress
$\sigma_r$	MPa	Radial stress
$\sigma_{sat}$	MPa	Hocket-Sherby parameter
$\sigma_t$	MPa	Tangential stress
$\sigma_y$	MPa	Yield strength after specific time of natural aging
$\tau$	Pa	Shear stress
$\varphi$	-	True strain
$\varphi_1$	-	Major strain
$\varphi_2$	-	Minor strain
$\varphi_{pl}$	-	True plastic strain

<b>Abbreviation</b>	<b>Description</b>
AA	Artificial Aging
BHF	Blankholder Force
CAD	Computer Aided Design
CAGR	Compound Annual Grow Rate
CF model	Constant Friction model
CoF	Coefficient of Friction
CS-Tool	Cross-Shaped Tool
DD	Diagonal Direction
DIC	Digital Image Correlation
EDT	Electric Discharged Texture
EV	Electric Vehicle
FE	Finite Element
FLC	Forming Limit Curve
FLD	Forming Limit Diagram
GP-Zone	Guinier-Preston Zone
MF	Mill Finish
NA	Natural Aging
PA	Pre-aging
RD	Rolling Direction
SSSS	Supersaturated Solid Solution
TD	Transverse Direction
TEM	Transmission Electron Microscopy
TF model	TriboForm model

# 1 Introduction

Fulfilling the legislative demands on CO<sub>2</sub> emissions is an ongoing challenge for the automotive industry. Decreasing the car weight reduces simultaneously fuel consumption and CO<sub>2</sub> emissions. An efficient way to implement this concept is lightweighting through the utilization of aluminum alloys instead of conventional steels. Benedyk [1] stated that a weight reduction of 10% could improve the fuel savings for 5-6%. Moreover, Ostermann [2] reports that the application of aluminum blanks for chassis parts instead of steel blanks may result in 100-140 kg weight loss. Despite having a lower density than steel alloys, aluminum alloys still exhibit exceptional corrosion resistance, excellent strength-to-weight ratio, good formability, and weldability. Thus, the utilization of aluminum alloys in car design massively increased over the past decades. The average content of aluminum for the production of passenger cars increased from 37 kg in the year 1973 to 126 kg in the year 2007. Figure 1 shows that the tendency of increased utilization of aluminum in European passenger cars continued also after the year 2006. Hirsch [3] reported that the average aluminum content in European cars was 140 kg in the year 2012. Nowadays, the average aluminum content in passenger cars is slightly above 200 kg. However, a projected expectation is about 256 kg of aluminum per passenger car by the year 2030. A similar scenario was also observed in North America, where almost 1/3 of produced aluminum is used for the transportation industry. The average aluminum content in North American passenger cars is expected to be about 258.5 kg by the year 2030. It has to be noted that the average vehicle curbside weight has not significantly increased since 2005 and it is expected to slightly decrease in the future. [3–9]

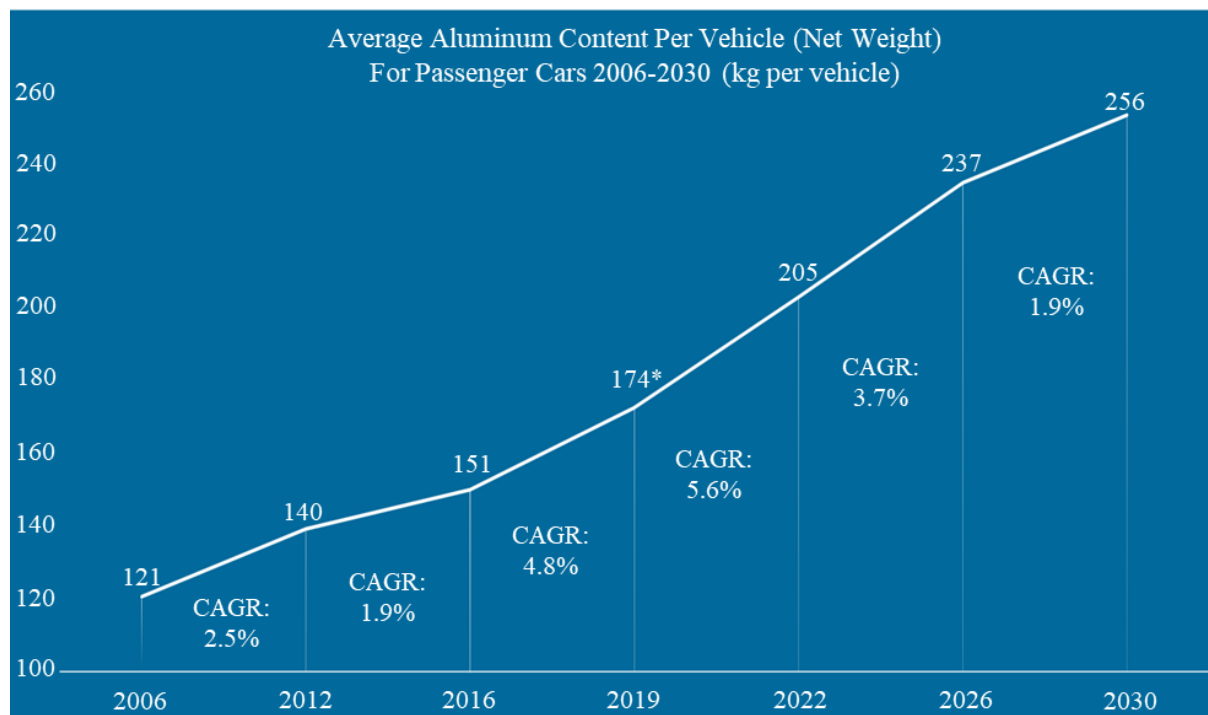


Figure 1 Average aluminum content for European passenger cars [10]

The average aluminum content of aluminum in European passenger cars was 205 kg in the year 2022. The highest share of about 60% belongs to castings whereas about 22% of aluminum components are made of blanks. Extrusions are making about 13% and the forgings about 5%. However, a steady increase for each product type is expected by the year 2030. Compound annual growth rates (CAGR) of 2.1%, 3.5%, 5.6%, and 0.6% are projected for castings, blanks, extrusions, and forgings, respectively. The increasing share of electric vehicles (EV) on the car market is notable shaping the aluminum content in future cars. The number of casting components in the area of powertrain, transmission, and driveline is decreasing. However, this is overcompensated by new cast components for EV, large and mega castings for body-in-white and subframes so an increase in the total weight of aluminum components is expected. Increasing utilization of aluminum blanks is mainly due to ballistic protection of the batteries, cooling plates, and weight reduction goals. An increased application for extruded components is expected for battery pack housing, body-in-white, and brakes. A minor increase in forging components may be expected in the area of the chassis. [10]

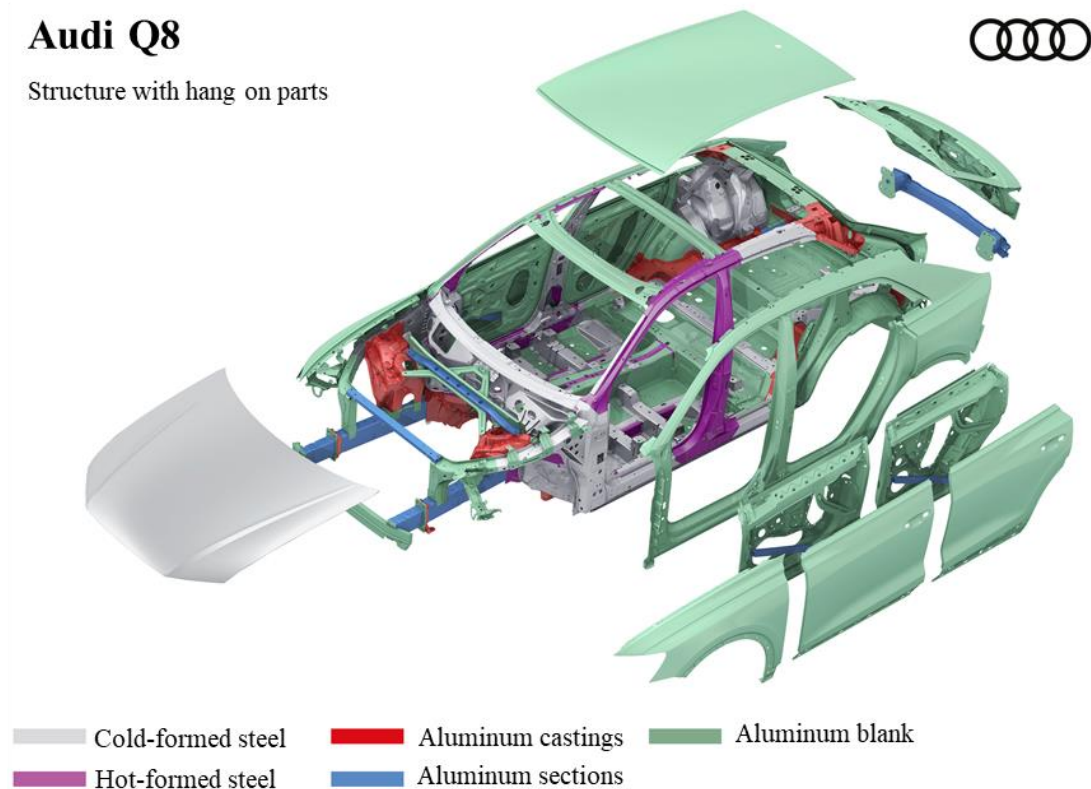


Figure 2 An example of successful implementation of aluminum components in passenger car design [11]

Figure 2 shows an example of the successful implementation of aluminum components in a passenger car. The potential for reducing the vehicle mass is immense considering numerous components that can be produced using aluminum blanks. In particular, car outer panels having

enormous potential are of utmost interest for the automotive industry. These components are typically produced by deep drawing of Al-Mg-Si alloy blanks. However, the shelf-life of these blanks is frequently limited to 6 months due to natural aging (NA), afterwards, these blanks are classified as expired. Extending the shelf-life would reduce scrap and prevent intensive recycling, which would have economic and ecological benefits. Yet, some information about the influence of NA on the formability and formability-related material properties is still missing. Thus, the focus of this work is an experimental and numerical investigation of the formability limits of Al-Mg-Si alloy blanks. The potential alteration of the formability and formability-related parameters was tracked during NA. Moreover, this work investigated the influence of main alloying elements Mg and Si on the formability and strengthening during NA. Pin-on-plate friction tests were performed and the influence of lubrication was analyzed. Based on the results from the friction tests, advanced friction models were generated for improving the accuracy of numerical investigations on the prediction of forming limits.

## 2 State of the art

### 2.1 Aluminum alloys

A favorable combination of mechanical properties made aluminum one of the most used metallic materials. It can be used in the food industry as drink cans or kitchen foils, in the transport industry as car door panels or engine parts but as well in construction engineering as structural parts. The wide application of aluminum alloys is primarily due to impressive strength-to-weight ratio. Despite having the density of  $2.7 \text{ g/cm}^3$  and Young's modulus of 70 GPa (approximately 1/3 of the values for steel) the tensile strengths up to 800 MPa can be achieved by appropriate alloying and application of strengthening mechanism. The processability of aluminum alloys is wide so aluminum components may be found in different forms such as stampings, extrusions, castings, forgings and other machined components. Moreover, aluminum alloys are well known for their exceptional corrosion resistance. A thin, self-renewable aluminum-oxide layer is formed on the surface of aluminum components, that prevents the further oxidation of material. By the reason of good thermal and electrical conductivity, aluminum alloys are often utilized for heat-exchangers and conducting wires. [1,2,12,13].

Aluminum alloys are divided into two groups: wrought and casting alloys. Due to immense differences in material properties of these two alloy groups, separate designation systems were established for each of the groups. A four-digit system is used for designating the wrought aluminum alloys. The first digit refers to primary alloying element or elements and the following digits represent the alloy variation. Following wrought aluminum alloy series are defined: [14]

- 1xxx: Almost pure aluminum with the aluminum content higher than 99%. These alloys are often utilized in chemical and electrical fields due to their high thermal and electrical conductivity.
- 2xxx: Copper (Cu) is primary alloying element. Very high strength-to-weight ratio makes these alloys decent for structural and aeronautic components. Precipitation hardening is commonly applied for reaching the necessary strength. Small amounts of magnesium (Mg) and tin (Zn) can be found.
- 3xxx: Up to 1.5% of manganese (Mn) can be found in alloys of this series. Strength increase of 20% may be achieved compared to 1xxx series. These alloys can be used for architectural applications.
- 4xxx: Up to 12% of main alloying element silicon (Si) can be added to this alloy series. Relatively high amount of silicon decreases the temperature range for melting without influencing the brittleness. Therefore, these alloys are generally used as brazing alloys.
- 5xxx: Magnesium (Mg) is the main alloying element of this series. The components made of this alloy series are characterized with moderate to high strength, good corrosion resistance and weldability. These components can be used as inner panels in passenger cars.
- 6xxx: Main alloying elements in this group of alloys are magnesium (Mg) and silicon (Si). This series is used in the production of car outer panels and extruded components.
- 7xxx: Primary added alloying element in these alloys is zinc (Zn) in amounts of 1-8%. Secondary added alloying elements such as magnesium (Mg) or copper (Cu) or chromium

- (Cr) can improve some of the mechanical material properties. This series is characterized with the highest strength applicable for airframe structures and highly stressed components.
- 8xxx: Alloy from this series may contain various alloying elements such as lithium (Li), tin (Sn) or iron (Fe). Al-Fe-V-Si alloys showed improved performance at higher temperatures. High potential for future applications is seen in Al-Li alloys having low density and high stiffness.
- 9xxx: Future alloys.

In general, wrought aluminum alloys have comparatively lower strength than steel grades. Strengthening mechanisms are playing an important role for achieving a good strength-to-weight ratio of wrought aluminum alloys. Precipitation hardening is essential heat treatment method for most of the wrought series but inapplicable to each of it. In fact, only 2xxx, 6xxx, 7xxx and some of 8xxx (\*) are heat treatable. Remaining wrought aluminum alloys from 1xxx, 3xxx, 4xxx and some of 8xxx series are not heat-treatable so the typical strengthening mechanism for these alloys is strain hardening. An overview about principal alloying elements, strengthening methods and range of tensile strength is summarized in Table 1. [13]

Table 1 Basic information about wrought aluminum alloys

Wrought aluminum series	Type of alloy composition	Strengthening mechanism	Tensile strength range [MPa]
1xxx	Al	Strain hardening	70-175
2xxx	Al-Cu(-Mg)	Heat treatment	170-520
3xxx	Al-Mn(-Mg)	Strain hardening	140-280
4xxx	Al-Si	Strain hardening	105-350
5xxx	Al-Mg	Strain hardening	140-380
6xxx	Al-Mg-Si	Heat treatment	150-380
7xxx	Al-Zn(-Mg)	Heat treatment	380-620
8xxx	Al-Li-Cu-Mg	Heat treatment*	280-560

Cast aluminum alloys are designated by a three-digit system followed by a decimal value, that relates to the casting limits. The first digit refers to primary alloying element and the following two digits refer to ingot composition. The overview about the primary alloying elements is shown in Table 2. The heat treatable cast aluminum alloys are the alloys from 2xx.x, 3xx.x and 7xx.x series whereas 6xx.x series is unused. [13]

Table 2 Main alloying elements of cast aluminum alloys

Cast aluminum series	1xx.x	2xx.x	3xx.x	4xx.x	5xx.x	7xx.x	8xx.x
Main alloying elements	-	Cu	Si (-Cu-Mg)	Si	Mg	Zn (-Mg)	Sn

### 2.1.1 Tempering designation of wrought aluminum alloys

Tempering of wrought aluminum alloys is described as follows [15]:

- As manufactured – no special treatment was applied on these types of alloys.
- O: Annealed – highest ductility but the lowest strength.
- H: Strain hardened – alloyed strengthened by strain hardening. Two or three digits follow the letter H in designation for describing the quantity of applied strain and eventual post-processes such as annealing, stabilizing or painting.
- T: Heat treatment – this group of alloys is typically strengthened by precipitation hardening method with subsequent natural or artificial aging (AA). Natural aging refers to material storage at room temperature whereas artificial aging refers to material storage at elevated temperatures.

Some of frequently applied heat treatments of aluminum alloys are shown in Table 3. Solution heat treatment or solutionizing refers to quenching of aluminum alloys after reaching the supersaturated solid solution (SSSS). If subsequent aging is conducted at room temperature, material temper condition is designated as T4. However, if the aging treatment is conducted at elevated temperature, the material temper condition is designated as T6. These two temper conditions are the most important in production of car outer panels. Forming of these components is usually executed in T4 condition. Subsequently, AA is performed afterwards for reaching the required strength in T6 condition. [15]

Table 3 The most frequent tempering conditions of aluminum alloys

Temper	SHT	Controlled stretching	Stain hardening	NA	AA	Overaging	Extrusion
T1				X			
T3	X		X	X			
T4	X			X			
T5					X		X
T6	X				X		
T651	X	X				X	
T76	X					X	
T8	X		X				

### 2.1.2 Al-Mg-Si alloys for outer panel application

Aluminum alloys of 6xxx series are also known as Al-Mg-Si alloys. On a microscopic scale, Al-Mg-Si alloys with high purity consists of primary  $\alpha$ -phase ( $\alpha$ -Al) and intermetallic  $Mg_2Si$   $\beta$ -phase.  $\beta$ -phase is a strengthening phase for precipitation hardening with the highest solubility of 1.9 wt.% at 583.5 °C, which decreases to 0.08 wt.% at 200 °C. The combined amount of main alloying elements Mg and Si in commercial Al-Mg-Si alloys (6xxx series) is 1-2 wt.%. These alloys have in general lower strength compared to alloys from 2xxx and 7xxx series; however, they still own good corrosion resistance, weldability, machinability, and formability. In the automotive industry, Al-Mg-Si alloy blanks are extensively used for the production of car outer panels. These components additionally require good bendability and exceptional surface quality, which may be an issue for other aluminum alloys like 5xxx series. Namely, surface defects such as flow figures can be observed at components formed using blanks from 5xxx series. Thus, these types of blanks are primarily used for non-visible inner panels. Al-Mg-Si alloy blanks are free of flow figures and have a less roping tendency, which makes them favorable for outer panel application. A comparison between 4 commercial alloys from 5xxx and 6xxx series is shown in Figure 3. The advantage of Al-Mg-Si alloys is better surface quality and buckling strength. Other material properties such as corrosion resistance, weldability, and formability are comparatively similar. Car outer panels are typically formed in deep drawing operations with subsequential hemming operations. Forming operations are performed in T4 temper condition prior to paint baking, i.e., artificial aging, for reaching peak strength in T6 temper condition. Hemming operations are used for bonding the outer panels to the inner components. Thus, exceptional bendability of blanks used for the production of outer panels is also required. The European automotive industry has used AA6016 for the last 25 years for outer panel application, whereas the North American automotive uses mainly AA6111. Additional important representatives of this group of alloys are AA6181A, AA6014, AA6009, and AA6022. Aside from car outer panels, Al-Mg-Si alloys are also used in the automotive industry for the production of structural components from rather thicker blanks or in the form of extrusions. [2,3,12,13,16]

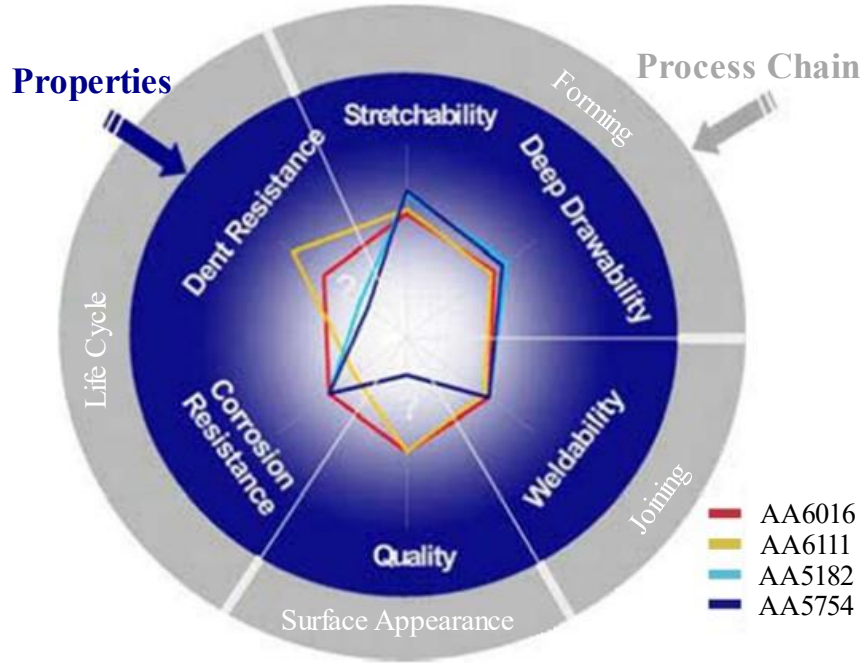


Figure 3 A comparison between 4 commercial aluminum alloy blanks used for production of car outer panels [3]

### 2.1.3 Aging of Al-Mg-Si alloys

Figure 4 schematically illustrates the processing of car outer panels made of Al-Mg-Si alloy blanks. Solutionizing is performed at 500-570 °C for various time ranges stretching from 5-180 min, followed by water quenching. NA is unavoidable due to intensive transportation times although it might harm peak strength in subsequent AA. The minimum predicted time necessary for blanks to reach the stamping facility is typically set to 1 month. AA is typically conducted at elevated temperatures of 160-220 °C. In case of car outer panels, AA temperatures are usually within a range of 170-185 °C and the heat treatment procedure takes about 20-30 min to reach the peak strength. [2,17,18]

For a better understanding of strengthening mechanism by precipitation hardening, it is necessary to analyze microstructural changes after the solutionizing. Microstructural changes during AA are generally more complex than changes occurring during NA. This is the main reason for higher interest in investigations of the effects of AA than of NA on changes in material properties. Research works studying the influence of NA on the properties of Al-Mg-Si alloys are shown in Table 4. Moreover, phase transformation sequences occurring during the precipitation hardening of Al-Mg-Si alloys are illustrated in Figure 5. The early stage of NA is characterized by the formation of uniform Si and Mg clusters from SSSS. Increasing the NA time results in the dissolving of Mg clusters and the accumulation of Mg atoms at Si clusters forming Mg/Si co-clusters. Further increase of NA time leads to co-cluster growth and formation of GP(I) zones. These phenomena are known as clustering. Increasing the size of the clusters and co-clusters hinders the dislocation movement during the plastic deformation and leads to an increase in strength. Co-clusters and GP(I) zone sequences are fully coherent with the primary

phase and there is no significant difference between them in terms of chemical composition. After reaching the size of a couple of nanometers, co-clusters are called GP-Zones, and the difference between them is usually distinguished using conventional TEM. Further increase of NA does not result in notable changes in phase sequences. The occurrence of the metastable phase  $\beta''$  is related to peak strength at elevated temperatures. This phase sequence is only partially coherent with the primary phase, and it can directly evolve from GP(I) precipitates or indirectly from the intermediate phase called pre- $\beta''$ . Moreover, reaching this phase is the goal of the paint-baking process since it is responsible for peak strength. Therefore, accurate determination of AA time and temperature is immense for avoiding eventual underaging and overaging. Moreover, a various number of metastable phases such as  $\beta'$ ,  $B'$ ,  $U1$ ,  $U2$ , or  $U3$  can be observed by increasing the AA time on the way to the equilibrium phase  $\beta$ . The equilibrium phase  $\beta$  is associated with high aging temperatures. Formation of each of these phases is not mandatory during the precipitation hardening of Al-Mg-Si alloys. Some phase sequences may not occur depending on chemical composition, aging temperature and aging time. [18–24]

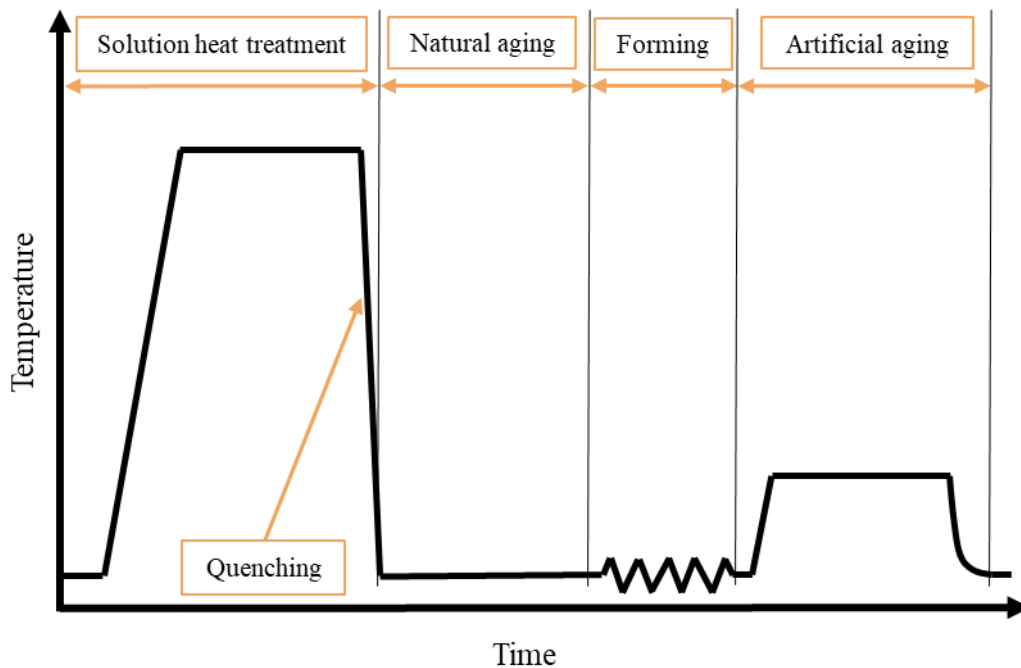


Figure 4 Schematic illustration of processing of Al-Mg-Si alloy blanks in production of car outer panels [17]

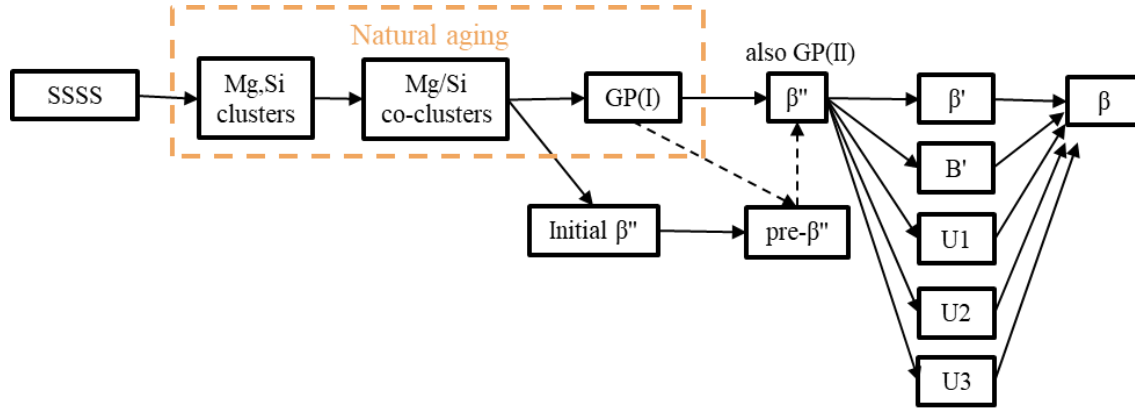


Figure 5 Phase sequences observable at different stages of precipitation hardening of Al-Mg-Si alloys [18]

Table 4 Literature overview about the influence of natural aging on properties of Al-Mg-Si alloys

Alloy	Mg	Si	Aging	SHT temp.	SHT time	NA time	AA temp.	AA time	Ref
[ - ]	[wt.%]	[wt.%]	[ - ]	[°C]	[min]	[days]	[°C]	[h]	[ - ]
6060; 6111/6082	0.4 - 0.59	0.4 - 0.82	NA, AA	535 - 540	30-60	180	180	167	[18]
6022	0.6	1	NA, PS, AA	530	30	30	170	0.5	[25]
N/A	0.5	1.15	NA, AA	560	45	N/A	175	30	[26]
6082	0.64	0.5	NA, AA	530	60	45	180	168	[27]
6016	0.3	1.23	NA, PA, AA	560	5	28	185	96	[28]
6111	0.79	0.60	NA, AA	560	10	14	160 - 220	100	[29]
N/A	0.5 - 0.76	0.54 - 1.0	NA	N/A	N/A	~21	N/A	N/A	[30]
6111; 6022	0.58 - 0.6	0.82	NA	550	5	70	N/A	N/A	[31]
6016	0.55	1.1	NA, PA, AA	560	5	14	185	6	[32]
6014	0.65	0.59	NA	540	60	180	N/A	N/A	[33]
6016; 6111	0.4	0.81 - 1.39	NA, AA	560	N/A	30	180	0.5	[34]
N/A	0.69 - 1.31	0.55 - 1.10	NA, AA	560	30	14	180	15	[35]
6011	0.6	0.6	NA, AA	N/A	N/A	N/A	120 - 205	18	[36]
6016	0.41	0.91	NA	N/A	N/A	547.5	N/A	N/A	[37]
6063	0.51	0.28	NA, AA	520	60	30	180	8	[38]
6022	N/A	N/A	NA, PA, AA	560	180	28	N/A	N/A	[39]
6061	0.8	0.63	NA, AA	550	120	0.166	200	10	[40]
6061	0.91	0.8	NA, AA	500	120	0.166	200	48	[41]
N/A	0.3 - 1.01	0.20 - 1.18	NA, AA	560	75	1/6	175	300	[42]
6016; 6005A; 6063; 6013	0.32 - 0.98	0.64 - 1.03	PA-NA, AA	N/A	N/A	180	185	1/3	[43]

N/A	1.02	0.93	NA, PA, PS, AA	530	30	14	170	0.5	[44]
6060; 6005; 6082	0.37 - 0.62	0.43 - 0.99	NA	535	10	150	N/A	N/A	[45]
6111	0.7	0.7	NA, AA	N/A	N/A	N/A	100 - 180	N/A	[46]
6016	0.19* Si	N/A	NA	N/A	N/A	547.5	N/A	N/A	[47]
6016; 6061	0.41 - 1.2	0.4 - 0.91	NA	N/A	N/A	547.5	N/A	N/A	[48]
N/A	0.9	1	NA, AA	N/A	N/A	15	170	48	[49]
N/A	1.09 - 1.14	0.7 - 0.71	NA, AA	570	20	24	170	14	[50]
6061	0.78 - 0.87	0.61 - 0.72	NA	530; 570	20	130	N/A	N/A	[51]
N/A	0.95	0.85 - 1.55	NA, AA	550	30	90	180	10	[52]
6016	0.42	0.95	NA, PA	550	30	7	N/A	N/A	[53]
6061	1.02	0.61	NA, AA	527	60	2	160	16	[54]
6014	0.65	0.59	PA-NA, AA	540	60	180	180	0.5	[55]
6063	N/A	N/A	NA	510	10-15	672	N/A	N/A	[56]
6016	0.471	1.147	NA-PA, AA	560	30	7	180	8	[57]
N/A	0.41 - 1.06	0.45 - 1.50	NA	550	30	30	N/A	N/A	[58]
6061	0.59	0.74	NA, AA	550	60	7	180	128	[22]
N/A	0.66 - 1.01	0.52 - 1.00	NA, AA	530	10	1/6	170	75	[59]

## 2.2 Experimental material characterization

### 2.2.1 Mechanical material properties

Uniaxial tensile test is likely the most common testing method for characterizing the mechanical properties of sheet metals. The uniaxial tensile test of metallic materials at room temperature and the sample geometry is defined according to standard DIN EN ISO 6892-1. The typical geometry of bone-shaped tensile testing samples is illustrated in Figure 6. Important geometrical characteristics of tensile testing samples include original thickness  $s_0$ , original width of the parallel length  $b_0$ , and original gauge length  $l_0$ . The original gauge length  $l_0$ , refers to the initial position of extensometers, which accurately measure the elongation in that area during the test.

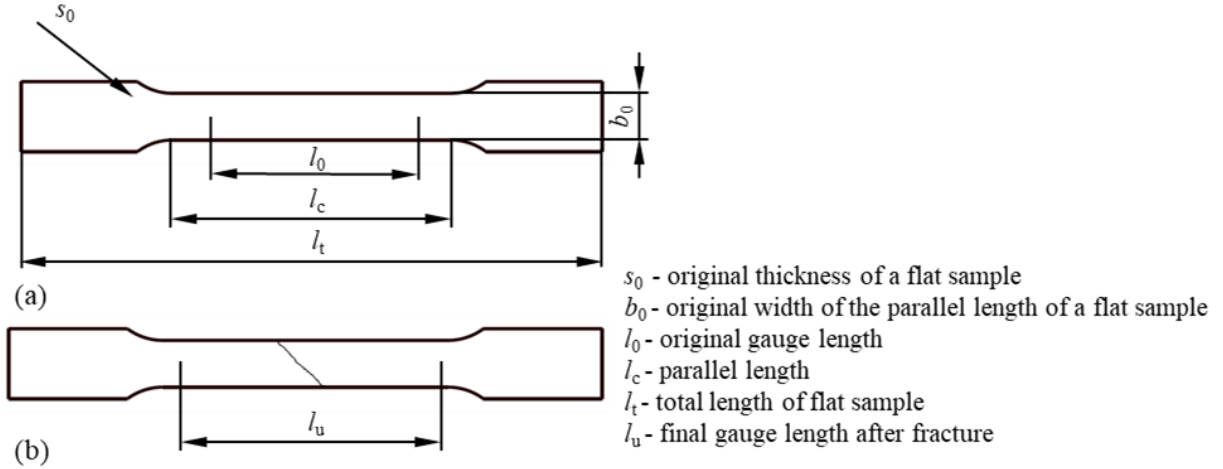


Figure 6 Schematic illustration of a flat sample for uniaxial tensile testing in (a) initial and (b) fractured state

Material flow is defined by the sample geometry and occurs only in the narrowed area of the sample. Based on the measured tensile forces and the sample elongation, characteristic stress-strain curves can be calculated. It is necessary to distinguish between the engineering and the true values as shown in Figure 7. Engineering stress  $\sigma_0$  and engineering strain  $\varepsilon$  are calculated using Equations (1) and (2), respectively, with  $F$  representing the measured tensile force,  $A_0$  being the original cross-section in the narrowed area of the sample and  $\Delta l$  being the sample elongation measured by extensometer. During the uniaxial tensile test samples are firstly exposed to elastic straining and subsequently to plastic straining. Elastic straining is characterized by the linear stress-strain increase whereas the plastic straining reflects the strain-hardening behavior and the ductility of the material. Reaching the maximum tensile force is associated with the initiation of localized necking. The following mechanical material parameters can be determined based on the engineering stress-strain curves:

- Young's modulus  $E$  refers to the slope of the linear increasing part of stress-strain curve.
- Yield strength  $R_{p0.2}$  is strength measured at 0.2% of plastic strain.
- Ultimate tensile strength  $R_m$  is the maximum strength occurring just before necking initiation.
- Uniform strain  $A_g$  refers to maximum elongation of sample prior to necking initiation.
- Fracture strain  $A_{80}$  is the total elongation of the sample determined using the extensometers with original gauge length  $l_0$  of 80 mm.

However, the cross-section in the narrowed area of tensile testing samples reduces during the straining, which results in comparatively higher stress-strain curves for true values than for engineering values. True stress  $k_f$  and true strain  $\varphi$  can be calculated using Equations (3) and (4) for the period of uniform elongation, which ends by initialization of localized necking. The true values are frequently described by the so-called flow curve, which can be used for generating the material models in numerical simulations. However, the flow curve does not consider the elastic straining but only describes the true stress  $k_f$  – true plastic strain  $\varphi_{pl}$  behavior of the material. The strains obtained from the uniaxial tensile test are eventually not sufficient for

application in numerical simulation. Namely, numerical forming simulations require flow curves with the true plastic strains of about 1. The true plastic strains obtained from uniaxial tensile test are in the range of about 0.2 for Al-Mg-Si alloys. Thus, the data obtained from the tensile test must be extrapolated. The most common extrapolation model for aluminum alloys is Hockett-Sherby [60] and combined Swift [61] / Hockett Sherby model. Some other material testing methods such as bulge test or stack-compression test can be used for validating the tendency of flow curves at higher plastic strains. [16,62–64]

$$\sigma_0 = \frac{F}{A_0} \quad (1)$$

$$\varepsilon = \frac{\Delta l}{l_0} \quad (2)$$

$$k_f = \frac{F}{A} = \sigma_0(1+\varepsilon) \quad (3)$$

$$\varphi = \ln \frac{l}{l_0} = \ln(1+\varepsilon) \quad (4)$$

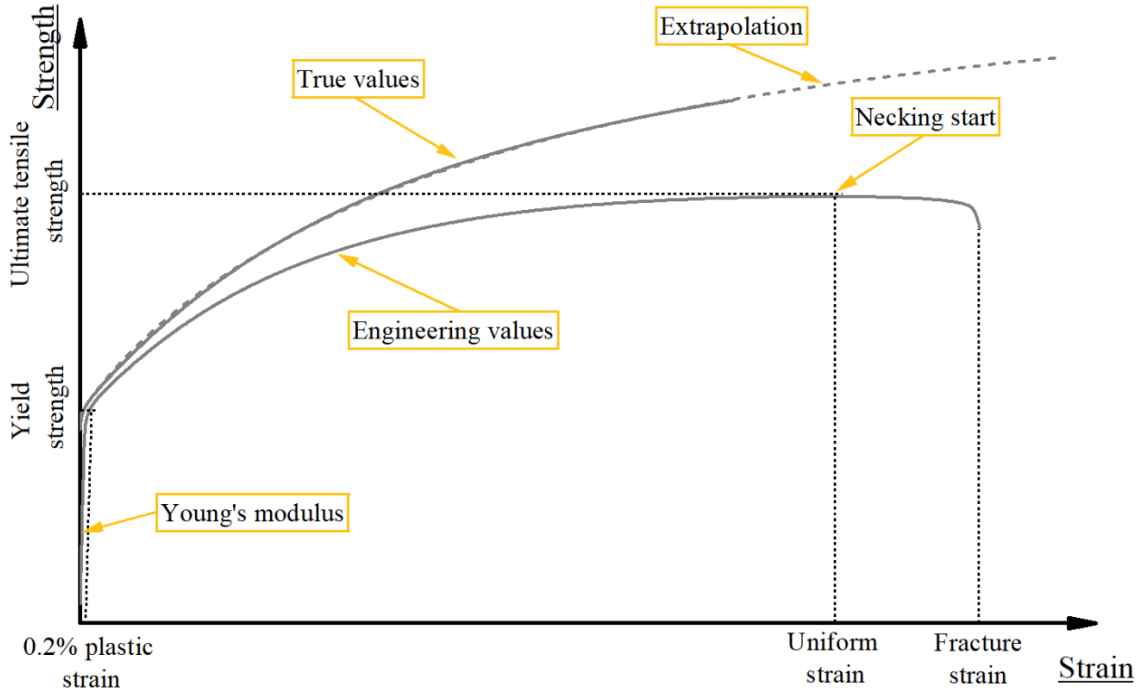


Figure 7 Stress-strain curves obtained by uniaxial tensile testing

### 2.2.2 Strain hardening exponent ( $n$ -value)

Strain hardening refers to an increase in material strength during plastic deformation. The strain hardening capacity is typically described by  $n$ -value (strain hardening exponent). According to standard DIN ISO 10275,  $n$ -value equals the slope of the flow curve measured between two strain values as illustrated in Figure 8. However, the strain-hardening behavior of aluminum alloys is variable and depends on the extent of true plastic strain [65]. During the straining of aluminum alloys, strain hardening capacity increases reaches a maximum at about 5-6% of true plastic strain and subsequently decreases. Therefore, it is important to highlight the strain range used for the evaluation of  $n$ -values. The usual determination of  $n$ -values is conducted for a strain range of 2-20%. Higher  $n$ -values reduce the formation of localized strain gradients, which is in general beneficial for the blank formability. [16,62,66]

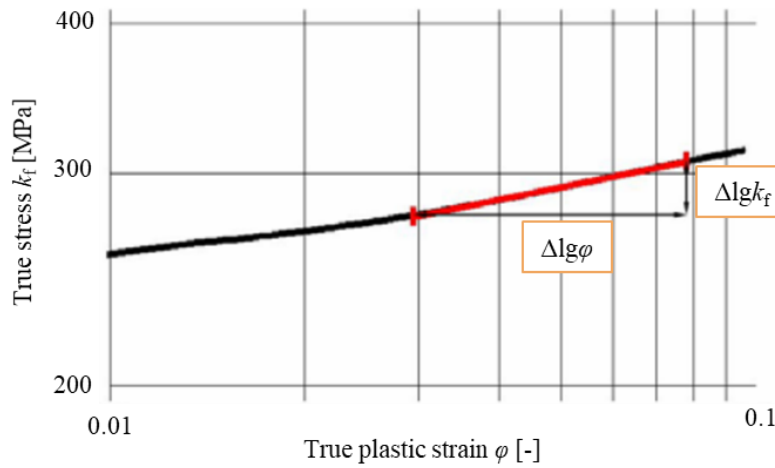


Figure 8 Determination of  $n$ -values using stresses and strains from flow curve (adapted from [67])

### 2.2.3 Anisotropy ( $r$ -value)

Anisotropy refers to the direction dependency of material properties. In the case of blank materials, anisotropy is a direct consequence of the rolling process, which is an unavoidable part of blank production. The rolling process leads to crystallographic texturing reflecting in different sizes, shapes, and orientations of grains e.g., parallel and perpendicular to the rolling direction. Thus, differences in mechanical properties may also be observed in these two directions. Affected mechanical properties include  $n$ -value, the yield and the tensile strength, the uniform, and the fracture strain. A common way to describe the anisotropic behavior of blanks is normal anisotropy or  $r$ -value, which can be determined by performing the uniaxial tensile test. The material flow of the tensile testing sample must be accurately monitored using width and length extensometers during the uniaxial tensile test as shown in Figure 9. Equation (5) is used for calculating the  $r$ -values, with  $b$  as the actual sample width,  $b_0$  as the original sample width,  $s$  as the actual sample thickness, and  $s_0$  as the original sample thickness. Normal anisotropy describes if the material flow is more dominant from the width or from the thickness of the tensile testing sample. If the material flow is predominantly due to a reduction of sample width,  $r$ -value is greater than 1. However, if  $r$ -value is smaller than 1, the material flow is mainly due to the sample thinning, which leads to earlier localized thinning and cracking of blanks. Therefore, the focus

of material suppliers is set on increasing the  $r$ -values to achieve better formability of blanks. Similar to  $n$ -values,  $r$ -values also vary during the uniaxial tensile test. For most materials,  $r$ -values decrease with the increasing tensile strain. Thus, for easier comparison between materials, it is necessary to specify the extent of strain or strain range used for the evaluation of  $r$ -values. This is typically 10% or 20% of engineered strain or an average  $r$ -value is also frequently determined for specific strain ranges such as 2-20% or 10-15%. [16,62,68]

$$r = \frac{\varphi_b}{\varphi_s} = \frac{\ln \frac{b}{b_0}}{\ln \frac{s}{s_0}} \quad (5)$$

However,  $r$ -values of blank materials are usually determined using the tensile testing samples cut in a rolling direction ( $r_0$ ), diagonal direction ( $r_{45}$ ) and transverse direction ( $r_{90}$ ). Based on these  $r$ -values, planar anisotropy  $\Delta r$  and average normal anisotropy  $r_m$  can be calculated using Equations (6) and (7), respectively. Note that Equation (6) is only valid if  $r_0 \approx r_{90}$ , otherwise planar anisotropy is calculated as  $\Delta r = r_{\max} - r_{\min}$ . Planar anisotropy  $\Delta r$  describes the effect of rolling direction on the uniformity of mechanical properties in different directions over the blank surface (plane). If  $\Delta r$  is closer to 0, the mechanical properties are more uniform. In particular, the material flow during the forming of such blanks is uniform from all directions, which is generally beneficial for formability. However, if  $\Delta r$  is significantly higher or lower than 0, notable differences in mechanical properties and non-uniform material flow are expected. Non-uniform material flow leads to an earing effect, which is especially visible during the forming of cup-shaped components. Two criteria are guidelines for exploiting the highest potential of blank materials regarding formability, i.e., maximum  $r_m$  for delaying the localized necking and  $\Delta r = 0$  for having the uniform material flow. [2,16,62,69]

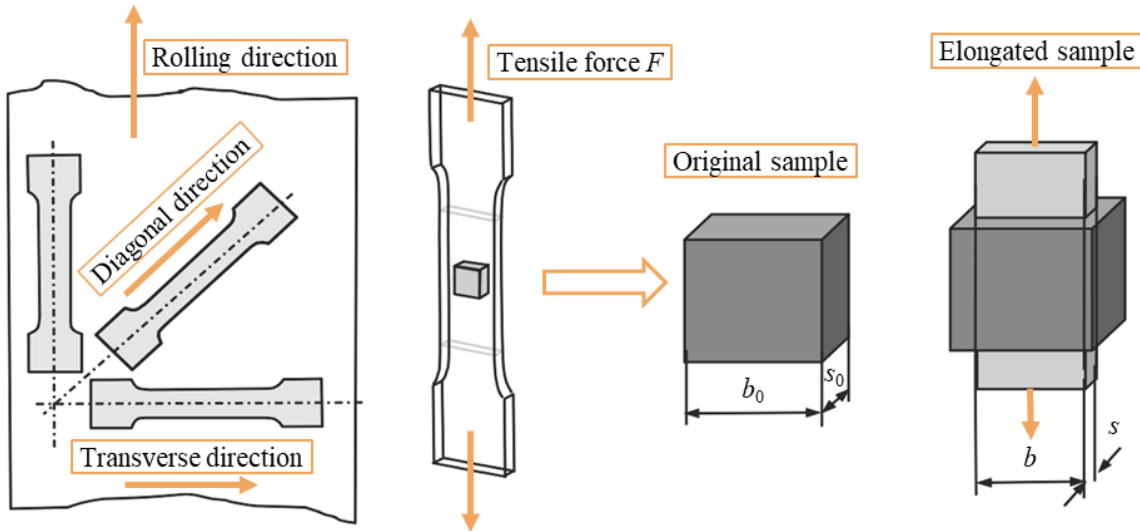


Figure 9 Determination of  $r$ -values using the samples for uniaxial tensile test (adapted from [16])

$$\Delta r = \frac{r_0 - 2r_{45} + r_{90}}{4} \quad (6)$$

$$r_m = \frac{r_0 + 2r_{45} + r_{90}}{4} \quad (7)$$

#### 2.2.4 Yield surface

The transition from elastic to elastic-plastic deformation of sheet metals is known as yielding or material flow start. The start of material flow depends on the applied stress state (e.g., there is a clear difference between uniaxial tension and biaxial tension). The dependency of material flow on the stress state of blank materials is described by a yield surface curve. If the stresses applied onto the sheet material are within the yield surface curve, only elastic deformation occurs. However, elastic-plastic deformation occurs when the stress state exceeds the yield surface curve. Figure 10 schematically illustrates the testing methods and induced stress states required for the full determination of a yield surface curve. An accurate description of the yielding behavior of blank materials is particularly important for numerical forming simulations. Several yielding criteria have been established in the past. Basic yielding criteria include models such as Tresca and von Mises. However, these criteria poorly describe the yielding behavior of aluminum alloys. Hence, some advanced models exist for describing the yielding behavior of aluminum alloys such as Barlat (1989) [70] and BBC2005 [71]. Generation of Barlat (1989) model requires a definition of material-specific constant  $M$  and some data from the tensile test, i.e., flow curve,  $r_0$ ,  $r_{45}$  and  $r_{90}$ . According to several scientific works, an accurate description of the yielding behavior of aluminum alloys can be described using the constant  $M = 8$ . [16,62,72,73]

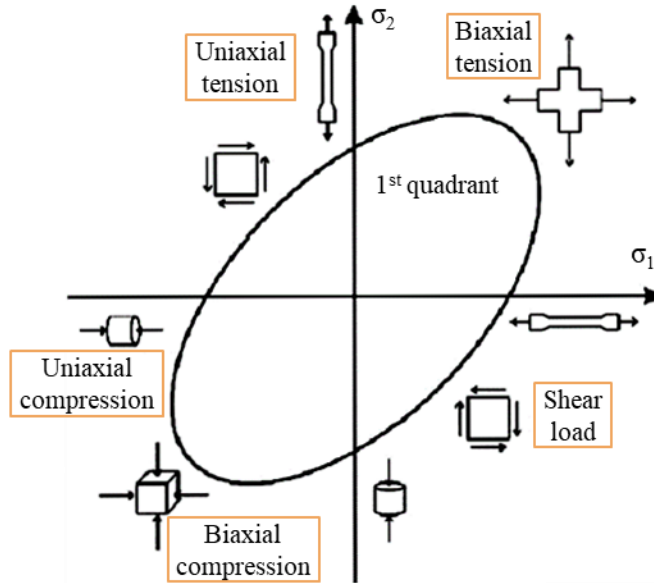


Figure 10 Illustration of loads and stress states necessary for experimental determination of yield surface (adapted from [64])

### 2.2.5 Stack compression test

The maximum reachable true strain from the uniaxial tensile test for Al-Mg-Si alloys with comparatively good formability such as AA6016 in T4 temper condition is about 0.2 [74,75]. Yet, significantly higher strains are induced during the forming of complex automotive components. The flow curve is an essential part of describing the material behavior in numerical forming simulation. Thus, an accurate extrapolation to higher strains of the flow curve derived from the tensile test is necessary. Material strength at true strains higher than 0.2 can be analyzed using additional testing methods such as the hydraulic bulge test according to standard ISO 16808. Yet, a special machine is required for conducting the bulge tests, which remarkably restricts the number of potential users. An alternative for reaching higher true strains during the forming of blank materials is a stack compression test that can be performed on the uniaxial tensile testing machine. This method can provide true strains up to 0.5, which is commonly higher than true strains observable during deep drawing. Note that FE software for numerical forming simulation requires flow curves with a true strain of about 1. Thus, this method can facilitate the extrapolation of flow curves to higher strains. The main difference between the results obtained using the tensile test and stack compression is in the resulting stress state. Namely, the tensile test provides uniaxial tensile stresses whereas the stack compression test provides biaxial compressive stresses. This may lead to slight differences between the flow curves. However, a good agreement between the data from the tensile test and stack compression test can still be achieved as illustrated in Figure 11. Hence, the data obtained from the stack compression test should be primarily for extrapolating the data from the tensile test.

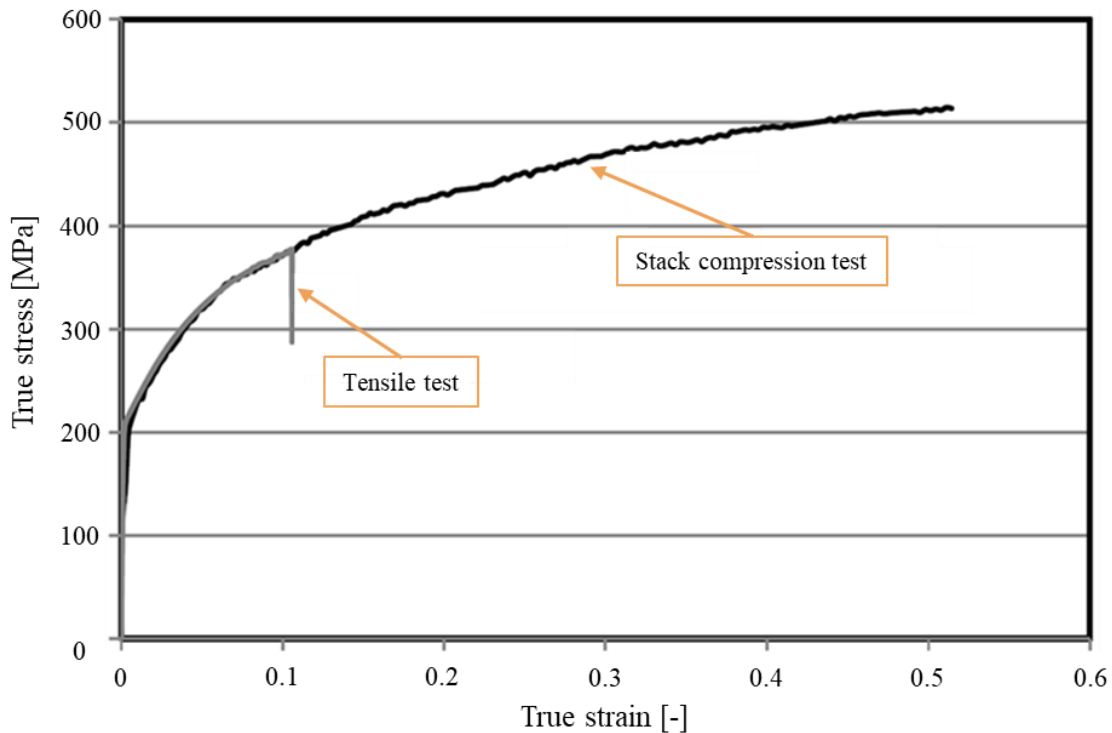


Figure 11 Flow curves obtained by the tensile test and by the stack compression test [64]

However, a valid standard for this testing method is still missing. Usually, testing parameters such as sample geometry and deformation velocity are based on the compression of cylindrical, metallic bodies according to standard DIN 50106. The ratio of sample height to sample diameter is 1:1 so the number of metallic disks in the stack compression test depends on blank thickness. However, the number of disks used for stacking does not affect the resulting flow curve. Moreover, the rolling direction of blanks must be considered during the stacking of blanks. A difference compared to full cylindrical bodies may be due to the friction between metallic disks. Stack compression tests were successfully utilized for determining the flow curve of steel and aluminum alloys blanks. [64,76–80]

## **2.3 Deep drawing fundamentals**

### **2.3.1 Introduction to deep drawing**

A car body consists of an average of 300-400 components made from blank materials. Most of these components including car outer panels are produced by a sheet metal forming process called deep drawing. This forming process is defined according to standard DIN 8544-3 as follows:

*“Deep drawing is a tensile-compressive forming process, for forming of a sheet metal blank into a hollow body open on one side or a formed hollow body into a hollow body with a smaller cross-section, without intentionally modifying its wall thickness.”*

Apart from application in the automotive industry, deep drawing is also used for producing daily life items such as cooking pots or bathtubs. Diverse blank materials including steel, aluminum and its alloys, titanium, copper, and its alloys can be formed using this process, which makes deep-drawn components suitable for a wide range of applications. The main parts of deep drawing tools are punch, die, and blankholder. Only these tool parts are in direct contact with blanks during forming operations, so they determine the geometry of the formed component. The deep drawing procedure typically consists of 4 steps as shown in Figure 12. A blank with a specific outline was placed either at die or at the blankholder in step 1, so punch and die are facing opposite sides of the blank. Step 2 is known as tool closing so a relative movement of one tool part is necessary (die or blankholder). Step 3 is characterized by the clamping of blank between blankholder and die by application of blankholder force (BHF). In step 4, blank was formed into a hollow body by relative movement between the punch and other tool parts. In general, two principles of tool movement during blank forming exist, i.e., (1) punch is fixed, and other parts move simultaneously and (2) punch is moving, and other parts are fixed. [16]

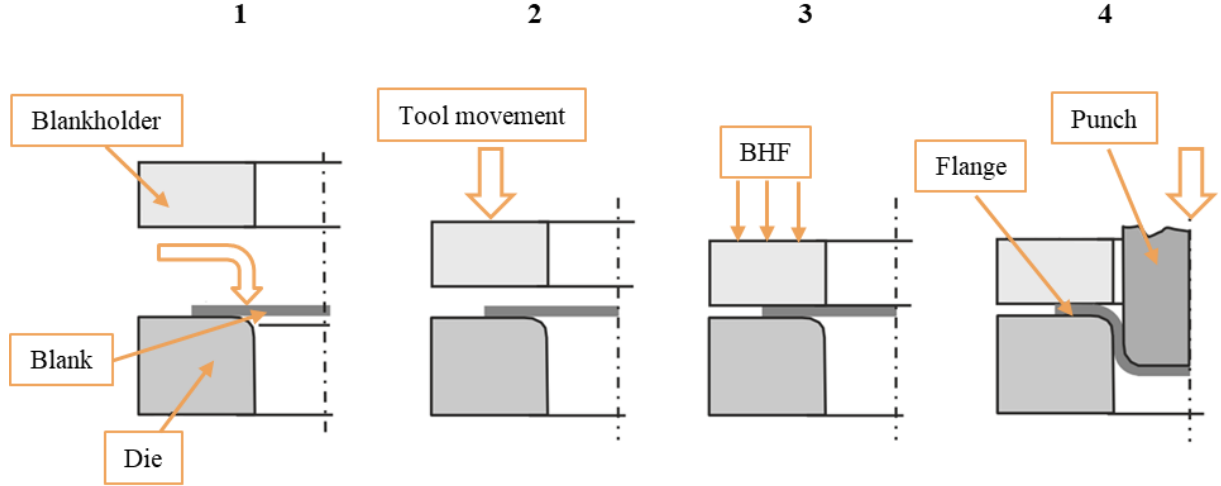


Figure 12 Basic steps in deep drawing procedure and the main parts of a deep drawing tool and [16]

Punch and die provide the final geometry of deep-drawn components whereas blankholder is used for controlling the material flow into the tool cavity. Figure 13 (a) shows a cup-shaped tool with a punch diameter  $d_0$  and a circular blank with a diameter  $D_0$ . Forming force or punch force is a force working on the punch during deep drawing operation and represents the necessary force for forming the component. Forming force can be measured using load cells placed under the punch. This force can be used for validating the forming simulations and in combination with BHF it can be used for determining the size of the forming press. Furthermore, the punch radius and the die radius play a significant role in forming of blank materials. Smaller die and punch radii limit the material flow compared to bigger radii. Less material flow leads to more intensive material stretching and earlier cracking of blank material. Figure 13 (b) illustrates the main areas of the formed component, i.e., flange, sidewall, and bottom, which are unavoidable parts of simple and complex components. The relative movement measured from the first punch-blank contact to the final position of the tool is known as drawing depth and the final position of the tool is called the bottom dead center. After reaching this position, the tool parts are returning to the initial position. [16,81]

The formability of blanks determined using the cup-shaped tool is often expressed through the drawing ratio  $\beta_0$ , which is calculated using Equation (8) [82]. Maximum limiting drawing ratio  $\beta_{0,max}$  refers to the maximum blank diameter  $D_{blank}$  that can be completely drawn through the tool without occurrence of failures. By increasing the blank diameter, the flange area of the component increases and the stress conditions in the deformation zone change. Accordingly, the forming forces working at component bottom and the tensile stresses in sidewall increase which may lead to earlier cracking. Several factors influence the formability, i.e., blank material, blank thickness, tribological conditions, tool geometry (punch and die radius), tool gap, and blankholder force. [16]

$$\beta_0 = \frac{D_{blank}}{d_{punch}} \quad (8)$$

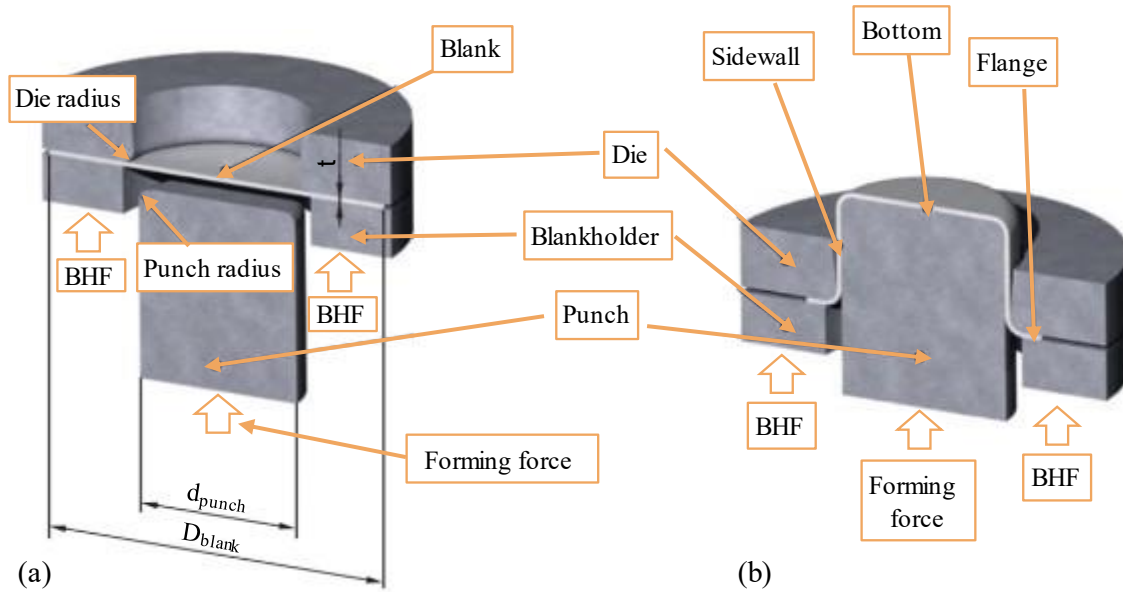


Figure 13 (a) A cup-shaped tool as a basic example of deep drawing and (b) deformation zones of deep-drawn component [81]

A notable, local increase of material strength occurs during the deep drawing due to plastic deformation of blank material. For a better understanding of changes in blank material during the forming, it is necessary to analyze strain states occurring in different areas of deep-drawn components. Figure 14 shows strain states in different zones of deformation for a cup-shaped component. The strengthening is especially significant in the area of die and punch radius. The transition area between the radius and the sidewall is of utmost importance in terms of component quality. So-called plain strains may occur in this area, which is the common reason for the cracking of deep-drawn components during the forming. The sidewall is characterized by tensile radial strains and compressive tangential strains. The plastic deformation of blank material in the punch radii area is blocking the material flow in the cup bottom, so only slight biaxial tension is observable in the component bottom. Slight biaxial tension may lead to the thinning of blank material in the component bottom. This principle is frequently applied on outer panels with high complexity. Namely, the material flow is blocked using block beads and the material stretching is the only deformation that occurs. The material strength increases due to strain hardening, which simultaneously increases the bulk strength of components. However, the highest deformation occurs in the flange area, which is constantly shrinking during the forming. Tensile-compressive strains occurring in this area may lead to an increase in the blank thickness in outer regions close to the blank edge. Thus, an additional clearance between the punch and the die is considered in tool design to prevent the clamping of blank material between tool parts. Clamping of blank material may damage the tool. Typically, the gap between punch and die equals the initial blank thickness, and the additional clearance is called the tool gap. The tool gap is characteristic of tools with vertical sidewalls that can completely draw blanks such as cup tools or cross-shaped tools. Yet, the industrial type of deep drawing tools usually has conical sidewalls so an additional gap is not necessary. However, strain states described in this section are typical

for cup-shaped components. Depending on tool geometry, the induced strain states in deep-drawn components may slightly vary in case of more complex tool geometries. [16,62,66,81,83]

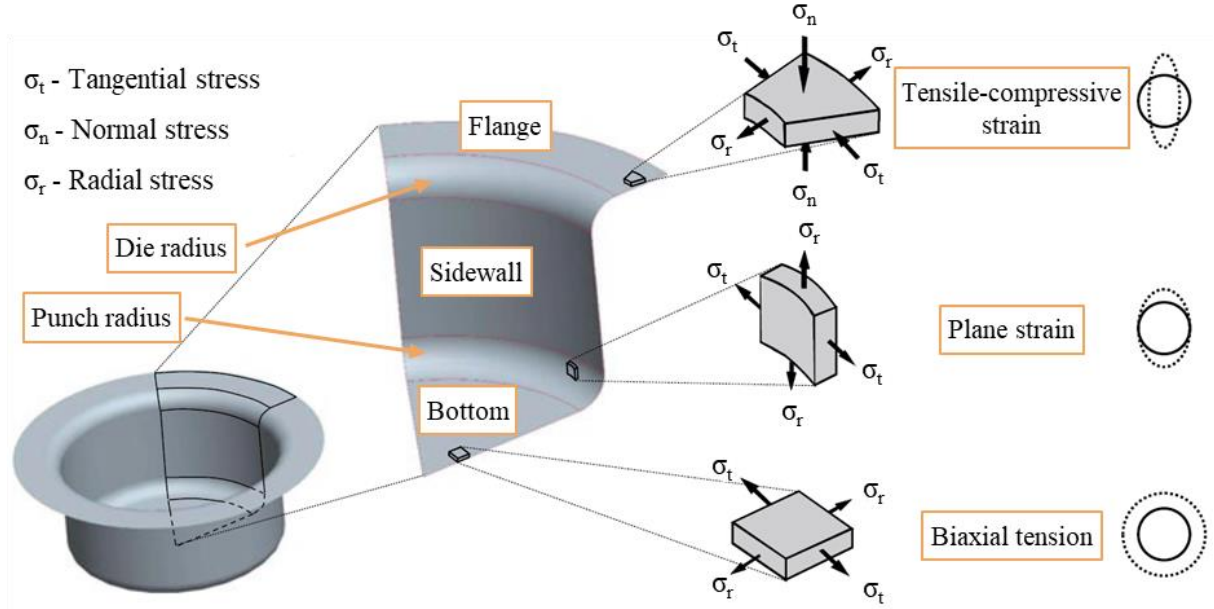


Figure 14 Deformation zones of deep-drawn components and corresponding strain states [84]

Scientific investigations are frequently conducted on very simple and compact tools such as cup-shaped tools or cross-shaped tools. Contrarily, deep drawing tools for industrial automotive applications produce components with complex and robust geometry. Despite having relatively simple geometry, various strain states can be induced in components formed using a cup-shaped tool as shown in Figure 14. A cross-shaped tool is an advanced version of a cup-shaped tool, that can induce even more complex strain states. These strain states are more similar to strain states of automotive components. Therefore, such relatively simple deep drawing tools are frequently used for formability characterization, comparison between materials, validation of numerical forming simulation, etc. Moreover, the drawing depth of these tools is adjustable, which makes them applicable for investigating blank materials with a wide range of formability. This principle is called open die and is usually not observable for industrial deep drawing tools. Deep drawing tools for industrial application typically have a closed die so variation of the drawing depth is not possible. This means that each formed component using tools with a closed die has the same geometry.

### 2.3.2 Failures

The target of deep drawing production lines is the forming of failure-free components; however, failures are an unavoidable part of the production process. The most common failures related to deep drawing include wrinkles, cracks, and springback as shown in Figure 15.

It must be distinguished between two types of wrinkles that may occur during deep drawing. Wave formation and overlapping of the waves due to tangential compressive stresses in the flange area are known as wrinkles of 1<sup>st</sup> order. Formation of these wrinkles can be avoided by the application of blankholder force. Compressive stresses applied to prevent the formation of wrinkles are typically in a range of 1-5 MPa. This is significantly lower than the tensile and compressive stresses necessary for starting the plastic deformation of blank material. Applied blankholder force depends on blank thickness, material strength, and type of material. Blanks with comparatively higher strength require higher blankholder force than blanks with comparatively lower strength. Moreover, thinner blanks have a higher wrinkling tendency than thicker blanks. Aluminum blanks have also a higher wrinkling tendency due to lower Young's modulus than steel blanks. Wrinkles of 2<sup>nd</sup> order occur in the conical sidewall area of components due to tangential compressive stresses. This type of wrinkles is influenced primarily by sidewall angle, material type, blank thickness, and stress state, which is affected by blankholder force. Avoiding the formation of these wrinkles is especially challenging in the production of complex car outer panels, which have conical sidewalls and require zero surface damage. The formation of the wrinkles in the conical sidewall is mainly due to a lack of contact between blank and tool surfaces. To prevent that, blankholder force should be increased. This would reduce the material excess in the tangential direction and reduce the wrinkling tendency.

The formation of cracks is alongside wrinkling the most frequent failure that occurs during deep drawing. Forming force, applied at the bottom of the component, is transmitted over component sidewalls into the flange area during deep drawing. The component being formed is locally exposed to different types and amounts of stresses and strains. Cracks initiate after strains locally exceed the forming limits. In the case of a cup-shaped tool, the cracking spot depends on the die radius and the punch radius so the crack will occur closer to a smaller radius, which limits the material flow and promotes the thinning. Typical measures for avoiding the crack occurrence are tool rework, enhancement of lubrication, change of blank material, etc.

Springback is a phenomenon that occurs after the forming operation is over when tool parts are moving from the bottom dead center toward the initial position. At the moment of tool opening, the elastic strains from the formed component are released. This may lead to certain deviations of component geometry from target geometry. In some situations, the extent of deviation can be too high so the following bonding operations cannot be accurately executed. The amount of springback can be calculated as a ratio between flow stress and Young's modulus. Higher yield strength and a higher  $n$ -value lead to an increase in springback. Moreover, lower Young's modulus also increases the springback. Therefore, the springback tendency of aluminum alloys is generally higher than springback tendency of steel alloys. The geometry deviation due to springback is particularly high after bending operations. In general, springback can be predicted by numerical forming simulations so certain geometrical tool features such as drawbead or side ribs can be implemented for preventing or reducing the springback.

These are the most frequent failures occurring during deep drawing. However, car outer panels also require outstanding surface quality. In the case of these components, some surface defects may occur such as flow figures, roping, deep scratches, etc. [2,16,84]

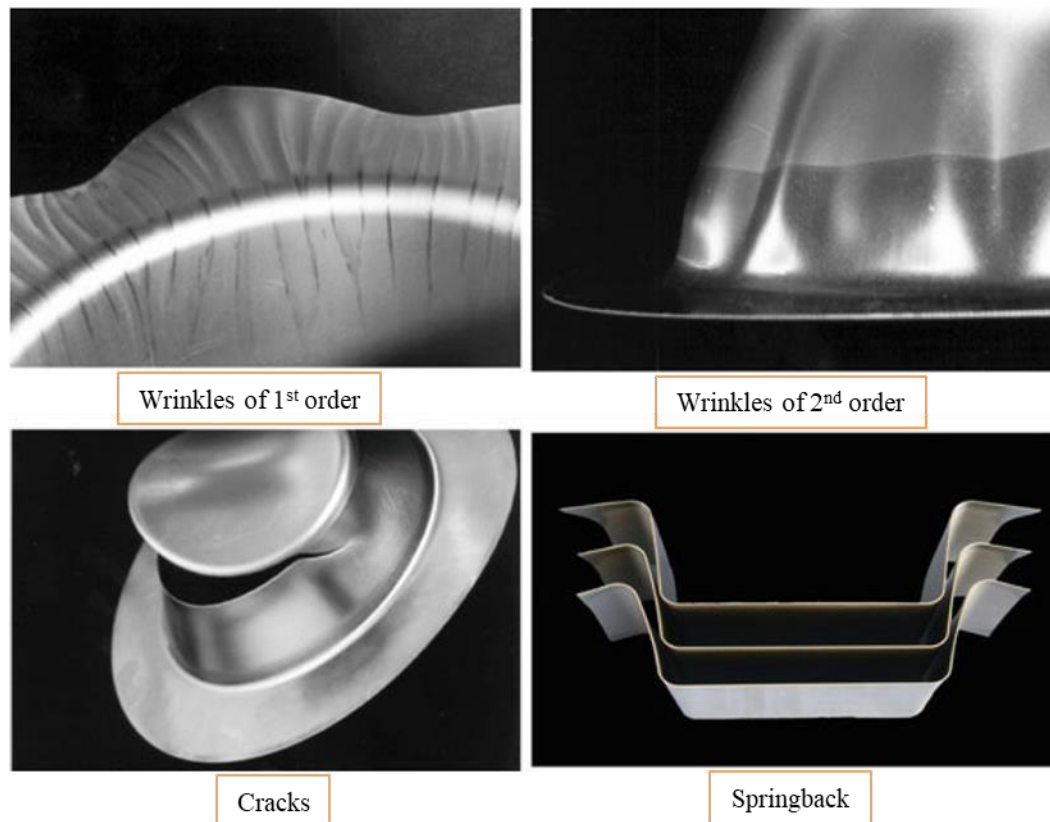


Figure 15 The most common types of failure related to deep drawing [84]

### 2.3.3 Role of the blankholder

The main role of the blankholder is a generation of blankholder force. The blankholder force is used for controlling the material flow and prevention of wrinkles. Straining of blank material during deep drawing is in general desirable for increasing the component strength through strain hardening and increasing the buckling strength of components. However, too high blankholder forces will lead to the production of components with cracks. Therefore, blankholder force should be used for balance between the prevention of wrinkles and the production of cracked components. Figure 16 illustrates the existence of a process window for forming components free of cracks and wrinkles. The process window is defined by blankholder force and drawing depth. At comparatively low drawing depths, the process window is wide and the robustness of process parameters for avoiding wrinkles and crack formation is high. However, increasing the drawing depth narrows the process window as the wrinkling tendency increases, which is compensated by increasing the blankholder force. An optimum blankholder force can be determined for achieving the maximum drawing depth. [16,72]

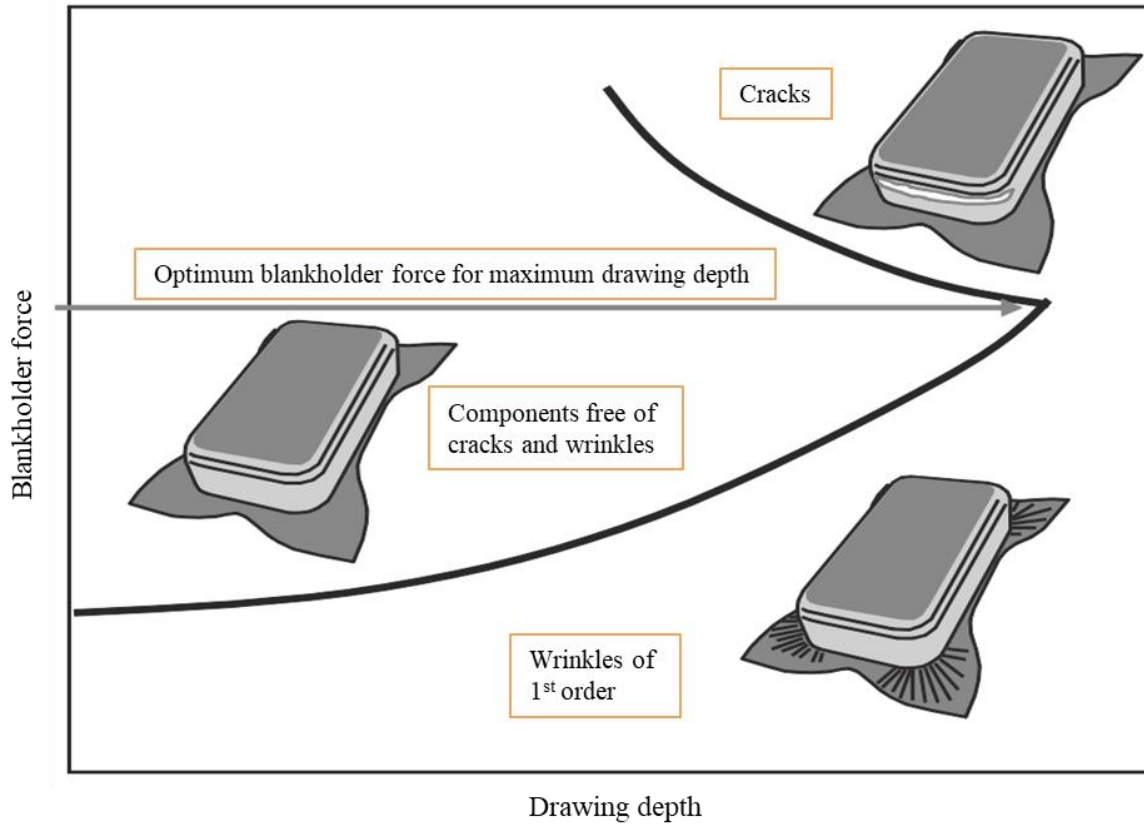


Figure 16 Process window for production of wrinkle- and crack-free components [16]

### 2.3.4 Forming Limit Curve (FLC)

Forming Limit Curve (FLC) illustrated in Figure 17 is a well-known failure criterion for describing the forming limits during deep drawing of blank materials. This criterion is important for evaluating the numerical forming simulations of deep drawing operations. The first research works in this field are based on a study by Gensamer [85] who observed that failure (necking or cracking) depends rather on local strains than on global strains. Keeler [86] pioneered the work in this field and observed that applied patterns at the blank surface in the form of circles became ellipses after biaxial tension deformation. He calculated the forming limits for this area in the form of maximum major strain  $\phi_1$  and minor strain  $\phi_2$  prior to failure based on the semi-axes of the ellipses. Goodwin [87] applied a similar procedure for calculating the critical major and minor strains for a tensile-compressive strain state. These two strain states, i.e., tension-tension and tension-compression, are of the highest interest for describing the forming limits of deep-drawn components. In fact, FLC was generated by connecting multiple, separately determined forming limit points in these two areas. FLC describes the maximum of specific strain states that can be induced for forming a failure-free component. It can be distinguished between necking or cracking failure, depending on how the test evaluation was executed. But generally, if the strains exceed the FLC a necking or a cracking may occur at the formed component. Commercially available FLCs describe necking initiation since the necking is also considered a failure and occurs prior to cracking. However, FLC is valid only if the strain path is linear, which always should be considered in forming simulations in case of complex geometry, drawbeads, etc. FLC

and strains induced in formed components are represented in the Forming Limit Diagram (FLD). This diagram provides a quick analysis of the obtained results and a direct comparison with the forming limits. [88,89]

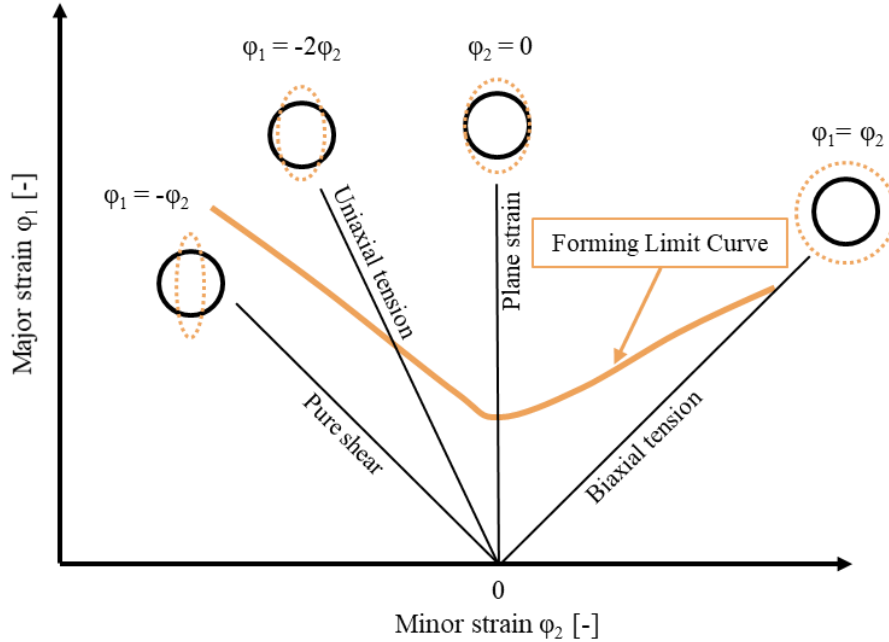


Figure 17 Schematic illustration of a forming limit curve and characteristic strain states

A specific FLC is valid only for a specific material including batch, alloy type, tempering, and thickness. Numerous testing methods for partial or fully experimental determination of FLC have been developed over the past. These methods include uniaxial tensile test, hydraulic bulge test, punch stretching test, Keeler test, Hecker test, Marciniak test, and Nakazima test [90,91] as the most used testing method nowadays. Nakazima introduced a testing method that uses a hemispherical punch, die, and blank samples with a different geometry shown in Figure 18 (a) and (b). Each of the sample geometries is used for the determination of forming limits for specific strain state. The forming of the full samples is characterized by biaxial tension whereas the forming of the narrowest samples is characterized by pure shear in the central area of the sample. A minimum of 5 different sample geometries are necessary to cover the domain of FLD relevant for deep drawing. A minimum of 3 repetitions were performed for each sample geometry. The evaluation of forming limits is done by measuring the major and minor strains shortly before failure using a digital image correlation (DIC) system. The testing procedure is described in detail by standard ISO 12004-5. Controlling the friction during the Nakazima test is an important challenge for preventing the scattering of the results. Thus, lubricants are utilized to minimize the friction, so the failure occurs in the central area of Nakazima sample. [62,83,88]

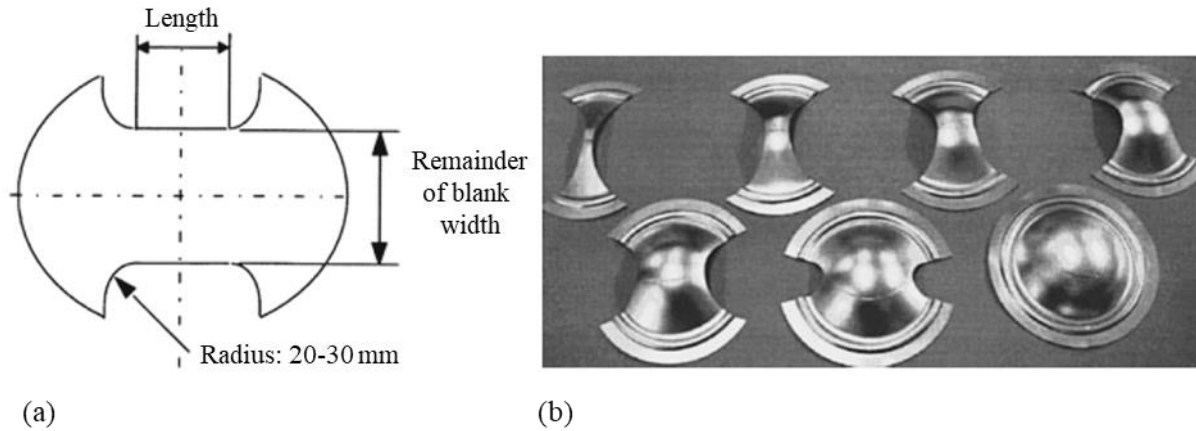


Figure 18 (a) Schematic illustration of Nakazima samples and (b) set of 7 formed samples with different geometry for determination of forming limit curve [88]

## 2.4 Hemming

Hemming is a common joining operation for bonding the outer panel components to the inner car components. In this forming operation, a narrow area around the outer panel outline is bent over the inner component outlines. In addition to bonding, hemming provides a better final appearance and reinforcement of component edges. The hemming procedure consists of three bending operations, i.e., flanging, pre-hemming, and hemming as shown in Figure 19. Flanging refers to  $90^\circ$  bending and pre-hemming to intermediate angle of approximately  $135^\circ$  bending. In the last step,  $180^\circ$  bending is conducted to close the hem. In this way, additional joining operations such as riveting are not necessary, and sharp edges are avoided. However, a good bendability of blank material is required for producing crack-free hems. This can be a challenge for aluminum alloy blanks, which have comparatively lower bendability than deep-drawing steels. If the existing bendability is not sufficient to produce flat hems, the flanging radius is increased, and a so-called rope hem is formed. Since aluminum blanks are roughly 1.5x thicker than steel blanks for the same application, aluminum hems are also significantly thicker than steel hems. Moreover, if a rope hem is required due to poor bendability, the thickness of the aluminum hem increases additionally. This should then be considered in car design for maintaining a high level of visual appearance for the combined use of aluminum and steel alloy blanks in the production of outer panels. [2]

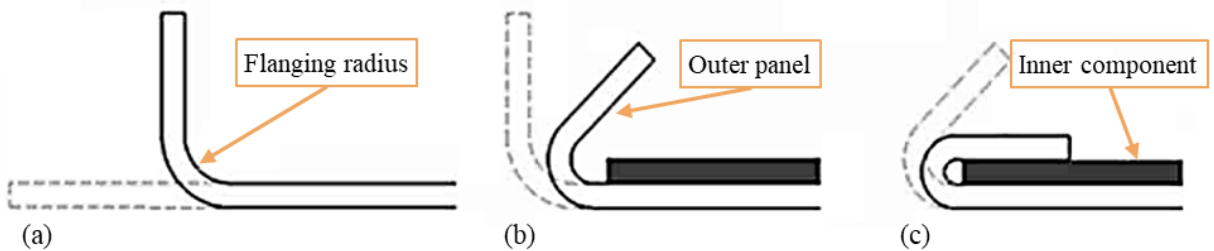


Figure 19 Bonding of outer and inner panels through hemming in 3 steps: (a) flanging, (b) pre-hemming and (c) hemming [33]

The bendability of blank materials can be analyzed by performing the relatively simple hemming test. The test results are usually evaluated by  $r_f/s$  ratio, with  $r_f$  representing the smallest flanging radius for the visually acceptable hem and  $s$  representing the blank thickness. However, visual evaluation is often not reliable, so other testing methods were developed. A well-known testing method for characterizing the bendability of aluminum and steel blanks is the plate bending test according to VDA 238-100. A schematic illustration of the test setup is shown in Figure 20. A drop in a monitored punch force (bending force) indicates the initiation of microcracks at the outer surface of the bent sample. Bendability is characterized by a maximum bending angle at maximum punch force. Geometrical and testing parameters for plate bending tests are shown in Table 5 and Table 6. Material failure during bending operation occurs in 4 steps:

- Orange skin formation
- Grooves formation parallel to the bending line
- Increase of grooves depth
- Shear failure at the deepest groove

Orange skin formation refers to roughening of the outer surface during bending resulting in a surface texture similar to orange skin. Failure can also occur inside the bent sample through void formation. The bendability of blank materials is affected by ductility, microstructure, strength, thickness but also pre-straining. Edge areas of deep-drawn components often have a certain amount of induced strain due to forming. This must be considered since pre-straining can deteriorate the bendability of blank materials. Moreover, the bendability of blanks is also dependent on the rolling direction so a difference in bendability properties is expected e.g. in the rolling direction and in the transverse direction. [2,31,92–94]

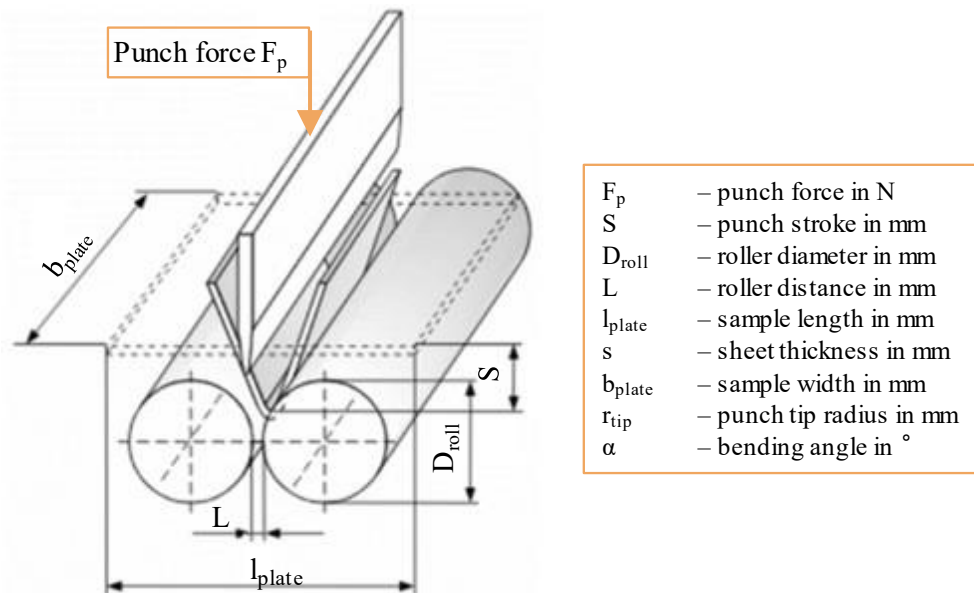


Figure 20 Plate bending test according to VDA 238-100

Table 5 Geometrical parameters for configuration of plate bending setup

Parameter	Value	
Blank thickness $s$	Material thickness	
Sample width $b_{plate}$	60 mm	
Sample length $l_{plate}$	60 mm	
Roller diameter $D_{roll}$	30 mm	
Punch tip radius $r_{tip}$	$s \leq 2$ mm	$s > 2$ mm
Steel ( $R_m \geq 780$ MPa)	0.4 mm	
Steel ( $R_m < 780$ MPa)	0.2 mm	0.4 mm
Al- and Mg-alloys	0.2 mm	0.4 mm
Roller distance $L$		
Steel	$2s + 0.5$ mm	
Al- and Mg-alloys	$2s$	

Table 6 Parameters for execution of plate bending test

Parameter	Value	
Velocity to pre-force	10 mm/min	
Pre-force	$s \leq 2$ mm	30 N
	$s > 2$ mm	100 N
Testing velocity	20 mm/min	
Force shot-off threshold	$s \leq 2$ mm	30 N
	$s > 2$ mm	60 N

## 2.5 Tribology in deep drawing

Tribology is a study concerned with contact, lubrication, friction and wear between two bodies in motion. The tribological conditions between two bodies in motion are often characterized by coefficient of friction (CoF). CoF  $\mu$  is calculated according to Coulomb's law using Equation (9), where  $F_F$  is frictional force and  $F_N$  is normal force. Some of the influencing factors on the CoF are: [95]

- Materials
- Surface texture
- Surface roughness
- Contact temperature
- Lubrication
- Sliding velocity
- Contact pressure
- Climate (temperature, moisture, ambient medium, ambient pressure)

$$\mu = \frac{F_F}{F_N} \quad (9)$$

A lot of general CoF for specific material pairings such as steel-steel or steel-aluminum can be found in literature lists. However, oxides and impurities at contact surfaces have more influence on the tribological system than bulk material itself. Moreover, the influencing factors mentioned above are frequently not specified in such lists. A single CoF is only valid for specific conditions, i.e., contact pressure, sliding velocity, temperature, etc. Hence, describing the general tribological conditions between two materials in contact using a single CoF value would be misleading. Therefore, the values from the literature lists can be only used as orientational values. The actual CoF should be experimentally determined by performing frictional tests. The testing conditions in such tests should be chosen based on actual conditions during material processing or application. [95,96]

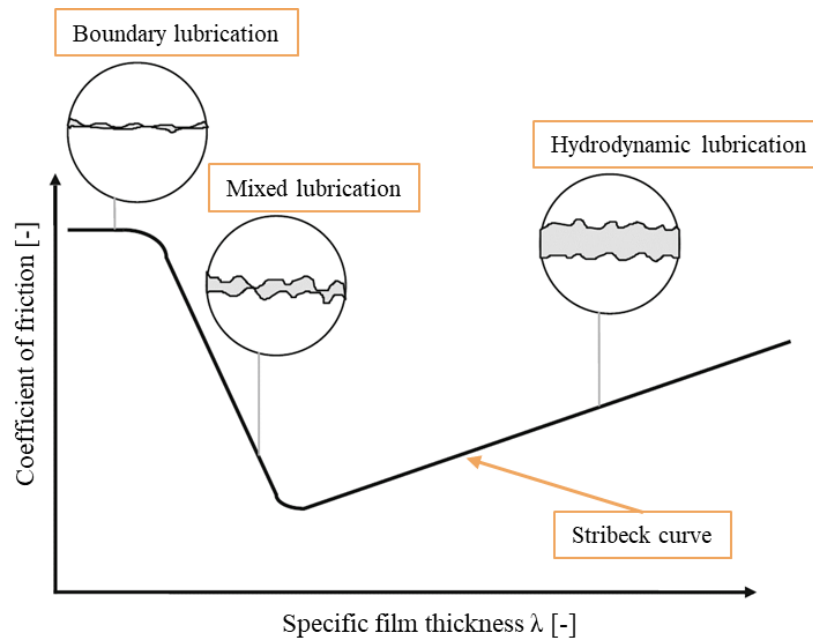


Figure 21 Lubrication regimes and Stribeck curve (adapted from [97,98] )

Lubrication is an important part of tribological systems that can reduce friction and wear. It can improve the performance (e.g., formability of blanks in deep drawing) and increase the service life (e.g., deep drawing tools). The importance of adequate lubrication in tribological systems can be described using lubrication regimes. There are 3 well-known lubrication regimes, i.e., boundary lubrication, mixed lubrication, and hydrodynamic lubrication. The effect of these lubrication regimes on CoF is described using the Stribeck curve shown in Figure 21. The highest CoF is expected for the boundary lubrication regime due to extensive direct contact between surface asperities. In combination with high heat energy input, this may lead to undesirable abrasive and adhesive wear. The lowest friction can be found in mixed lubrication regimes. Thus, a mixed lubrication regime is favorable for most working operations such as deep drawing. The load is partially supported by direct contact between surface asperities and partially by the lubricant. Wear can occur due to direct solid-solid contact and plastic deformation of surface asperities. Moreover, excess lubricant in hydrodynamic lubrication will lead to an increase in CoF. Hydrodynamic lubrication (full-film lubrication) is a regime where the contact surfaces are

completely separated by lubricant. Further increase of CoF is expected with increasing specific film thickness in this regime. [97]

Apart from the mechanical properties of blank material, the tribological conditions between the active components of deep drawing tools and blanks play an essential role in the processability of blanks. The friction directly affects the material flow, which can be used for controlling the deep drawing operation. The tribological system consists of a blank surface, tool surface, and lubricant. The lubricant prevents abrasion, reduces wear of active tool components, and particularly for aluminum alloys prevents adhesion at the tool surface and scratches at blank surfaces. Ensuring the mixed lubrication regime during deep drawing is also important for finding the optimum lubricant amount since excess lubricant affects production costs. Moreover, the lubricant selection should be in coordination with the following processing steps like lubricant removal to avoid additional costs and environmental pollution. [2]

The tribological system in deep drawing operation is characterized with:

- Moderate relative sliding velocity between tool surfaces and blank
- Generally low contact pressures in macroscopic contact areas
- Relatively big contact areas between tool surface and blank

Reduction of frictional forces during deep drawing operation can be achieved by applying oil, grease, or dry lubricants on the upper and lower surfaces of blanks. Preliminary tryouts are used for transferring the lubricant on the tool surface. The first tryout is usually performed with cleaned tool surfaces, and a lubricant film is stepwise transferred from blank to active tool surfaces. Approximately 15 tryouts are necessary for reaching the steady state so the tribological system is not changing with further tryouts. On a microscopic scale, a thin lubricant film is built during deep drawing between the tool surface and the blank surface. Yet, some areas with direct metallic contact are still present. The proportion of these areas depends on several parameters of which the most important are surface roughness, surface texture, and lubricant amount. Features of a tribological system between the tool surface and the blank surface are shown in Figure 22. Contact force is expressed through normal pressure ( $p_N$ ) applied in the moment of tool closing, and the actual contact between the tool surface and the blank surface is only between the surface asperities. The tool surface is significantly harder, so plastic deformation ( $k_f$ ) occurs at the blank surface asperities. This leads to generation of high hydrostatic pressure ( $p_{HS}$ ) in closed surface valleys filled with lubricant. Excess lubricant is squeezed out between the tool and the plastically deformed blank asperities, so a thin lubricant film was built. A relative movement described by velocity  $v$  between the tool and the blank leads to the generation of shear stresses  $\tau$ . If the lubrication film breaks due to high pressures, direct metallic contact between the tool and the blank surface asperities occurs, which may lead to adhesion through cold welding. Further, relative movement breaks the junctions so either blank material sticks to the tool surface or an abrasive particle breaks off. [2,99]

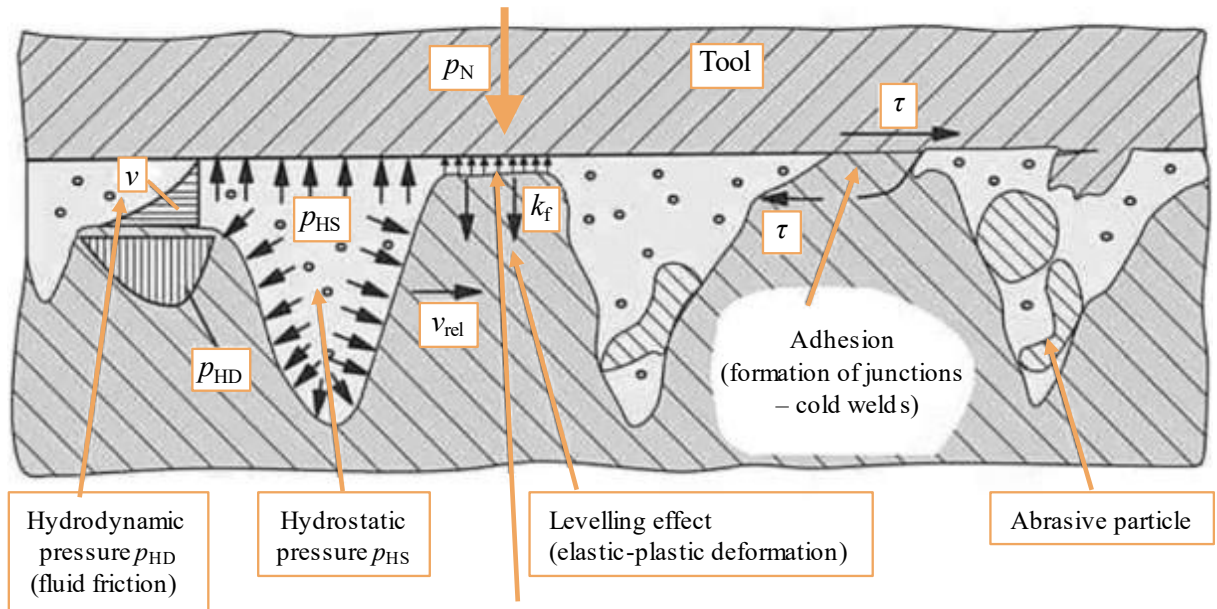


Figure 22 Tribological system observable for mixed lubrication regime in a deep drawing operation (adapted from [2])

Several testing methods were developed over the past for characterizing the tribological conditions in deep drawing operation. Most of the methods include blank strips and tool pins for simulating the contact between the tool and blanks. These tests were performed by using tribometers such as strip drawing or pin-on-plate and the tribological conditions were evaluated by determining the CoF. However, the testing parameters such as sliding velocity, contact pressure, and temperature are to be defined based on deep drawing conditions. Another important factor is the topology of the blank surface. The most used blank surface topographies nowadays are electric discharged texturing (EDT) and mill finish (MF). Although the coefficient of friction is usually lower for MF textured blanks, notably lower abrasion and adhesion can be observed for EDT blanks. This makes them suitable for the production of outer skin panels, which require exceptional surface quality. [2,100]

Figure 23 illustrates the tribological zones that are observable during the deep drawing of blank materials. Friction can be used for controlling the material flow in the tool cavity. The material flow can be improved by reducing the friction in the flange area (1) and the area around the die radius (2). Reducing the frictional forces in these areas reduces the material thinning and therefore enhances the formability. Simultaneously, the overall forming force reduces due to the reduction of frictional forces. However, higher friction is required in the punch radii area (3) and the sidewall area (4) for better transmission of the forming forces through the sidewall. A lower friction in the bottom area (5) is usually necessary when a certain amount of stretching is demanded. Moreover, the material flow in the tool cavity of rather complex components can be controlled by using drawbeads (6). These areas are characterized by high local pressures that can slow down or block the material flow. In this way, material stretching and strengthening are promoted, which enhances the bulk strength of formed components. Moreover, the springback is reduced in areas around the drawbeads. [2,16]

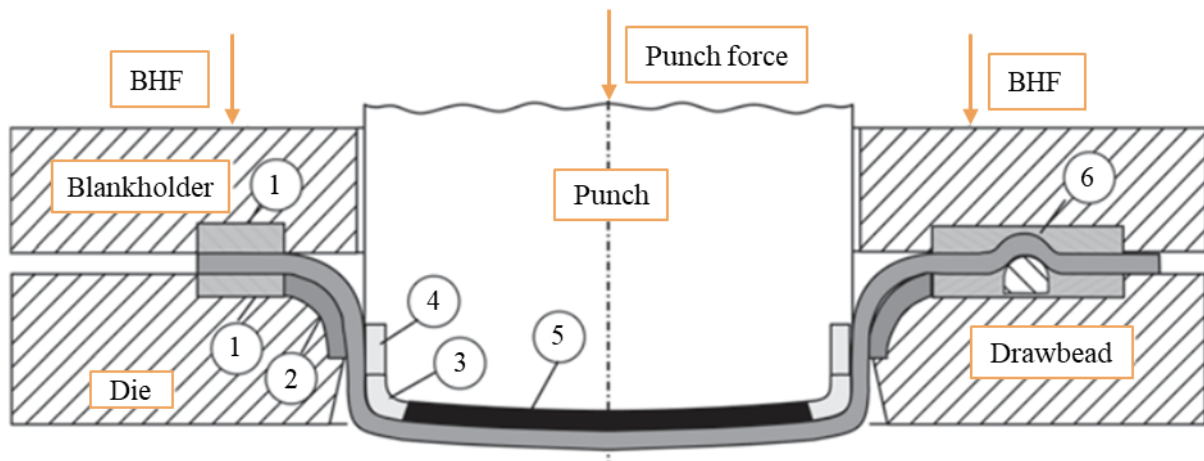


Figure 23 Tribological zones in deep drawing operation (adapted from [2])

### 3 Methods

#### 3.1 Materials

The influence of NA on the formability and material properties of 4 Al-Mg-Si blanks named AF1, AF2, AF3, and AF4 was investigated in this work. The difference between blanks with a thickness of 1 mm was in chemical composition or in lubrication. The investigated blanks can be categorized either as AA6016 (AF1, AF2, and AF4) or as AA6181 (AF3), whose typical chemical composition is shown in Table 7. Compared to blanks AF1, blanks AF2 had a higher content of Mg and Si but the same Mg/Si ratio of 1/3; however, blank AF3 had a higher content of Mg and lower content of Si and therefore a higher Mg/Si ratio of 7/10. Blanks AF1 and AF4 had the same chemical composition but different Hotmelt Drylube was applied on the surface of blanks. Namely, blanks AF1-AF3 were lubricated by the Multidraw Drylube E 1 and blanks AF4 by the ANTICORIT PL 39 SX. Blanks, supplied by AMAG rolling GmbH (Austria Metall AG, Ranshofen, Austria) had EDT surface texture. The periodical investigations on material properties and formability were conducted after 1, 2, 3, 6, 9, 12, 15, and 18 months of NA. The starting time of 1 month approximately represents the time blanks need to reach the forming facility.

Table 7 Typical chemical compositions of investigated blanks

Alloy	Mg/Si	Mg	Si	Cr	Cu	Fe	Mn	Ti	Zn	Other	Al
AA6016	1/3	0.25-0.60	1.00-1.50	0.10	0.20	0.50	0.20	0.15	0.20	0.15	Bal.
AA6181	7/10	0.60-1.00	0.80-1.20	0.10	0.10	0.45	0.15	0.10	0.20	0.15	Bal.

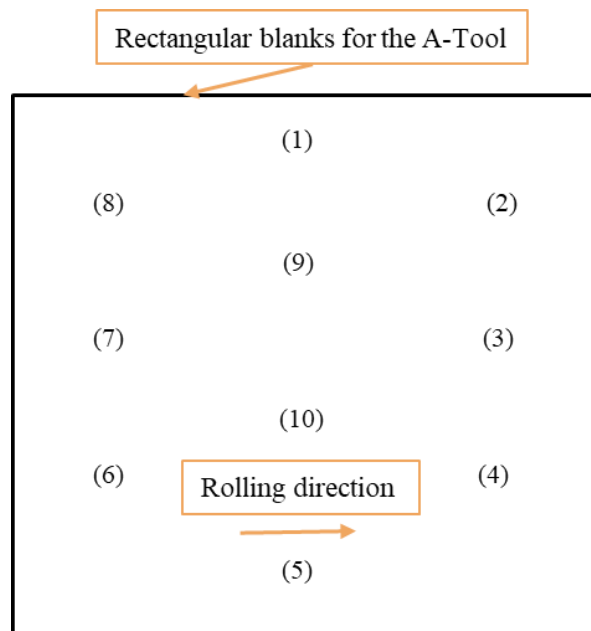


Figure 24 Schematic illustration of the measurement points for the analysis of surface roughness and lubricant amount

Lubricant amount and surface roughness  $R_a$  were measured at upper and lower side for blanks AF1-AF4. Surface roughness was measured using the mobile roughness device HOMMEL-ETAMIC W5 (Jenoptik, Jena, Germany) and lubricant amount was measured using oil film measurement device AMEPA OFIS (AMEPA GmbH, Würselen, Germany). Figure 24 illustrates the positions of measurement points marked (1)-(10). An average value for lubricant amount and surface roughness  $R_a$  was calculated from 10 measurements.

### 3.2 Uniaxial tensile test

Uniaxial tensile tests were performed for characterizing properties of investigated blanks. The tests were conducted according to DIN EN ISO 6892-1 using Zwick-Roell Z100 (Zwick-Roell, Ulm, Germany) tensile testing machine. The investigated mechanical properties include yield strength  $R_{p0.2}$ , ultimate tensile strength  $R_m$ , uniform strain  $A_g$ , fracture strain  $A_{80}$ , normal anisotropy ( $r$ -value) and strain hardening exponent ( $n$ -value). The uniaxial tensile tests were conducted for blanks AF1-AF3 using a quasi-static strain rate of 0.0067 1/s. Note that the material properties of blanks AF1 and AF4 are identical since the only difference between these blanks is lubrication. An average value for each material property was calculated from five tests. The bone-shaped samples for the tensile test had geometry defined according to DIN 50125 as shown in Figure 25 (a). The tensile test samples were wire eroded in rolling direction (RD), diagonal direction (DD) and transverse direction (TD). Moreover,  $r$ -values and  $n$ -values were estimated for a strain range of 2-20% according to ISO 10113 and ISO 10275, respectively. Extensometers shown in Figure 25 (b) had a gauge length of 80 mm and a gauge width of 20 mm. The planar anisotropy was calculated using Equation (6) with  $r_0$ ,  $r_{45}$ ,  $r_{90}$  representing the  $r$ -values in RD, DD, and TD directions, respectively.

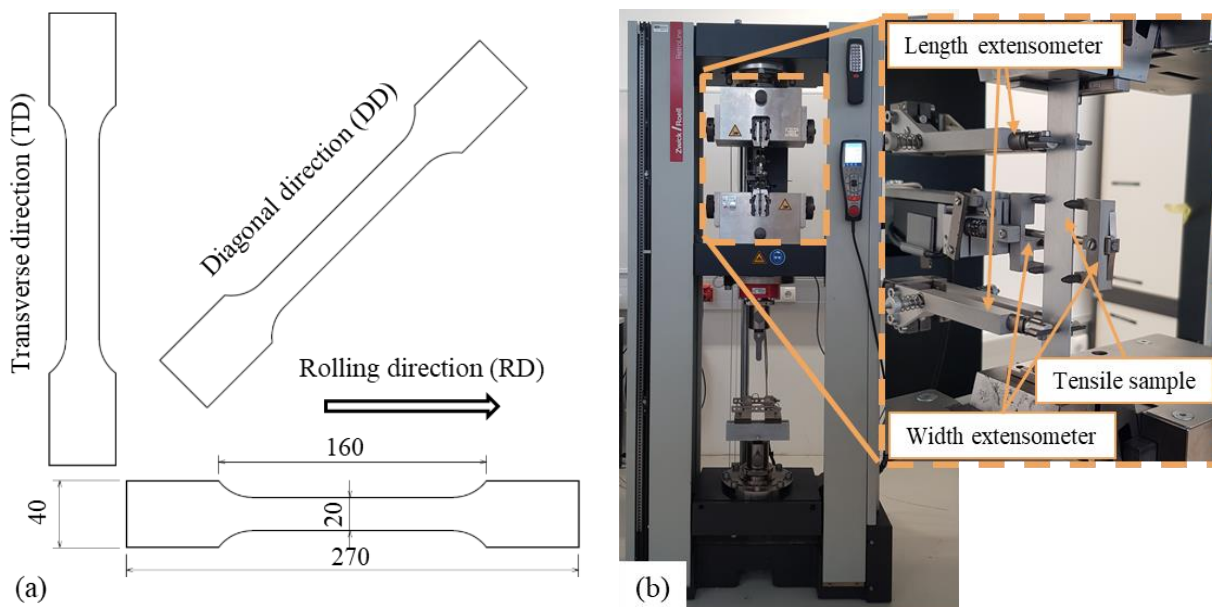


Figure 25 (a) Tensile test samples with respect to rolling direction and (b) Tensile testing setup

The effect of elevated strain rates on the strengthening behavior of blanks AF1-AF3 was analyzed using the testing machine INSTRON ElectroPuls E10000 (Instron, Norwood, USA). The bone-shaped tensile test samples were wire eroded in RD with a total length of 100 mm and a width of 12.5 mm in the narrowed area. Uniaxial tensile tests were performed at strain rates of 0.001 1/s, 0.1 1/s and 1 1/s. The lowest strain rate of 0.001 1/s represented the quasi-static strain rate. The highest strain rate of 1 1/s is in a similar range to the maximum, locally occurred strain rates during deep drawing of blanks at the forming velocity of 100 mm/s. The straining of the samples was evaluated by the traverse movement.

### 3.3 Stack compression test

The strengthening behavior of Al-Mg-Si blanks at comparatively higher strains than obtained by tensile testing was investigated by performing stack compression tests. The resulting biaxial stresses may slightly differ from the uniaxial stresses obtained by the tensile test. However, the tendency of the obtained stress-strain curve helps determine the tendency of the so-called flow curve, which is an essential part of material cards in numerical forming simulations. According to the standard for compression of metallic cylinders ISO 16808, the diameter and the height of the stacked sample should have a ratio of 1. Thus, 10 disks with a thickness of 1 mm and a diameter of 10 mm were stacked with regard to the rolling direction prior to compression. The compression of the stacked sample was conducted with a constant forming velocity of 5 mm/min. The relative displacement of the upper and lower cylinder was measured using the digital image correlation (DIC) system GOM ARAMIS (Carl Zeiss GOM Metrology GmbH, Braunschweig, Germany). However, the stack compression test is only valid for a period of uniform deformation i.e., before the bulging of the stacked sample starts. Figure 26 shows the shape of stacked disks (a) in a non-deformed state and (b) shortly before bulging of the stack (start of non-uniform deformation). Engineering stresses were calculated using Equation (10) with  $F_{comp}$  as compression force and  $D_{disk}$  as the initial diameter of disks. Engineering strains were calculated using Equation (11) with  $x$  representing the vertical deformation of the stack and  $h_0$  representing the initial height of the stack. True stresses and true strains were calculated using Equation (3) and (4), respectively. The flow curves obtained with this testing method were compared with the flow curve obtained from the tensile test in RD and the bulge test.

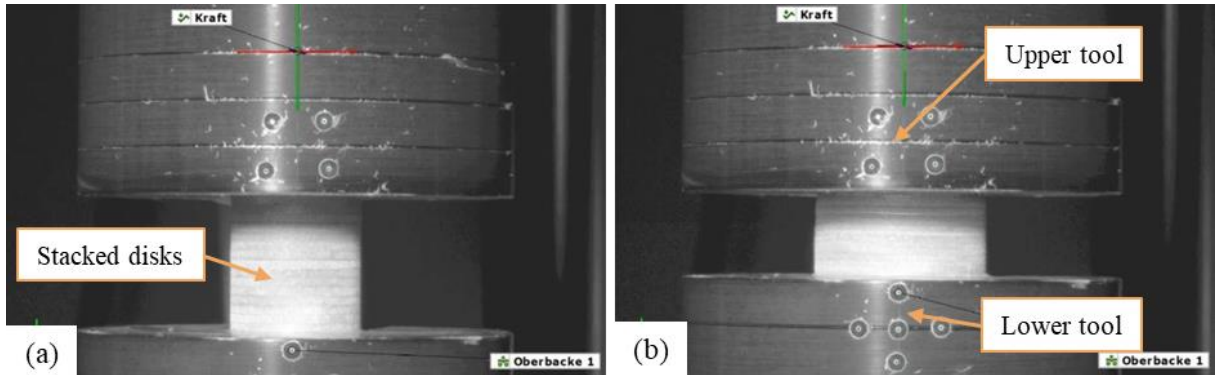


Figure 26 Stack compression tests (a) at the first contact and (b) at the end of the test

$$\sigma = \frac{F_{comp}}{D_{disk}} \quad (10)$$

$$\varepsilon = \frac{x}{h_0} \quad (11)$$

### 3.4 Bendability

The bendability of blanks AF1-AF3 was investigated by performing a plate bending test according to VDA 238-100. Figure 27 shows an aluminum plate placed in the plate bending fixture (a) at the start and (b) at the end of the bending test. Plates dimensioned 60 mm × 60 mm were placed at two support rollers with a gap of 2 mm, and each of the support rollers had a diameter of 30 mm. Subsequently, plates were bent perpendicular to the rolling direction using a punch with a tip radius of 0.2 mm. The test ended when the bending force decreased for 30 N after reaching the maximum, indicating minor cracking at the outer surface radius of the plate. However, the bendability was characterized using a maximum bending angle,  $\alpha_{max}$ , determined analytically at the moment of reaching the maximum bending force as proposed by the standard. An average value from five tests was calculated for  $\alpha_{max}$ .

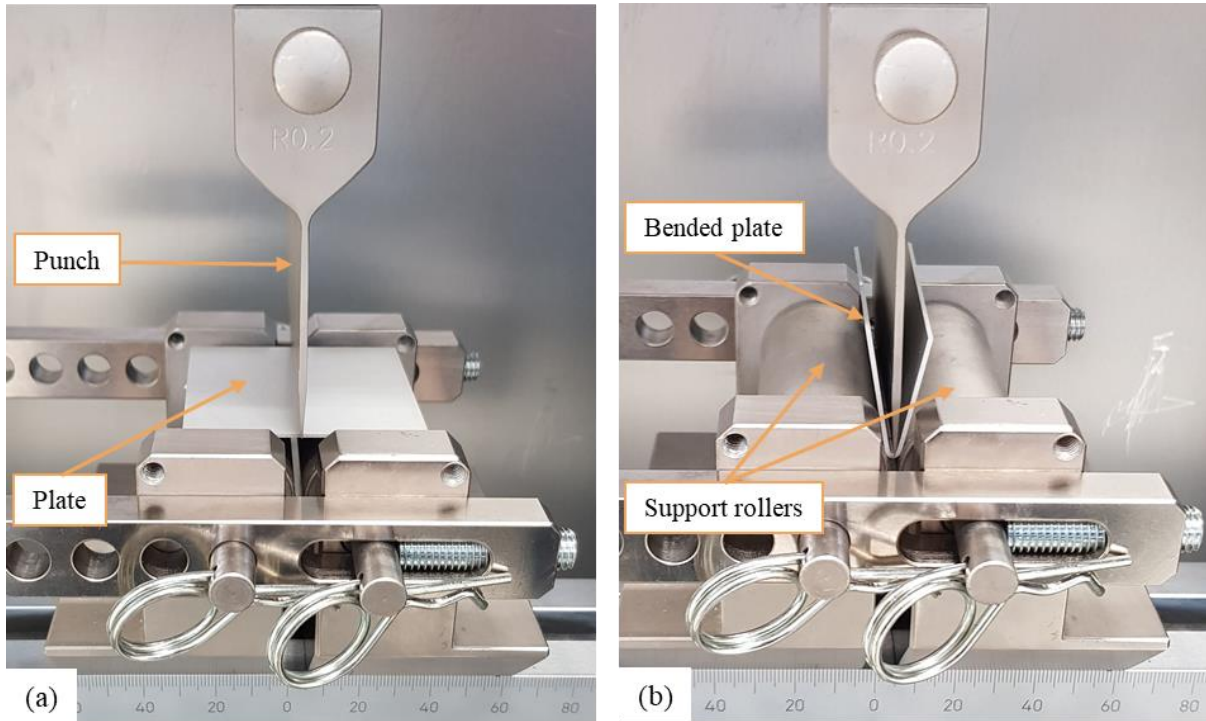


Figure 27 Plate bending test fixture with an Al-Mg-Si alloy plate at the (a) start and (b) end of the test

Moreover, hemming operations are typically performed in edge areas of car outer panels, which were previously exposed to a certain amount of straining during deep drawing. For investigating the effect of straining on the bendability, stripes of blanks AF1-AF3 were pre-strained for 10% prior to cutting 60 mm × 60 mm plates. The straining reduced the thickness of the plates to 0.93 mm. Accordingly, the distance between the support rollers was changed to 1.86 mm for this series of plate bending tests.

### 3.5 Forming limits

Forming limits of blanks AF1-AF3 were characterized using a forming limit curve (FLC) determined by performing Nakajima tests according to ISO 12004. Figure 28 (a) schematically illustrates the Nakajima test setup consisting of die, punch, and blankholder. A lubricated blank sample clamped between the die and the blankholder, was formed using the punch until cracking. Material flow from the blankholder area was restricted by block beads. Samples with different geometries shown in Figure 28 (b) were used to induce a specific strain state in the central area of the sample prior to cracking. The tests were performed after 1,3,6 and 18 months of NA.

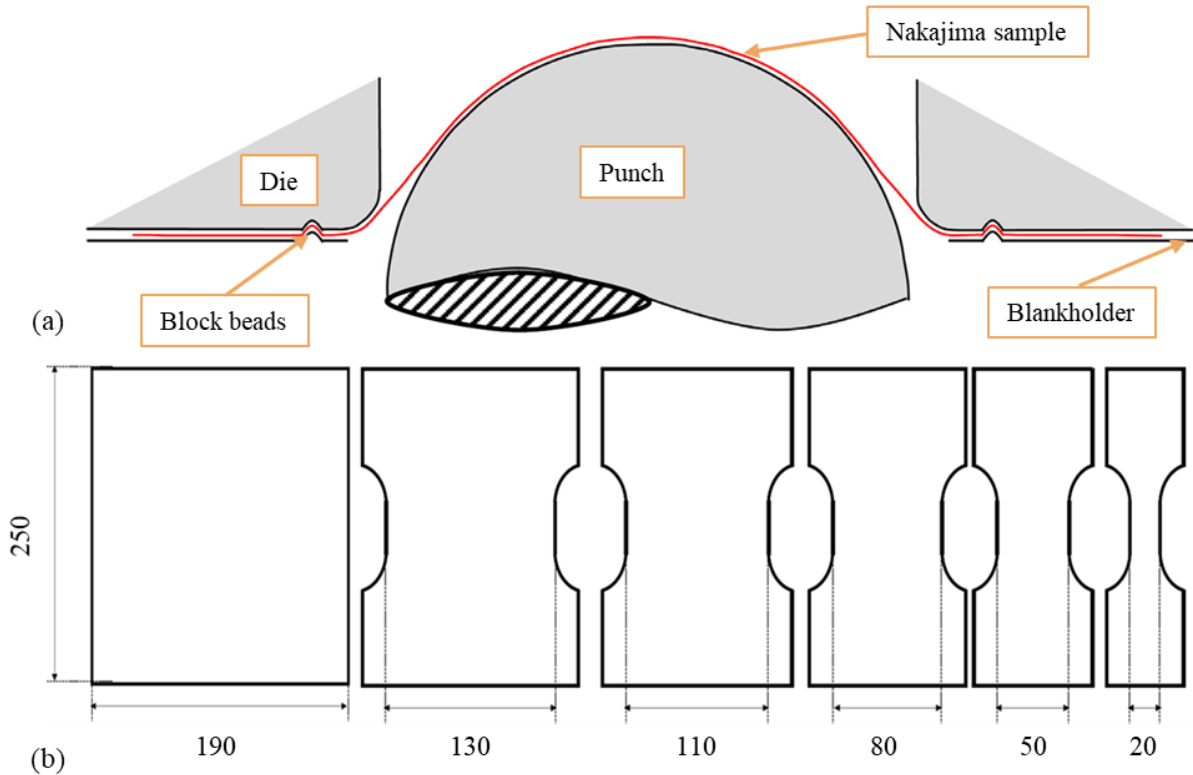


Figure 28 (a) Illustration of setup for the Nakajima test and (b) sample geometries (adapted from [75])

### 3.6 Formability

The influence of NA on the formability of blanks AF1-AF4 was investigated by performing deep drawing tests using two different tools, i.e., (i) complex tool (A-Tool) with closed die and (ii) cross-shaped tool (CS-Tool) with open die. The formability was investigated at two constant forming velocities of 10 mm/s and of 100 mm/s. The strain rates occurring during forming with the low forming velocity of 10 mm/s were in a similar range to quasi-static strain rates. However, the high forming velocity of 100 mm/s, which is close to an industrial range of forming velocities, induced significantly higher strain rates during forming. Thus, the effect of strain rate on the formability of Al-Mg-Si alloy blanks was also investigated.

#### 3.6.1 A-Tool

The active components of the A-Tool, i.e., the die, the punch and the blankholder are shown in Figure 29 (a). The A-Tool, originally introduced by AUDI (AUDI AG, Ingolstadt, Germany) was designed for the formability analysis of 1 mm-thick Al-Mg-Si alloys blanks for car outer panel application. Thus, the formed components using the A-Tool consisted of typical car outer panel features such as door handle cup, design ridges with and without sheet flow, 3D corners, and complex radii as shown in Figure 29 (b). Due to the closed die, each formed component obtained the same geometry, so variation of the drawing depth was not possible. Therefore, the formability of the investigated Al-Mg-Si alloys blanks dimensioned 472 mm × 435 mm was characterized by varying the BHF. The deep drawing procedure consisted of 3 steps, i.e., (1) tool cleaning, (2) preliminary tryouts, and (3) formability characterization. In step (1), the A-Tool was cleaned using ethanol and a service cleaner to remove the residual accumulations of lubricants and dirt. In step (2), 15 aluminum blanks were formed with a BHF of 300 kN and with a forming velocity of 100 mm/s. In this step, the lubricant film was stepwise transferred from the blanks to the active surfaces of the A-Tool to achieve steady tribological conditions during formability characterization. In step (3), the BHF was stepwise increased by 20 kN until visible necking or cracking appeared. Crack-free forming boundary and crack forming boundary were determined using 3 formed components of the same classification as schematically illustrated in Figure 29 (c). The crack free forming boundary refers to the maximum BHF ( $F_{max}$ ) that can be applied for forming failure-free components (free of crack and necking). The crack forming boundary refers to the minimum BHF that will lead to the forming of only cracked components. Between these two boundaries, a transition zone consisting of components with visible necking, cracked components, and crack-free components may be found. The formed components were visually evaluated. Necking or cracking occurred at the corner marked with the red arrow in Figure 29 (b). Step (3) was repeated for the low forming velocity of 10 mm/s. Moreover, the A-Tool was equipped with a distance sensor and a load cell. The distance sensor measured the relative displacement of the active components of the A-Tool and the load cell was used for measuring the forming force that works at the punch during deep drawing.

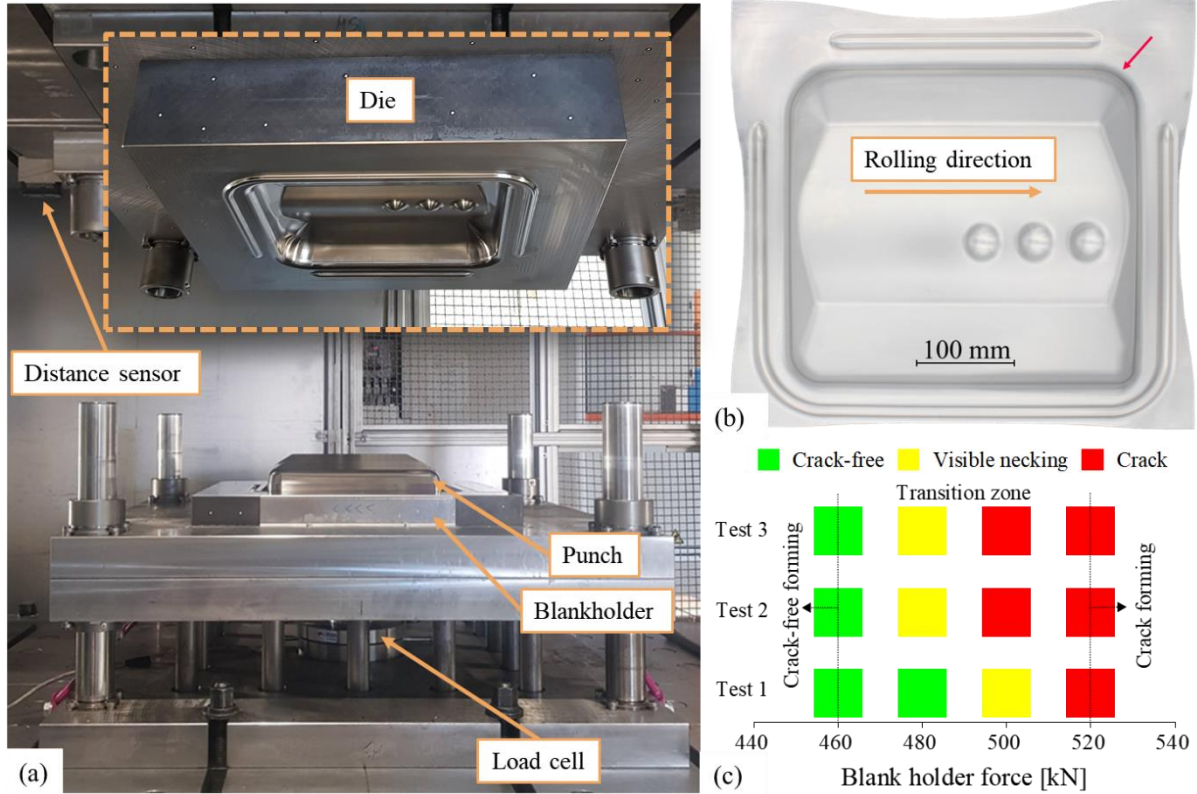


Figure 29 (a) A-Tool, (b) Blank component formed with the A-Tool and (c) formability characterization using the A-Tool

### 3.6.2 CS-Tool

The active components of the CS-Tool, i.e., the die, the punch and the blankholder are shown in Figure 30 (a). The CS-Tool can be used for the investigation of blank materials with a wide range of formability such as steel or aluminum blanks for blank thickness ranging from 0.5-3.5 mm. The formability of the circular blanks AF1-AF4 having a diameter of 280 mm was characterized by determining the drawing depth in a moment of crack initiation. The corners where cracks are initiated are marked with the red arrows in Figure 30 (b). Variation of drawing depth was possible due to the open die, so components with a height difference can be formed. The deep drawing procedure consisted of 3 steps, i.e., (1) tool cleaning, (2) preliminary tryouts, and (3) formability characterization. In step (1), residual lubricants and dirt were removed from the surface of the CS-Tool using ethanol and brake cleaner. In step (2), 15 aluminum blanks were formed with a BHF of 200 kN and with a forming velocity of 100 mm/s. In step (3), cross-shaped components were formed until cracking. The moment of cracking was determined using an accelerometer, a distance sensor, and a load cell. In the moment of cracking, blanks produce vibrations which can be captured by the accelerometer. Moreover, cracking of the blanks is also associated with the forming force maximum, which can be used for verifying the accuracy of the accelerometer as shown in Figure 30 (c). Therefore, the formability of investigated Al-Mg-Si blanks was characterized by the maximum drawing depth ( $D_{max}$ ), displayed by the distance sensor in a moment of cracking, which is captured by the accelerometer and the load cell. The forming tests with the CS-Tool were performed for each of the forming velocities, i.e., 10 mm/s and 100 mm/s,

at constant blankholder forces of 200 kN, 400 kN and 600 kN. An average value from 5 tests was calculated for each set of parameters. Forming the 1 mm-thick Al-Mg-Si alloy blanks was done using the die with a tool gap of 1.2 mm. An additional gap was necessary to prevent the clamping of blanks during forming since the die and the punch of the CS-Tool have vertical walls. On the contrary, the die and the punch of the A-Tool have conical walls, so an additional gap was not necessary.

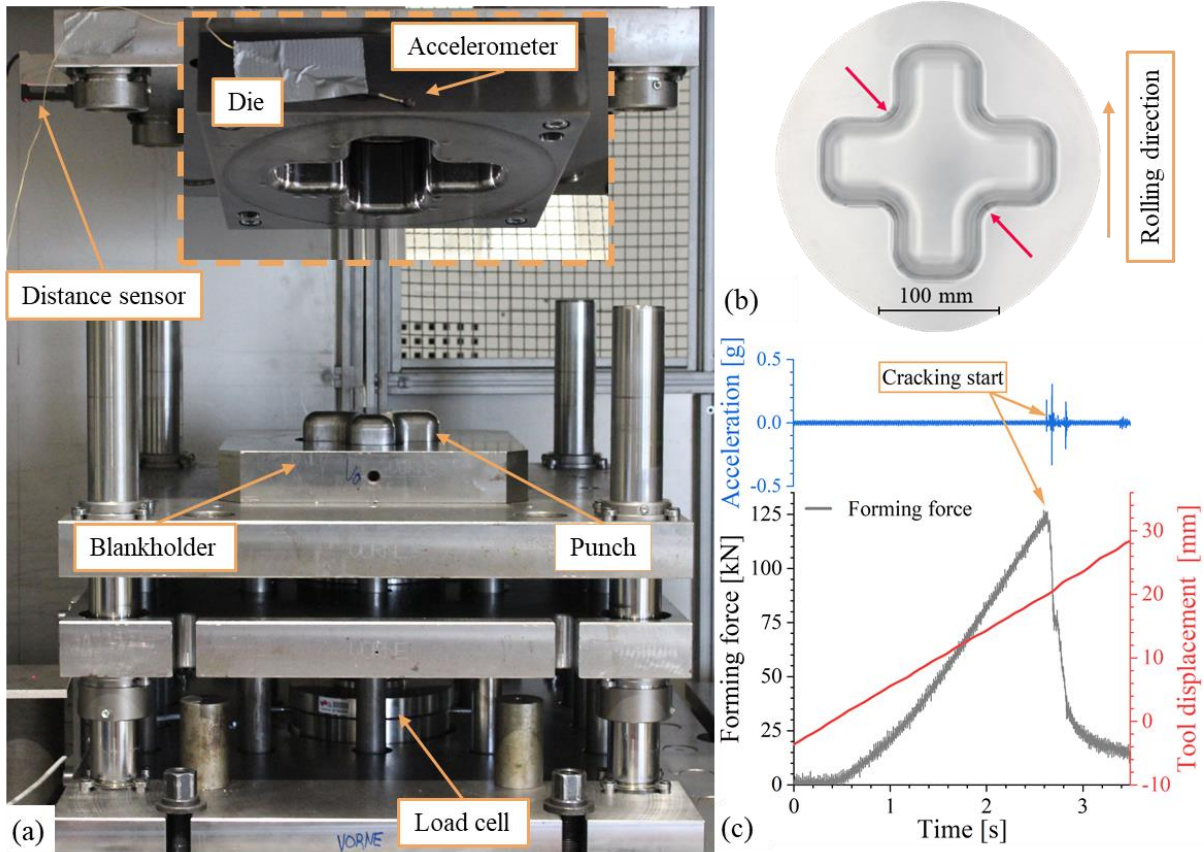


Figure 30 (a) Cross-shaped tool (CS-Tool), (b) component formed with the CS-Tool and (c) determination of maximum drawing depth with the CS-Tool

### 3.7 3D optical scanning

Finite element (FE) forming simulations are validated by comparing obtained results from simulation with experiments. Utilization of 3D optical scanning systems can provide digitalized data of experimentally formed components, that are necessary for validating the forming simulations. 3D optical scanning systems ARGUS and ATOS, developed by GOM Metrology (Carl Zeiss GOM Metrology GmbH, Braunschweig, Germany), were used for accurate data acquisition of experimentally formed components. Figure 31 (a) shows a component formed with the A-Tool, which is analyzed with the 3D optical scanning system ARGUS. This system is primarily used for the calculation of strain states at formed components, but it can also provide information about component geometry and thickness. However, this system requires extensive

preprocessing of blanks prior to forming. After the lubricant was removed from the blank AF1-AF4 using ethanol and brake cleaner, a rectangular dot pattern with a 1.5 mm distance between the circular dots were electrochemically etched at the blank surface using electrolyte 8090 from the company Östling (Östling Marking Systems GmbH, Solingen, Germany). Furthermore, the initial lubricant type and amount were applied to the blank surfaces, which were measured and verified using the lubricant film measurement device AMEPA OFIS. Finally, the components were formed using the A-Tool and the CS-Tool, and the induced strain states were evaluated based on distortion of the dot pattern. For the analysis, the components were photographed from different positions and directions, which were later determined by the software ARGUS based on the reference markers. Figure 31 (b) shows the 3D optical scanning system ATOS, which is used for capturing the component geometry. This system does not require the preprocessing of blanks, and it can be used for digitalizing various components and part geometries. Adhesive reference points and a tiny layer of anti-reflex spray were applied to the component surface. Subsequently, the component geometry was scanned using the ATOS Triple Scan camera from different positions. For exact identification, at least 4 reference points should be visible at the component surface. The reference points were used for defining the camera positions and for assembling the separate scans into one unit. The outer side of the formed components was scanned for a springback analysis. However, both sides (inner and outer) of the components were captured in one scan for the thickness analysis.

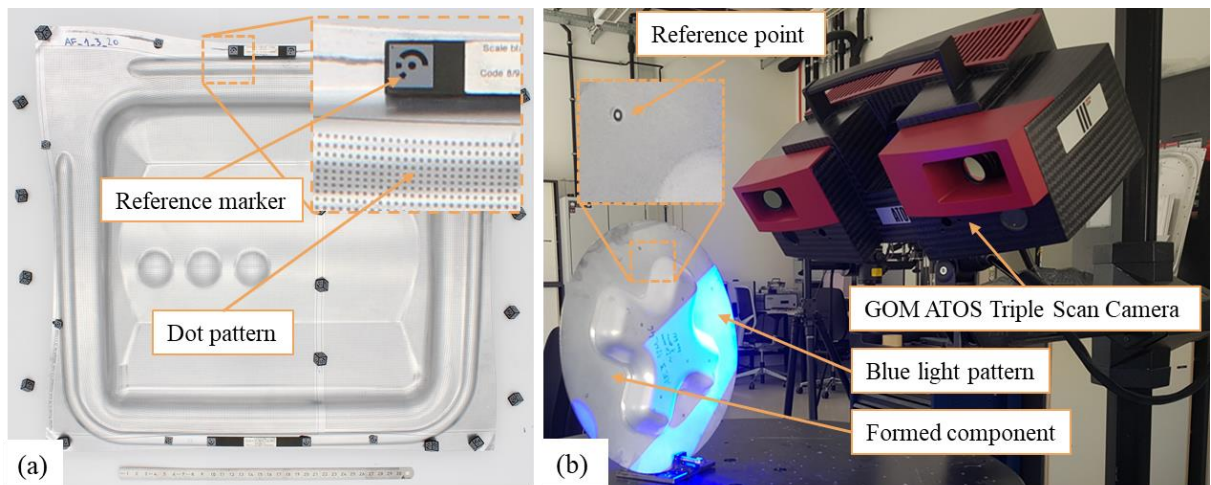


Figure 31 3D optical scanning of the components using (a) ARGUS and (b) ATOS

### 3.8 Pin-on-plate tribometer

Tribological conditions observable during the deep drawing of aluminum blanks were investigated by using a pin-on-plate tribometer shown in Figure 32 (a). A combination of steel pins and aluminum plates was used for an adequate representation of contact between the deep drawing tools and Al-Mg-Si alloy blanks. The aluminum plates with the size 68 mm × 27 mm × 1 mm were cut from blanks AF1-AF4. The steel pin, whose geometry is shown in Figure 32 (b), had a surface roughness  $R_a$  of 0.5  $\mu\text{m}$  and hardness of 55 HRC, which is similar to the surface

roughness and hardness of the deep drawing tools. After the normal force ( $F_N$ ) was applied, the steel pin slid for 40 mm over the aluminum plates in RD with a constant sliding velocity of 1 mm/s. Fresh pins and plates were used for each friction test, which consisted of 3 repetitions as illustrated by wear tracks in Figure 32 (a). The monitored frictional force ( $F_F$ ) was used for calculating the coefficient of friction (CoF) according to Equation (9). An average CoF was calculated from 2-3 friction tests for each condition. The normal force was used for the calculation of the nominal contact pressures between the pin and the plate. The influence of 4 nominal contact pressures of 4 MPa, 8 MPa, 12 MPa, and 16 MPa on the CoF was investigated in friction tests. This range of contact pressures is typically occurring in the flange area of the deep drawing tools [63,101,102]. Moreover, the changes in CoF at comparatively low contact pressures are higher than at more elevated contact pressures [103,104]. Minor changes of CoF are expected at contact pressures higher than 16 MPa.

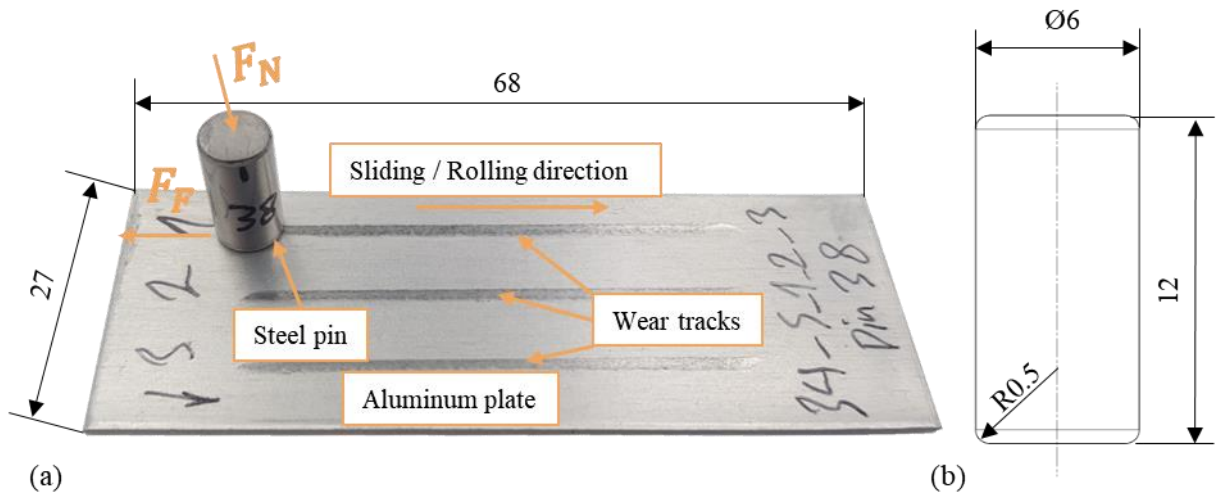


Figure 32 (a) Test setup for pin-on-plate tribometer and (b) geometry of the steel pin

## 4 Finite element (FE) forming simulations

Design and manufacturing of deep drawing tools have a notable share in the production costs of car outer panels. Numerical simulations of forming processes are nowadays essential for cost and time savings in the automotive industry. Parallel to providing information about production feasibility, accurate simulation mode can also reduce production costs and time by avoiding the production of new tool parts, reducing time and effort for rework on active tool surfaces, or avoiding an eventual purchase of new blank materials with better formability. Thus, it is necessary to consider as many influencing factors as possible. Commercial software for this application can already provide good results by using a constant friction coefficient as a friction model. Therefore, the focus of this work was set on tribological conditions in a deep drawing for improving the accuracy of numerical forming simulations. The forming simulation was built on three models, i.e., the simulation model for defining the part geometry and process parameter, the material model for describing the forming behavior of blank material, and the friction model for describing the tribological condition during deep drawing.

### 4.1 Simulation model

Numerical forming simulations were performed using a commercial FE simulation software AutoForm R8 (AutoForm Engineering GmbH, Pfäffikon, Switzerland). Figure 33 shows the simulation models consisting of the die, the punch, the blankholder, and the blanks for (a) the A-Tool and (b) the CS-Tool. The simulation model of the A-Tool was derived from the actual tool geometry, which was scanned using the 3D optical scanner ATOS, whereas the CAD geometry of the active tool parts was used for the CS-Tool. The active tool parts, which were defined as rigid bodies, were meshed using triangular shell elements with a size of 1 mm. The rectangular blanks for the A-Tool and the circular blanks for the CS-Tool were meshed with triangular elastoplastic shell elements with 11 integration points across the blank thickness. The constant mesh size of 1 mm was defined for the circular blanks whereas the initial mesh size of 2 mm for rectangular blanks could be refined to 1 mm during the forming simulation. The threshold for the mesh refinement, which occurred only in the area around drawbeads, was  $22.5^\circ$  for the maximum element angle and 0.22 mm for radius penetration. The meshing parameters were chosen based on the mesh sensitivity study so further reduction of the element size would lead to errors occurring during the forming simulation.

The forming simulation consisted of four steps: (1) blank positioning, (2) tool closing, (3) blank forming, and (4) springback simulation. In step (1), the blank was placed on blankholder, and the effect of gravity on the blank form was simulated. In step (2), the blank was clamped between the die and blankholder, and the blankholder force was applied. In step (3), the blank was formed with relative motion between the punch and other active tool parts. In step (4), which was performed after the relative motion ended, the elastic deformations were released from formed components by performing a free springback. The free springback refers to the simultaneous removal of all active tool parts, which leads to the release of elastic strains in the formed component. This is slightly different from the actual deep drawing process where the active tool parts slowly return to their initial position.

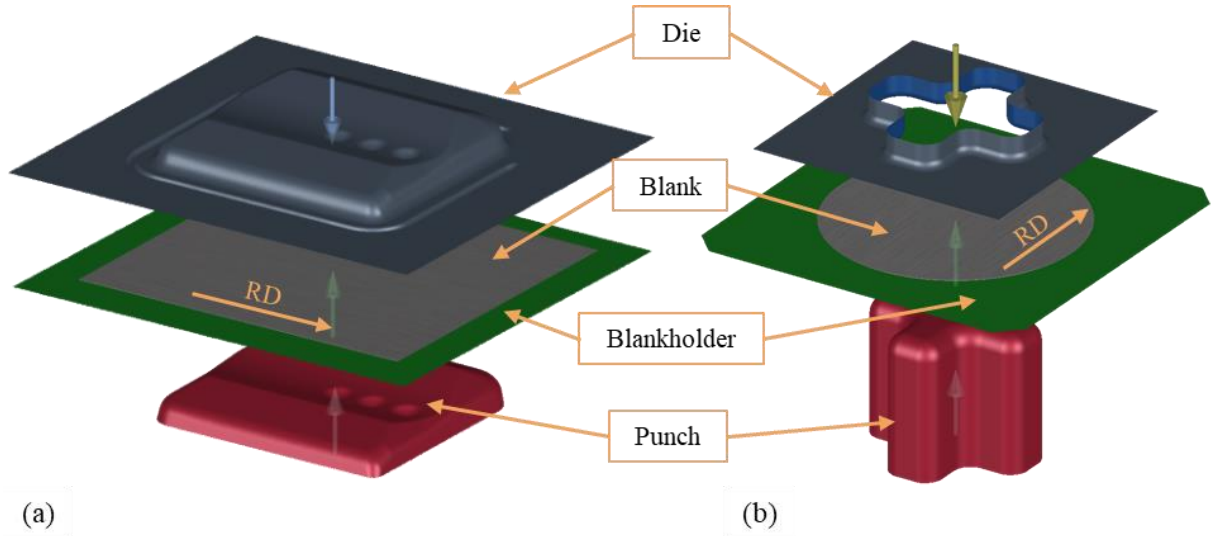


Figure 33 Simulation models of active tool parts for (a) the A-Tool and (b) the CS-Tool

Three types of numerical simulations were conducted. The first type of numerical simulation was conducted using the material data obtained after 3 months of NA. These simulations were conducted using the advanced friction model described in section 8.1 and a constant CoF. Numerically and experimentally obtained results were compared and extensively analyzed in terms of strains, thinning, forming force, and springback. Table 8 shows the process parameters used for forming components, that are utilized for validating the forming simulations. Experimentally obtained components were formed at relatively low forming velocities so only strain rates in the range of quasi-static strain rate were induced. For producing the components using the A-Tool, blankholder force was varied for each of the blanks AF1-AF4. However, the components formed using the CS-Tool were produced using a constant BHF of 400 kN and various drawing depths for each of the blanks AF1-AF4. The process parameters were chosen to induce a critical stress state in the components so a slight increase of the BHF for the A-Tool or of the drawing depth for the CS-Tool would result in failure. Yet, a small crack was observed for the component formed using the A-Tool and blank AF3. Other formed components were failure-free. The remaining two types of numerical simulations were focused on the changes in material properties during NA and the influence of elevated strain rates on the formability of blanks AF1-AF3. These forming simulations were conducted using the geometry of the A-Tool, and the numerically obtained results were evaluated using the FLD. Information about material models used in these forming simulations is provided in the following section.

Table 8 Process parameters for forming of the components used for validation of the numerical forming simulations at quasi-static strain rates

Tool	Formability criterion	AF1	AF2	AF3	AF4	Forming velocity
A-Tool	Blankholder force [kN]	360	500	500	600	10 mm/s
CS-Tool	Drawing depth [mm]	19.5	21.5	19.5	23.5	1 mm/s

## 4.2 Material model

The material model of investigated Al-Mg-Si alloy blanks consisted of a flow curve, yield locus, and FLC. Quasi-static flow curves determined after 3 months of NA for blanks AF1-AF3 are shown in Figure 34 (a). A detailed description of the calculation and extrapolation of the flow curves can be found in section 5.2. The transition between elastic and plastic deformation (start of material flow) is described using the yield locus. The start of the material flow depends on the stress state so it may vary for uniaxial tensile stresses and biaxial compressive stresses. Barlat89 [70] yield criterion with the constant  $M = 8$  was used for defining the yield locus of blanks AF1-AF3. This model accurately describes the yield behavior of aluminum alloys in numerical forming simulation [101,105,106]. This model also required normal anisotropy  $r_0$ ,  $r_{45}$  and  $r_{90}$ , which were determined by tensile testing. Potential failures of blanks in forming simulation such as necking or cracking were considered by means of FLC. An exceeding of strains over the FLC may result in failure. The FLC determined after 3 months of NA for blanks AF1-AF3 are shown in Figure 34 (b).

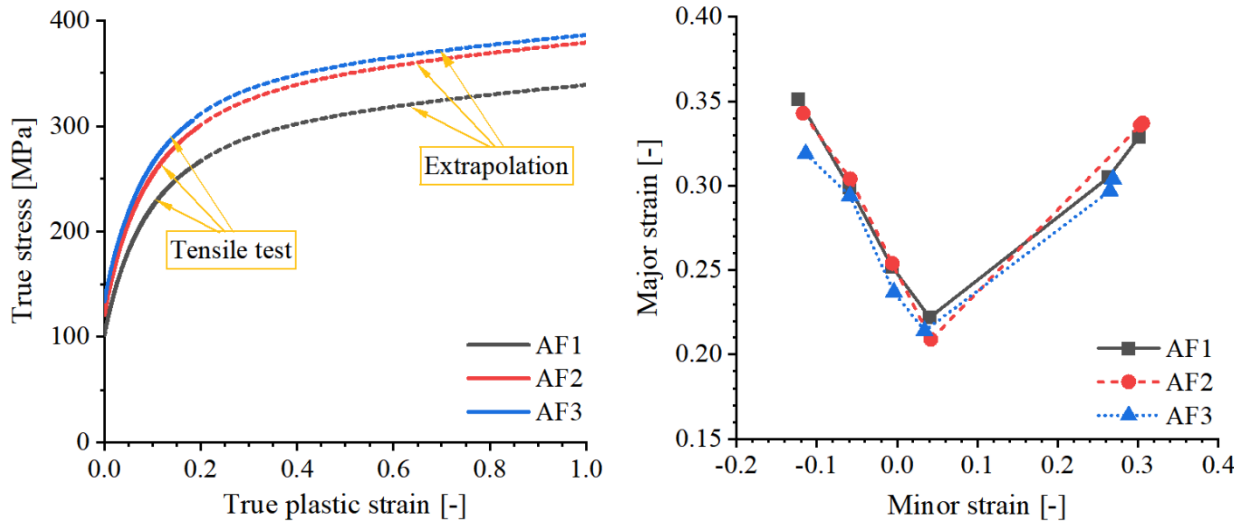


Figure 34 (a) Flow curves and (b) FLC determined after 3 months of NA

The second type of simulation analyzed the influence of variable material properties on the formability of investigated blanks within 18 months of NA. The strengthening affected primarily the flow curves but other material properties such as  $r$ -values were also adapted. The forming simulations were conducted for blanks AF3 using the advanced friction model, the blankholder force of 500 kN and the forming velocity of 10 mm.

The forming behavior of blanks AF1-AF3 at the high forming velocity of 100 mm/s was numerically investigated in the third type of simulation. For this purpose, flow curves were determined at strain rates of 0.001 1/s, 0.1 1/s 1 1/s after 15 months of NA. The highest strain rate of 1 1/s was in a similar range to the maximum, locally induced strain rates during a deep drawing with the forming velocity of 100 mm/s. Table 9 shows experimentally determined highest blankholder force ( $F_{\max}$ ) for forming of failure-free components, which are also used in

forming simulations. Moreover, these simulations were also used for validation of advanced friction model at elevated sliding velocities.

Table 9 Process parameters used for forming of the components for validation of the numerical forming simulations

Tool	Formability criterion	AF1	AF2	AF3	AF4	Forming velocity
A-Tool	Blankholder force [kN]	300	440	360	500	100 mm/s

### 4.3 Friction model

Two friction models were used in numerical forming simulations, i.e., the Coulomb friction model (CF model), which is described by constant CoF, and the TriboForm friction model (TF model), which is generated using software TriboForm R3.0 (TriboForm Engineering, Enschede, Netherlands). Two different CoF were used for the CF model, 0.10 for blanks lubricated with the E 1 lubricant (AF1-AF3) and 0.08 for blanks lubricated with PL 39 SX lubricant (AF4). The CoF values were chosen based on the best fit between experimentally and numerically determined forming forces curves. The increase rate of the forming forces curve can be significantly influenced by the CoF so a higher CoF leads to an increase of the forming forces [101]. The TF models for blanks AF1-AF4 were generated based on the results from the pin-on-plate friction tests and a default TriboForm model for Al-Mg-Si alloy blanks with hotmelt lubricant. The default model considers the CoF dependency on contact pressure, sliding velocity, temperature, and strain. Hence, the results obtained from the friction tests were used to fit the default model for specific blank type. Although the contact pressure was the only varied parameter in the friction tests, the generated TF models also considered the influence of sliding velocity and temperature on CoF. However, for better correlation between numerical forming simulations and deep drawing experiments, the experimentally obtained components after 3 months of NA were formed at room temperature and with slow forming velocities. Additional forming simulations were performed with the material data obtained after 15 months of NA, for validating the TF models at elevated sliding velocities.

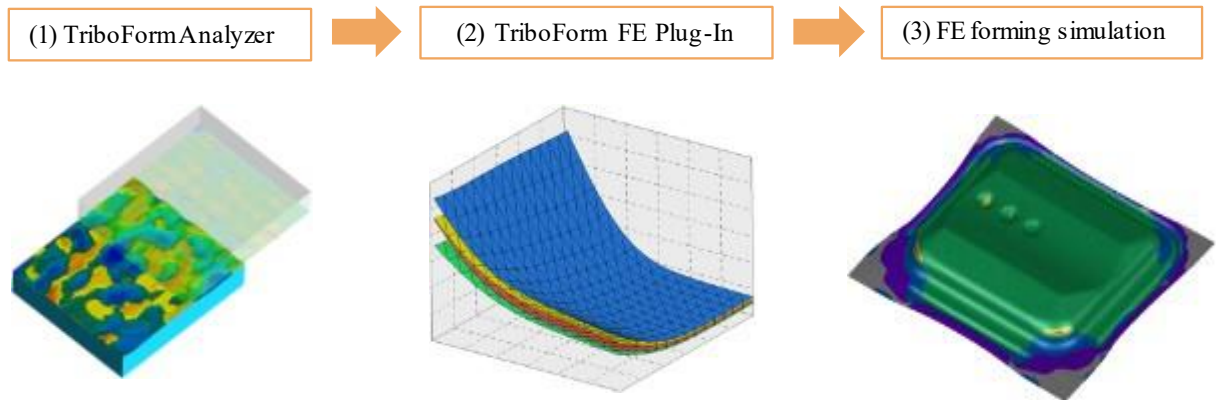


Figure 35 3 mandatory steps in generation and implementation of the TriboForm friction model

The general procedure for generating the customized TF models and performing numerical forming simulations with this model is shown in Figure 35. In step (1), the basic data about the

blank and the tool is imported into TriboForm Analyzer. This step requires information about the type and alloy series of the blank material, surface topography of the blank and the tool, type and amount of lubricant, and experimental results from friction tests. Figure 36 shows the surface topography of the EDT blanks in (a) dry (b) lubricated condition and (c) of the deep drawing tools with MF texture. The surface topographies with the size of about  $0.5 \text{ mm} \times 0.5 \text{ mm}$  were captured by using Keyence VHX-6000 3D digital microscope (Keyence, Osaka, Japan). A surface roughness  $S_a$  of  $0.43 \text{ }\mu\text{m}$  was measured for the tool and of  $0.80\text{-}0.90 \text{ }\mu\text{m}$  for blanks AF1-AF3. Information about the surface topography of the blanks and the tool was used for accurate calculation of local contact pressures during deep drawing operation. However, the computation time was not significantly affected compared to the numerical forming simulation with the CF model. In step (2), the FE Plug-in for the simulation software AutoForm R8 was generated. In step (3), the lubrication file was generated in AutoForm and added to the material model for each of the blank types. Subsequently, the numerical forming simulation was conducted.

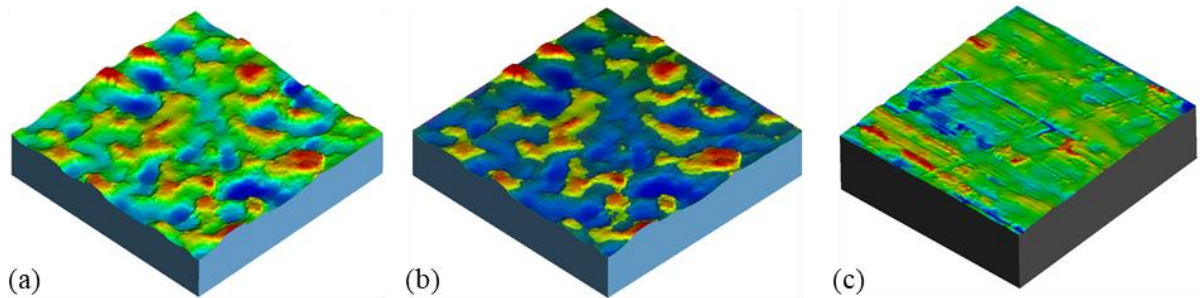


Figure 36 EDT surface of investigated blanks in (a) dry and (b) lubricated condition; (c) surface topography of the tool with MF texture

## 5 Material characterization

### 5.1 Uniaxial tensile test

#### 5.1.1 Tensile strength

Figure 37 (a) shows a constant increase in the yield strength within 1-18 months of NA as a result of the clustering effect. Generally, the highest yield strength was observed for the samples cut in RD. After 1 month of NA, the yield strength of blanks AF1 in RD was about 99 MPa. For the same period, an increase in Si and Mg content of AF2 blanks promoted the yield strength to 117 MPa, but higher Mg content and higher Mg/Si ratio of AF3 blanks improved the yield strength to 129 MPa. The yield strength in DD was about 6-9 MPa lower than the yield strength in RD. However, the yield strength in TD was only 1-2 MPa lower than the yield strength in DD. The yield strength of AF3 blanks remained highest for the entire NA time, followed by AF2 blanks and AF1 blanks. An increase of yield strength was comparatively similar for all three directions (RD, DD, and TD) within 1-18 months of NA reaching an average increase of about 21.5%, 19.5%, and 24.5% MPa for AF1, AF2, and AF3 blanks, respectively.

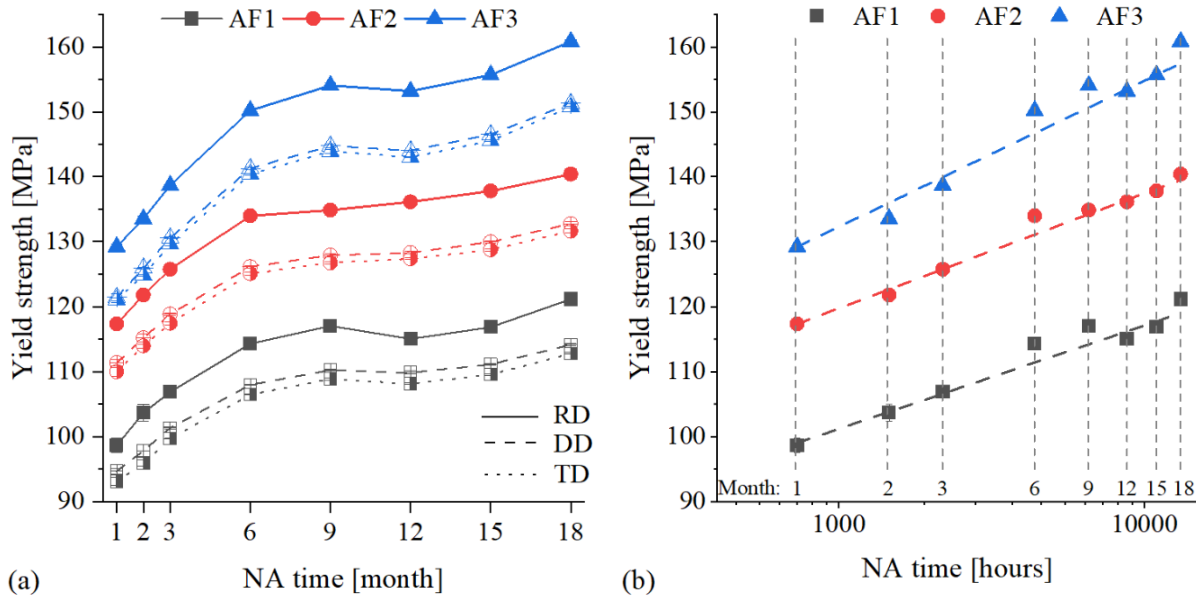


Figure 37 (a) NA influence on the yield strength of blanks AF1-AF3 and (b) logarithmic increase of yield strength in RD

Strengthening of blanks was more dominant at the beginning of NA and generally decelerated with the increasing NA time. Thus, the strengthening of blanks AF1-AF3 can be represented as a logarithmic function over time using Equation (12) as shown in Figure 37 (b). The constants used for describing the logarithmic progression of yield strength in RD are shown in Table 10. The highest constant  $k$ , representing the fastest kinetic of NA, was observed for blanks AF3

followed by AF2 and AF1 blanks. Obviously, higher Mg content promoted the strengthening of blanks AF3. NA kinetics of blanks AF2 was only marginally higher than NA kinetics of blanks AF1 due to slightly higher Si and Mg content. However, the highest initial yield strength  $\sigma_0$  was observed for blanks with the highest Si content, i.e., blanks AF2. This indicated that Si clusters are formed before Mg clusters and Mg/Si co-clusters [30,34,107]. Hence, it can be concluded that the kinetic of NA was primarily affected by Mg content and Mg/Si ratio but the initial yield strength  $\sigma_{1h}$  was primarily affected by Si content. That Si affects primarily the initial yield strength  $\sigma_{1h}$  and has very little influence on NA kinetics  $k$  was also reported elsewhere [30]. Prillhofer et al. [43], Zhong et al. [53] and Simões et al. [48] reported comparatively similar NA kinetics for AA6016. Moreover, NA kinetics of similar trend like for blanks AF1-AF3 were also reported for other Al-Mg-Si alloys in other research works [25,27,52]. However, a notable acceleration of NA kinetics can be achieved by increasing the Cu content, which is reported for AA6013 by Prillhofer et al. [43] and for Al-Mg-Si alloy with 0.82 wt.% of Si and 0.76 wt.% of Mg by Esmacilli and Lloyd [30].

$$\sigma_y = \sigma_{1h} + k \log(t_{NA}) \quad (12)$$

Table 10 Parameters used for describing the logarithmic propagation of yield strength in RD

Alloy	$\sigma_{1h}$ [MPa]	$k$ [MPa]
AF1	53.38	15.93
AF2	66.67	17.69
AF3	64.81	22.50

NA influence on the ultimate tensile strength was comparatively similar to NA influence on the yield strength. The highest ultimate tensile strength was observed for blanks AF3, followed by blanks AF1 and AF2 as shown in Figure 38. After one month of NA, the ultimate tensile strength in RD of 208.5 MPa, 236 MPa, and 243 MPa was measured for blanks AF1, AF2, and AF3, respectively. Like the yield strength, the ultimate tensile strength in DD was about 7-11 MPa lower than in RD. Moreover, the ultimate tensile strength in TD was about 1.5-2 MPa lower than in DD. An increase of ultimate tensile strength within 1-18 months of NA due to the clustering effect was comparatively similar for all three directions (RD, DD, and TD) reaching an average increase of about 24.5 MPa, 24.5 MPa, and 31.5 MPa for blanks AF1, AF2 and AF3, respectively. Yet, the influence of NA on the strengthening of AF2 blanks in RD is of particular interest. After 1 month of NA, the ultimate tensile strength for blanks AF2 in RD was higher than the ultimate tensile strength for blanks AF3 in DD and TD. This was due to the higher strain hardening capacity of blanks AF2 than of blanks AF3, so this scenario was not observed for the yield strength. However, faster NA kinetic in blanks AF3 resulted in a higher ultimate tensile strength in each of both DD and TD after 18 months of NA compared to blanks AF2 in RD.

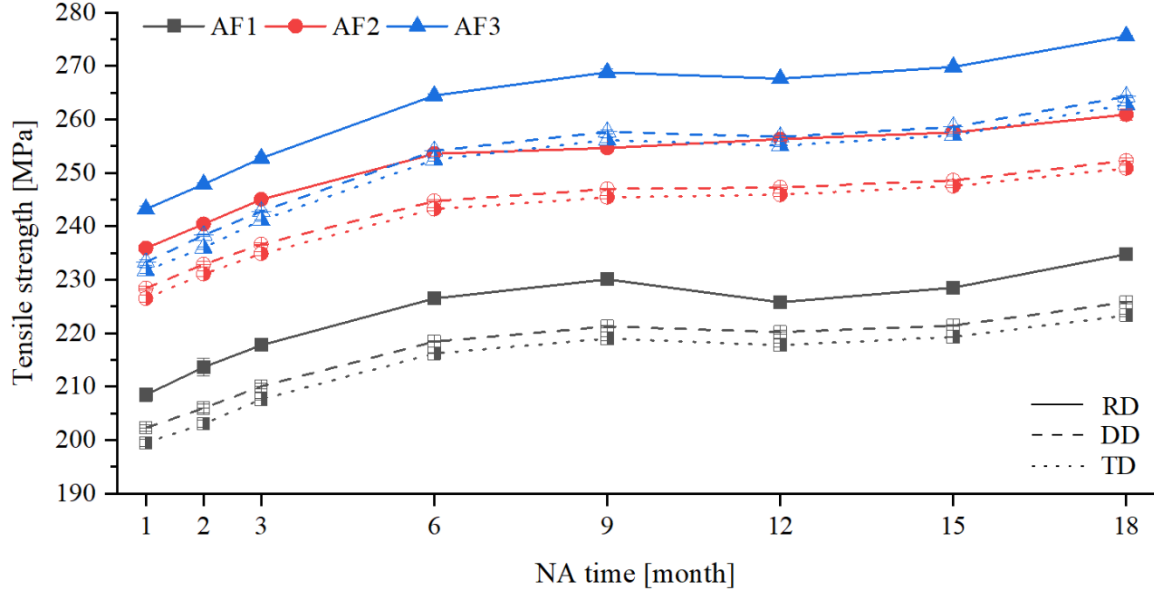


Figure 38 The influence of NA on the ultimate tensile strength for blanks AF1-AF3

### 5.1.2 Tensile ductility

The influence of NA on the uniform strain is shown in Figure 39 (a), (b), and (c) for blanks AF1, AF2, and AF3, respectively. After 1 month of NA, the highest uniform strains were observed in DD for blanks AF1 (26.1%) followed by blanks AF2 (25%) and blanks AF3 (24.5%). Slightly lower uniform strains were observed after using the tensile test samples in TD and in RD after 1 month of NA. Uniform strains measured in DD were about 23.4% for blanks AF1, 22.7% for blanks AF2, and about 22% for blanks AF3. In RD, uniform strains of about 22.6%, 22.1%, and 20.9% were measured for blanks AF1, AF2 and AF3, respectively. The uniform strains were inversely proportional to the yield and ultimate tensile strength of blank materials. Blanks with higher material strength exhibited lower ductility. Surprisingly, an additional increase of the strength due to NA had only minorly affected the uniform strains for each of the three directions. A minor decreasing trend can be identified for some of the curves such as for blanks AF2 and AF3 in DD. The decrease of the uniform strain within 1-18 months of NA was 0.6% for blanks AF2 and 0.8% for blanks AF1 in DD. However, this trend was not observed for the same blanks in RD and in TD and for blanks AF1 in each of the three directions. The decrease of the uniform strain at the end of NA was in the range of only 0.1-0.3%. Note that the increase of material strength within 1-18 months of NA was about 20% and higher. Therefore, it can be concluded that the uniform strain remained relatively constant within 1-18 months NA, and the influence of NA on the uniform strain is only minor. Similar trends were observed by Zhong et al. [53] for AA6016 and by Gu et al. [55] for AA6014 but with significantly higher fluctuation of the yield strength during NA. However, Simões et al. [48] observed a minor decrease in the uniform strains for AA6016 within 1-7 months of NA.

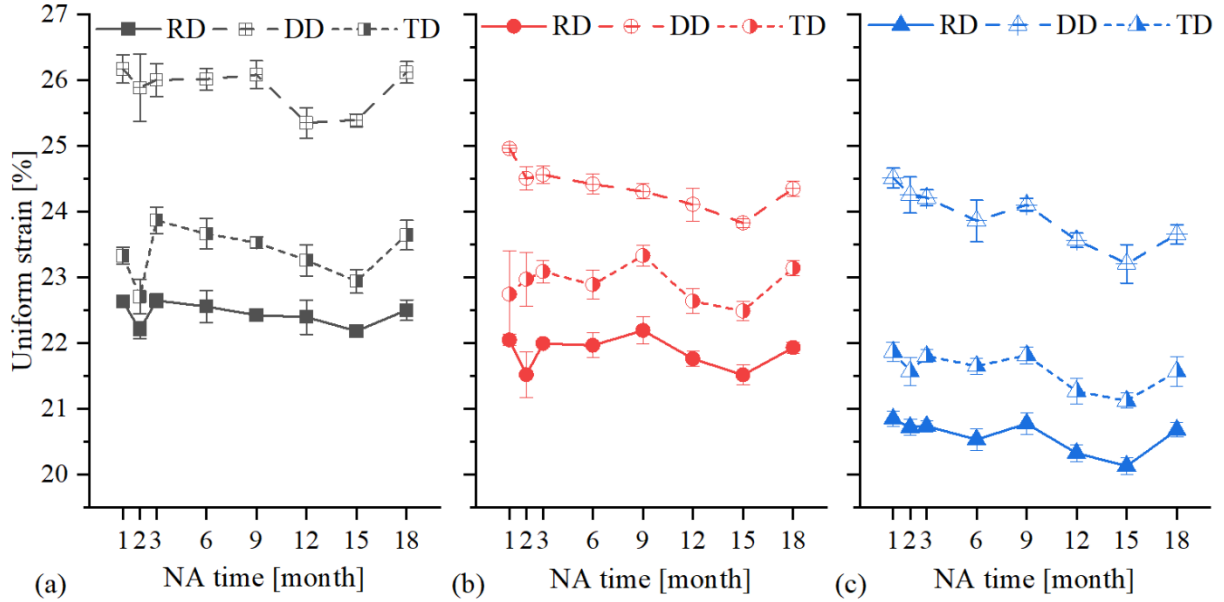


Figure 39 Influence of NA on the uniform strains of blanks (a) AF1, (b) AF2 and (c) AF3

The influence of NA on the fracture strain is illustrated in Figure 40 (a), (b), and (c) for blanks AF1, AF2, and AF3, respectively. The results revealed that the behavior of blanks is identical for the fracture strain as for the uniform strain. After 1 month of NA, the highest fracture strain was observed in DD for blanks AF1 (29.8%) followed by blanks AF2 (29.1%) and blanks AF3 (28%). Significantly lower fracture strains were observed for the tensile test samples in TD and in RD for the same period of NA. Fracture strains measured in DD were about 25.8% for blanks AF1, 26.8% for blanks AF2 and about 25.5% for blanks AF3. The fracture strains in RD of about 25.8%, 26.3%, and 25% were measured for blanks AF1, AF2, and AF3, respectively. However, the fracture strain in RD of blanks AF1 increased after 3 months of NA to about 27.5% and in DD to about 28%. Afterwards, the fracture strains of blanks AF1 remained relatively constant. The fracture strains of blanks AF2 increased by little within 1-6 months of NA reaching a maximum of about 27.5%, 30.6%, and 28.4% in RD, DD, and TD, respectively. Subsequently, the fracture strains remained relatively constant except for the tensile test samples in DD between 15-18 months. The fracture strains of blanks AF3 remained relatively constant during the NA for each of the three directions. Generally, the fluctuation and the scattering of the fracture strain results were higher than those of the uniform strain results but a clear trend, whether decreasing or increasing, was not identified. The high scattering of the fracture strains was primarily caused by the sample preparation. The wire-eroded samples were immersed during the cutting into a water bath that contained additives to prevent the corrosion of steel. Likely the interaction between the lubricant at blanks and the additives caused some surface defects, which led to a change in the fracture pattern of the tensile test samples as shown in Figure 41. The changes in the fracture pattern reduced the fracture strains determined within 1-3 months of NA. This phenomenon did not have a significant influence on the uniform strains. However, this effect was reduced when the samples were cleaned before or immediately after the wire eroding.

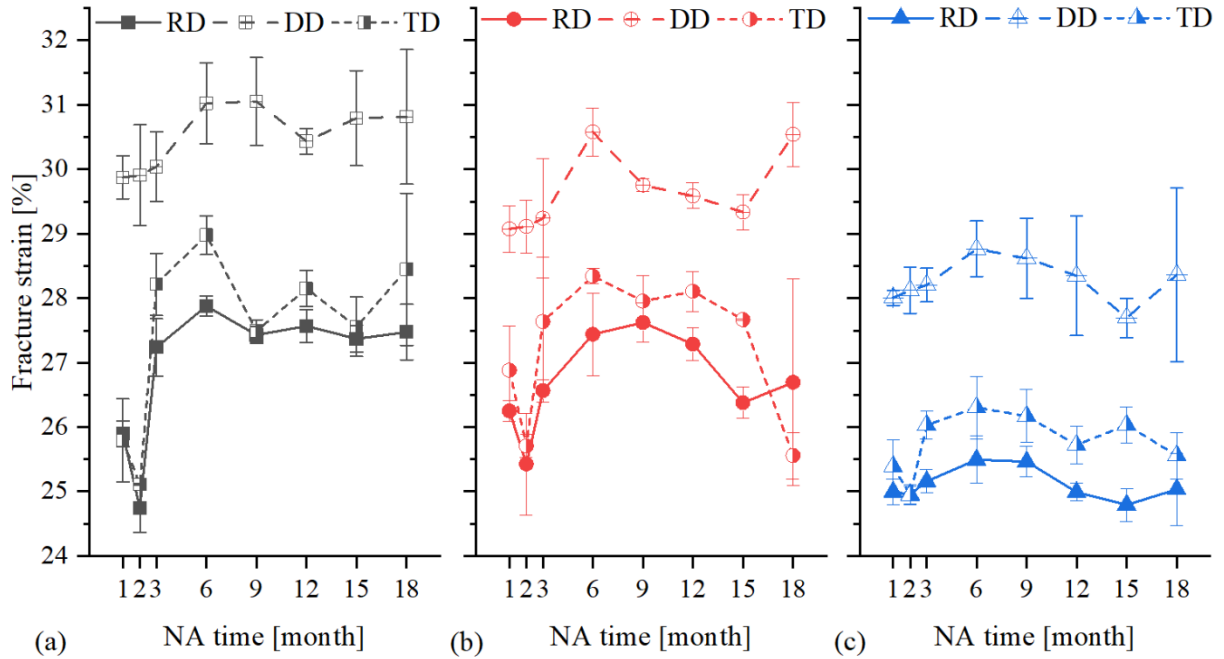


Figure 40 Influence of NA on fracture strain of (a) AF1, (b) AF2 and (c) AF3 blanks

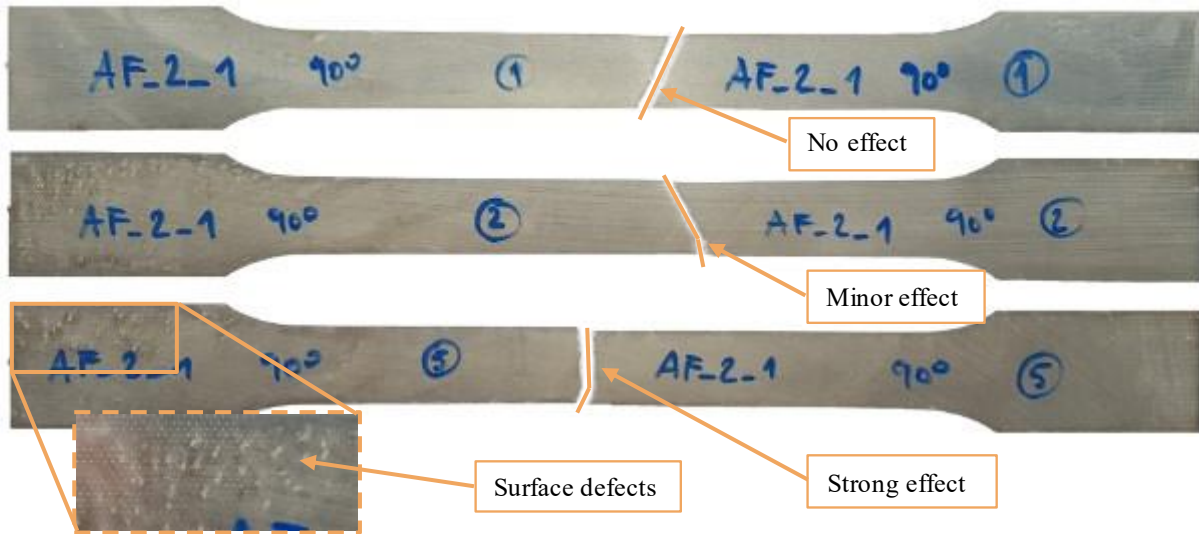


Figure 41 Effect of surface defects observed at tensile test samples after the wire eroding on the fracture pattern

To summarize, investigated Al-Mg-Si blanks showed the highest tensile ductility in DD, followed by TD and RD. The difference in strength of blanks, achieved by variation of Mg and Si content, had a direct impact on the tensile ductility so blanks with higher strength had a lower tensile ductility. However, a deterioration of tensile ductility was not observed within 1-18 months of NA despite a constant increase in material strength.

Post-uniform strains are calculated as the difference between the fracture strain and the uniform strain. Figure 42 (a), (b), and (c) show the influence of NA on the post-uniform strains of blanks AF1-AF3 in RD, DD, and TD, respectively. Generally, the highest post-uniform strains in each of the three directions were observed for blanks AF2, whereas blanks AF1 and AF3 obtained similar values. Post-uniform strains notably increased within 1-3 months of NA eventually staying in the range of about 4.5-6% within 6-18 months. Reduced post-uniform strain observed within 1-3 months of NA was mainly due to sample preparation as mentioned above. However, within 6 – 18 months, post-uniform strain remained relatively constant.

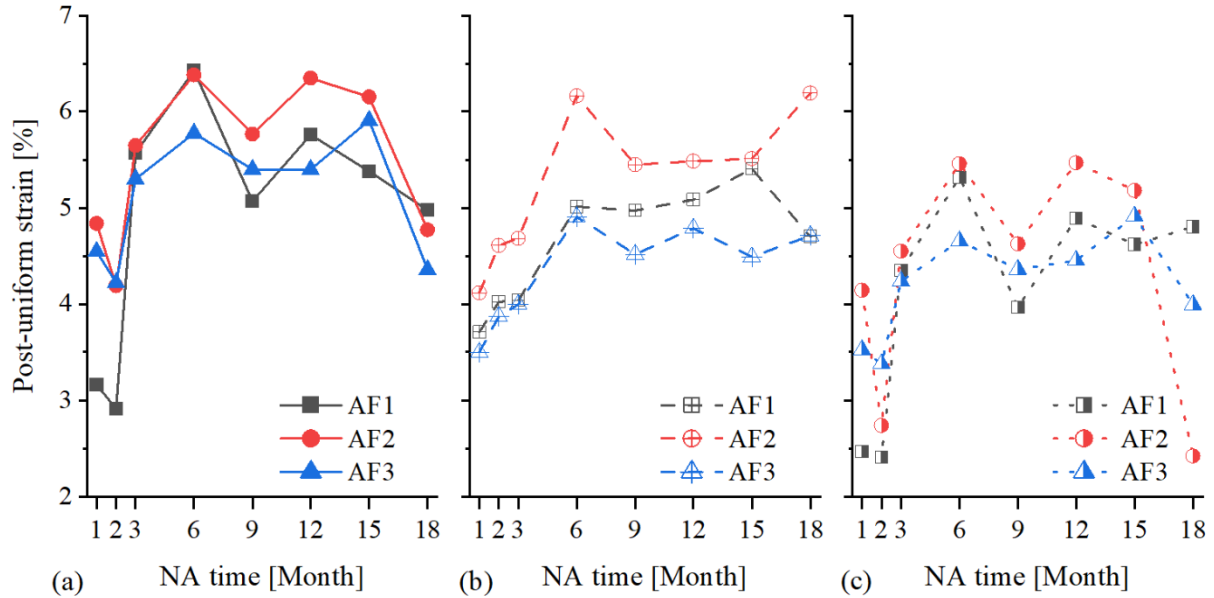


Figure 42 Post-uniform strain of AF1-AF3 blanks measured in (a) RD, (b) DD and (c) TD

### 5.1.3 Strain hardening

Figure 43 shows the progression of the  $n$ -value depending on the true plastic strain during the tensile test. The data was obtained after 18 months of NA with the tensile test samples in RD for the period of uniform elongation prior to necking. The highest strain hardening capacity was observed for blanks AF1, followed by blanks AF2 and AF3. A lower strain hardening capacity was observed for blanks with higher strength. Increasing the contents of Mg and Si for blanks AF2 promoted the material strength but negatively affected the strain hardening. The same was also observed for blank AF3 with higher Mg content and lower Si content. However, the strain hardening exponent of Al-Mg-Si alloys was variable during plastic straining. The minimum  $n$ -value of about 0.04 was observed at the start of plastic straining for each of the blanks. Subsequently, the  $n$ -value progressively increased and reached a maximum at the true plastic strain of about 0.06, i.e., about 0.300, 0.285, and 0.270 for blanks AF1, AF2, and AF3, respectively. The  $n$ -value almost linearly decreased for the true plastic strains greater than 0.06. This behavior of Al-Mg-Si alloy blanks during the plastic deformation reveals good distributions of stresses at low plastic strains but the tendency to localized necking and cracking at high plastic

strains. Moreover, it is necessary to specify the value or the range of strains for evaluating the  $n$ -values.

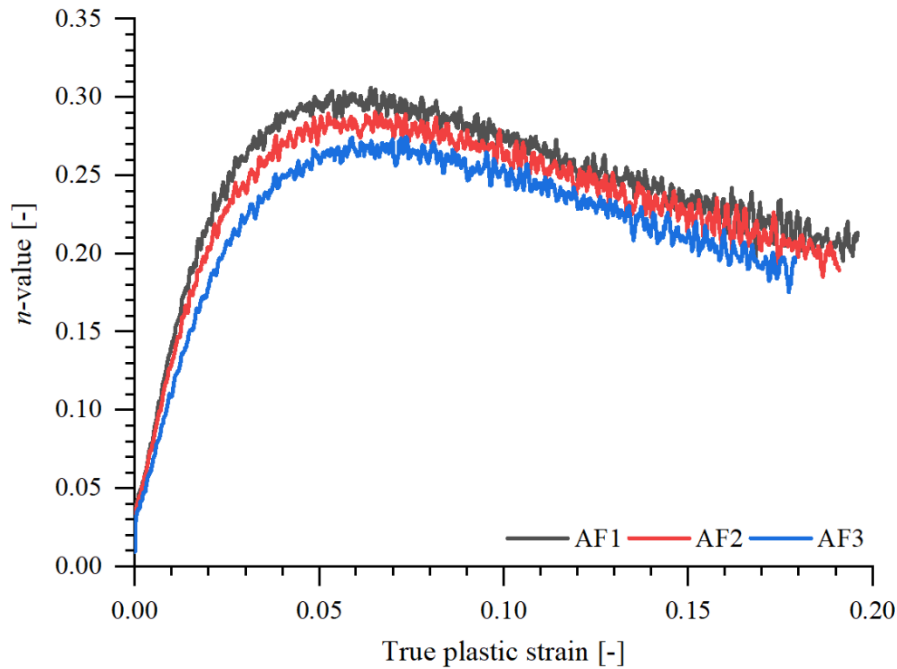


Figure 43 Strain hardening capacity during the tensile test of blanks AF1-AF3

The influence of NA on  $n$ -values determined for the strain range of 2-20% is shown in Figure 44. The highest  $n$ -values were observed for the tensile test samples in TD, whereas  $n$ -values in RD and DD were comparatively similar. After 1 month of NA,  $n$ -values for each of three directions were 0.293-0.295 for blanks AF1, 0.282-0.285 for blanks AF2, and 0.267-0.272 for blanks AF3. The strengthening of blank materials during NA negatively affected  $n$ -values, which constantly decreased. This correlates with the general trend observed in Figure 43 so higher strength leads to lower  $n$ -values. The decrease of  $n$ -values was more notable in the first months of NA. This agrees well with the strengthening of the blanks, which was also more notable at the beginning of NA. Moreover,  $n$ -values decreased by about 5.1%, 5.8%, and 8% for blanks AF1, AF2 and AF3, respectively. Thus, the decrease of  $n$ -values due to NA is related to natural aging kinetics, so the decrease of  $n$ -values was more intensive for blanks with faster NA kinetics. Decreasing  $n$ -values during NA of Al-Mg-Si alloys was also reported by other researchers in the early hours of NA [53] but also in later stages of NA [33,39,55]. Since  $n$ -values are related to formability, the decreasing  $n$ -values may be an indicator of formability deterioration.

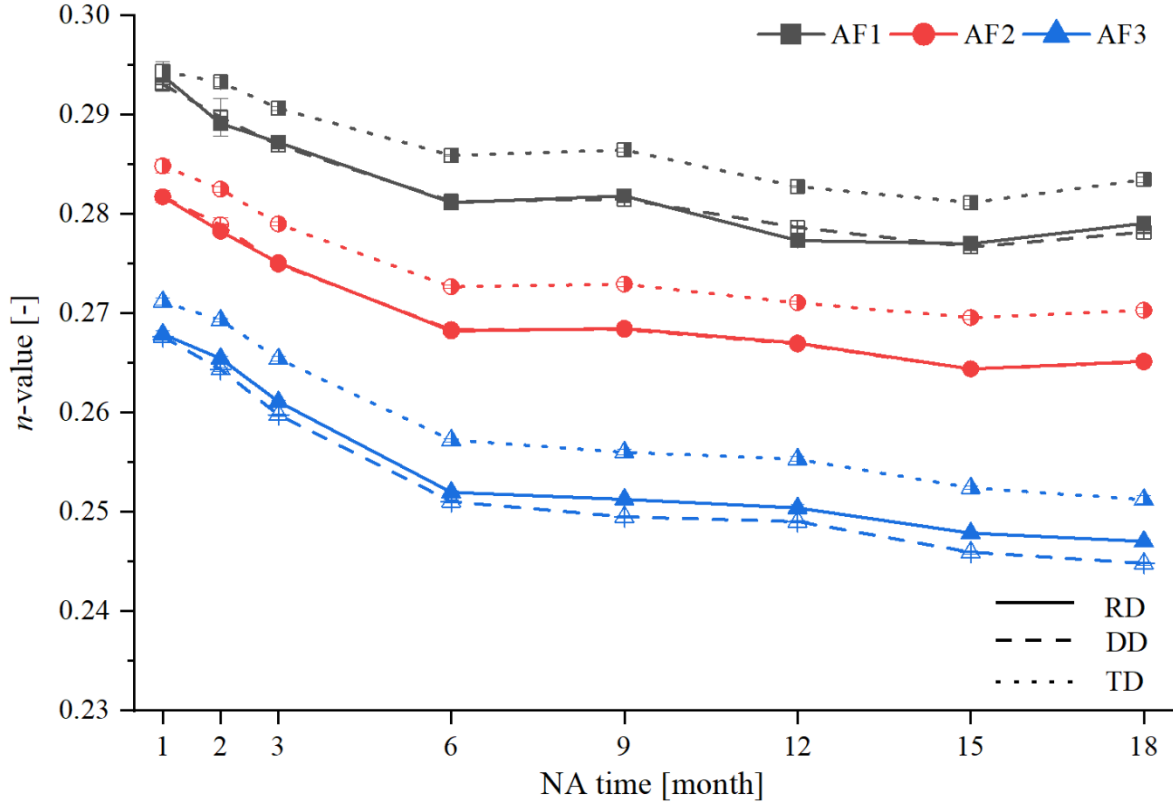


Figure 44 Influence of NA on  $n$ -values of blanks AF1-AF3 in RD, DD and TD

#### 5.1.4 Anisotropy

Normal anisotropy ( $r$ -value) was determined for strain range of 2-20% in RD, DD and TD. Influence of NA on  $r$ -values of blanks AF1-AF3 is shown in Figure 45. After 1 month of NA, normal anisotropy in RD,  $r_0$ , was 0.749, 0.713 and 0.788 for blanks AF1, AF2 and AF3, respectively. Thus, blanks AF3 had the highest  $r_0$ , followed by AF1 and AF3 blanks. A similar scenario was observed in TD with  $r_{90}$  of 0.683 for blanks AF1 and AF3, and of 0.625 for blanks AF2. However, a different scenario was observed for normal anisotropy in DD,  $r_{45}$ . The highest  $r_{45}$  of 0.476 was observed for blanks AF2 whereas  $r_{45}$  was 0.426 for blanks AF1 and 0.375 for blanks AF3. Yet, the strengthening of blank materials due to clustering of Mg and Si atoms did not affect the normal anisotropy since  $r$ -values remained constant within 1-18 months of NA. The  $r$ -values of Al-Mg-Si alloys are mostly determined by the crystallographic texture [108], which was not affected by the clustering effect. Relatively constant  $r_0$ ,  $r_{45}$  and  $r_{90}$  in range of 0.58-0.67 are reported also by Simões et al. [48] for AA6016 within 1-7 months of NA. Contrary, Gu et al. [33] observed a significant decrease of  $r_0$ ,  $r_{45}$  and  $r_{90}$  for AA6014. Within 1-6 months of NA,  $r_0$ , and  $r_{90}$  decreased by about 0.2 whereas  $r_{45}$  decreased by about 0.1.

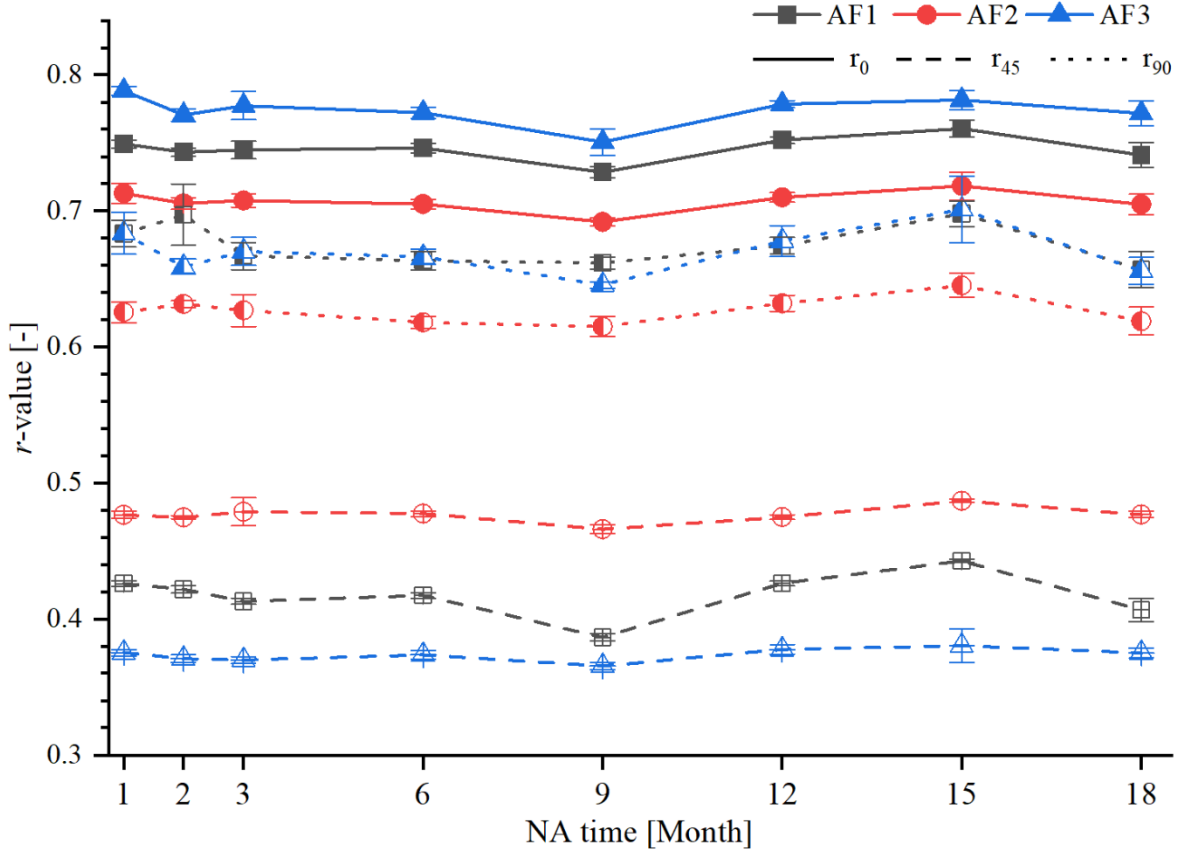


Figure 45 Influence of NA on  $r$ -values of blanks AF1-AF3

The influence of NA on the planar anisotropy  $\Delta r$  of blanks AF1-AF3 is shown in Figure 46. After 1 month of NA, the lowest planar anisotropy  $\Delta r$  of about 0.2 was observed for blanks AF2. This was due to the lowest  $r_0$  and  $r_{90}$  and the highest  $r_{45}$  for AF2 blanks compared to blanks AF1 and AF3. The planar anisotropy  $\Delta r$  was about 0.3 for blanks AF1 and 0.34 for blanks AF3. Within 1-18 months of NA the planar anisotropy  $\Delta r$  of blanks AF1-AF3 remained constant, since the  $r$ -values in RD, DD and TD were also not influenced by NA. Relatively constant  $\Delta r$  in the range of about 0.03 were reported by Simões et al. [48] for AA6016 within 1-7 months of NA. Contrary, Gu et al. [33] observed a significant decrease for  $\Delta r$  of about 0.1 for AA6014 within 1-6 months of NA.

An average normal anisotropy,  $r_m$ , was relatively similar for each of blanks AF1-AF3. Based on  $r_m$  values, a significant difference between the blanks could not be distinguished. After 1 month of NA,  $r_m$  of about 0.57 was observed for the blanks AF1 and AF2. A minorly lower  $r_m$  of about 0.56 was observed for blanks AF3 after the same period of NA. Only slight fluctuations of  $r_m$  were observed within 1-18 months of NA so it can be concluded that average normal anisotropy also remained constant. This is not surprising since normal anisotropy of blanks AF1-AF3 also remained unchanged during NA.

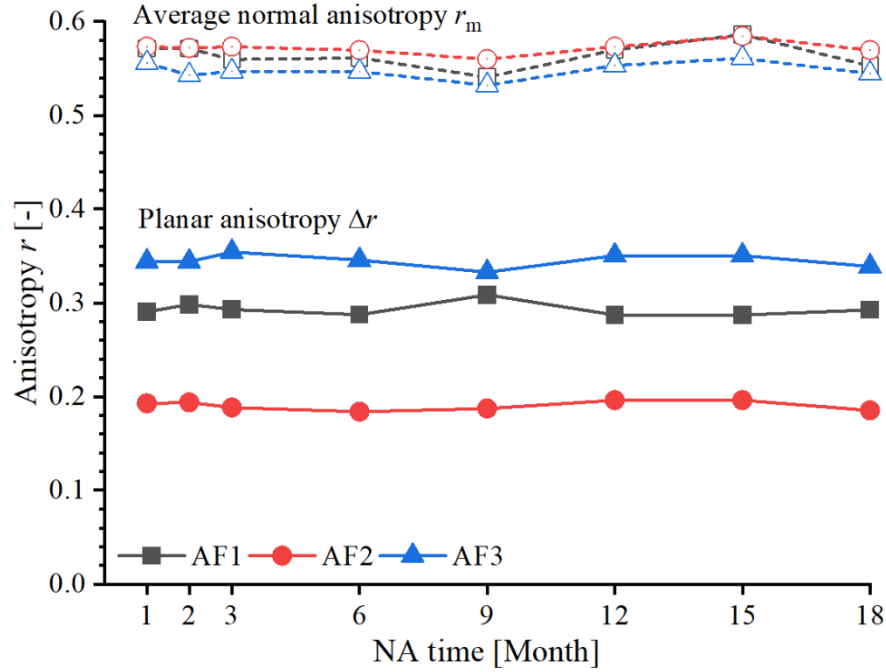


Figure 46 Influence of NA on the average normal anisotropy  $r_m$  and the planar anisotropy  $\Delta r$  of blanks AF1-AF3

### 5.1.5 Discussion mechanical parameters

Blanks were stored at the ambient temperature during the NA. The difference in air temperature between hot summer days and cold winter days was  $> 20^\circ\text{C}$ . Such difference likely affected the NA kinetics so slight fluctuations of the yield strength were detected. Moreover, fluctuations of the fracture strain were also observed. These fluctuations were notably higher than for the uniform strain, and they were mainly induced by the sample preparation. However, the amplitude of fluctuations for the fracture strain was still significantly lower than commonly observed in the literature. This indicates that the sample preparation and other factors that may affect the value of fracture strain were not considered. The chemical composition had an enormous effect on each of the mechanical parameters. Increasing the Si and Mg content promoted the initial strength of Al-Mg-Si alloy blanks but decreased the initial ductility and initial strain hardening capacity ( $n$ -value). Surprisingly, further increase of material strength due to NA did not affect the tensile ductility but the decrease of  $n$ -values continued. Whereas the literature reports clearly proved a negative effect of NA on  $n$ -values, the research works reported a negative, positive as well minor effect of NA on the tensile ductility. However, the yield strength increase of blanks AF1-AF3 was significant (about 20%) within 1-18 months of NA, and if a negative effect of NA on tensile ductility is there, it should be clearly visible. Thus, it can be concluded that the effect of NA on tensile ductility is minor. Moreover, the production process of blanks AF1-AF3 was completely identical, and the only difference between the blanks was in chemical composition. The microstructural analysis was not included in this work, but based on  $r$ -values can be concluded that the crystallographic texture was affected by variable chemical composition. In general, the determined  $r$ -values were lower than 1, which is common for Al-Mg-Si alloys. This

indicates more intensive material flow from the thickness than from the width during plastic straining. Material flow from the thickness leads to the thinning of material and earlier cracking, which is not beneficial for formability. Thus, the general tendency is to provide the highest possible  $r$ -values. Yet, it must be balanced between  $r$ -values in RD, DD and TD. An increase of  $r$ -values in RD does not necessarily lead to better formability if  $r$ -values in DD and TD are decreased. Thus,  $r$ -values must be analyzed in the form of planar anisotropy  $\Delta r$  and average vertical anisotropy  $r_m$ . However, the strengthening of Al-Mg-Si blanks had only a minor effect on  $r$ -values. Thus, it can be concluded that the changes in the crystallographic texture were minor during the NA.

## 5.2 Generation of flow curves using stack compression test

Figure 47 shows the flow curves obtained after 6 months of NA using three different testing methods for blanks (a) AF1, (b) AF2, and (c) AF3. The maximum true plastic strain reachable in the tensile test in RD was about 0.20 whereas higher true plastic strains of 0.35 and 0.60 were reached in the stack compression test and the bulge test, respectively. The bulging of stacked samples already started for true plastic strains greater than 0.35 so the acquired data for strains greater than 0.35 was not valid anymore. The main difference between the obtained flow curves is the applied load, which was different for each of the tests. Uniaxial tension was applied in the tensile test, biaxial compression in the stack compression test, and biaxial tension in the bulge test. This can lead to a slight difference in strength between the flow curves but the strengthening tendency at higher plastic strains should remain the same for each of the curves [16]. Therefore, the flow curve from the tensile test is used as a basis for generating the flow curves and other tests are only used for the data extrapolation. There are two basic possibilities for generating the flow curves. The first one is simply extending the flow curves obtained by the tensile test with data from other tests. The second option is to find a specific model (equation) that can accurately describe strengthening behavior at low as well as at high true plastic strains.

For true plastic strains lower than 0.2, a very good agreement was observed between the flow curves obtained using the uniaxial test (the tensile test) and biaxial tests (the stack compression test and the bulge test) despite the difference in the type of load. The stack compression test and the bulge tests also provided identical strengthening trends for true plastic strains greater than 0.2. Compared to the tensile test and stack compression test, the flow curve from the bulge test fluctuated more and showed a slightly higher yield strength. However, the fluctuations reduced at higher true plastic strains, and a clear trend was observable. The tensile test and the stack compression test provided very smooth curves. The Hockett-Sherby model [60], as described by Equation (13), is frequently used for describing the flow curves of Al-Mg-Si blanks [101,109,110]. This model provided acceptable results for the plastic strains  $< 0.2$  but underestimated the true stresses for the true plastic strains  $> 0.2$ . An improvement was achieved by using combined models that will increase the accuracy at higher true plastic strains. Combined Swift model (Equation (14)) [61] and Hockett-Sherby model were used to improve the characterization of the strengthening behavior for blanks AF1-AF3 at higher plastic strains. The combined model was described using Equation (15) with the constant  $\gamma = 0.3$ . The parameters  $\sigma_{ini}$ ,  $\sigma_{sat}$ ,  $a$  and  $p$  used in Equation (13) and  $C$ ,  $\varepsilon_0$ ,  $m$  used in Equation (14) are shown in Table 11. Based on the presented results, a conclusion can be drawn that extrapolating the flow curves based only on the data from tensile test might be misleading.

Table 11 Parameters used for describing the flow curves of blanks AF1-AF3 determined after 6 months of NA

Blank	Hockett-Sherby					Swift	
	$\sigma_{ini}$	$\sigma_{sat}$	$a$	$p$	$C$	$\varepsilon_0$	$m$
AF1	109.6	302.6	8.95	0.930	456.7	0.010	0.310
AF2	128.9	339	8.55	0.931	502.3	0.010	0.293
AF3	151	354	9.25	0.955	515	0.011	0.300

$$\sigma_{\text{Hockett-Sherby}} = \sigma_{\text{sat}} - (\sigma_{\text{sat}} - \sigma_{\text{ini}}) \exp(-a \varepsilon_{\text{pl}}^p) \quad (13)$$

$$\sigma_{\text{Swift}} = C(\varepsilon_0 + \varepsilon_{\text{pl}})^m \quad (14)$$

$$\sigma_{\text{flow}} = \gamma \sigma_{\text{Hockett-Sherby}} + (1 - \gamma) \sigma_{\text{Swift}} \quad (15)$$

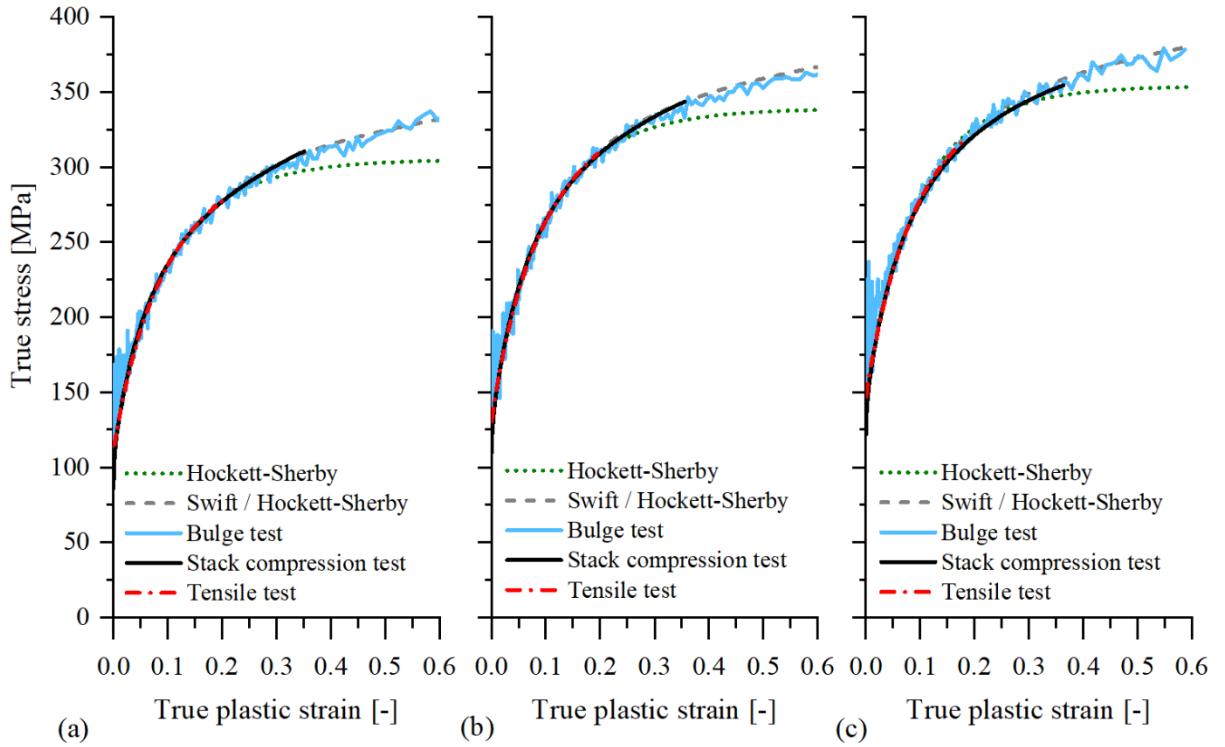


Figure 47 Strengthening as function of the true plastic strain (flow curve) for blanks (a) AF1, (b) AF2 and (c) AF3

### 5.3 Influence of NA on the flow curves of Al-Mg-Si blanks

Using up-to-date data is crucial for achieving accurate results in numerical forming simulations. Therefore, it is necessary to implement the changes in mechanical properties of Al-Mg-Si blanks that occurred during NA in material models for numerical forming simulations. The NA had a notable influence on the strength of blanks AF1-AF3 whereas the other parameters relevant to the numerical forming simulations remained almost unchanged (e.g.,  $r$ -values). The increase of strength and the decrease of  $n$ -values directly affected the flow curves. Therefore, the flow curves

were created for blanks AF1-AF3 with 1-18 months of NA. Utilization of accurate flow curves in material models is of utmost importance for reaching a sufficient level of accuracy in numerical forming simulations.

Figure 48 shows the flow curves determined for blanks AF1-AF3 within 1-18 months of NA. The flow curves constantly increased during the NA due to the clustering of Mg and Si atoms. The slope of the flow curves was different for each of the blanks since there was a difference in strain hardening capacity. The differences between the curves at lower true plastic strains were not the same as the differences at high true plastic strains. Some curves were equal at low true plastic strains but differed at high true plastic strains due to differences in strain hardening. Yet, some general observations can still be drawn. The flow curve of blanks AF1 determined after 18 months of NA was only minorly lower than the flow curve of blanks AF2 determined after 1 month of NA. However, the flow curve of blanks AF2 determined after 3 months of NA exceeded the flow curve of blanks AF3 determined after 1 month of NA for true plastic strains  $> 0.15$ . Moreover, the flow curve of blanks AF2 determined after 18 months of NA reached the flow curve of blanks AF3 determined after 6 months of NA at the true plastic strain of about 0.9. Hence, the influence of NA on the flow curves of blanks AF1-AF3 was significant and must be considered in numerical forming simulations. Even though Al-Mg-Si blanks are nowadays used only within 6 months of NA, the strengthening is particularly high for this period of NA. The actual forming time of blanks is frequently not fixed and may vary from 1 to 6 months. Thus, tool makers should consider this effect in tool design for predicting the potential formability changes of Al-Mg-Si blanks.

Table 12 Influence of NA on the constants used for generating the flow curves

NA time [Month]	AF1			AF2			AF3		
	$\sigma_i$ [MPa]	$\sigma_{sat}$ [MPa]	$C$ [MPa]	$\sigma_i$ [MPa]	$\sigma_{sat}$ [MPa]	$C$ [MPa]	$\sigma_i$ [MPa]	$\sigma_{sat}$ [MPa]	$C$ [MPa]
1	92	281	422	110	321	467	125	326	482
2	98	287	434	115	324	471	129	332	492
3	100	290	442	118	332	481	136	338	499
6	110	303	457	129	339	502	151	354	515
9	111	307	464	131	341	504	156	359	519
12	112	300	463	132	344	507	157	360	520
15	113	306	465	135	346	510	159	363	523
18	117	312	471	139	351	520	162	365	543

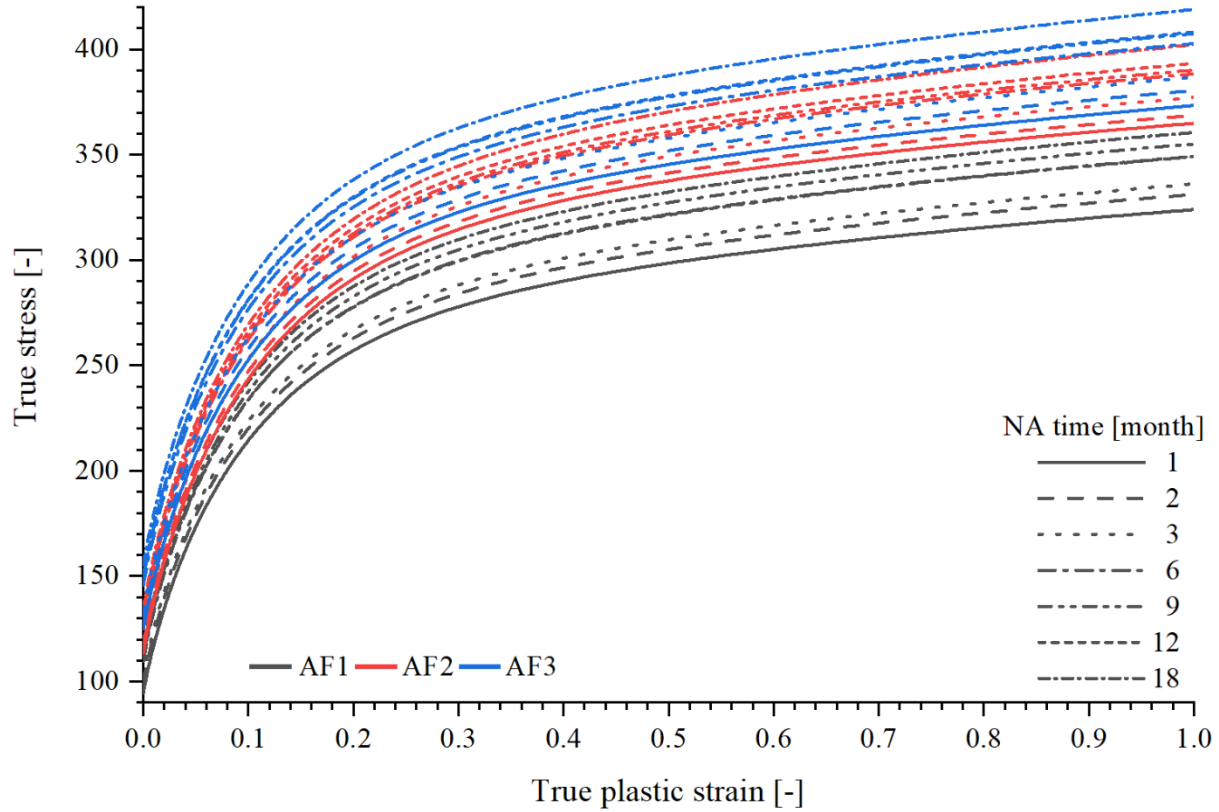


Figure 48 Influence of NA on the flow curves of blanks AF1-AF3

The flow curves were generated using Equations (13), (14) and (15). True stress – true plastic strain curves from the tensile test in RD were used as a basic for determination of the flow curves. The parameters  $\sigma_i$  and  $\sigma_{sat}$  from Equation (13) and the parameter  $C$  from Equation (14) constantly increased during the NA, which is due to the strengthening of the blanks. The evolution of these constants during NA is shown in Table 12. These parameters were not only affected by the strengthening but also by changes of  $n$ -values during NA. However, since the changes of strain hardening exponent were not significantly high, this was compensated by adapting the variable parameters  $\sigma_i$ ,  $\sigma_{sat}$  and  $C$ . Remaining parameters  $a$ ,  $p$ ,  $m$ ,  $\varepsilon_0$  shown in

Table 11 were constant for the entire period of NA. The weighting factor  $\gamma = 0.3$  remained the same for each of the flow curves.

#### 5.4 Tensile behavior of Al-Mg-Si blanks at elevated strain rates

Figure 49 shows engineering stress-strain curves for blanks AF1-AF3. The data was obtained by uniaxial tensile testing after 15 months of NA at a low strain rate of 0.001 1/s, moderate strain rate of 0.1 1/s and high strain rate of 1 1/s. Utilization of extensometer was not possible so straining of the tensile test samples was calculated based on the relative movement between the upper and the lower clamp. Therefore, information about the tensile ductility gained from these tests may not be quantitatively accurate but potential changes of the tensile ductility were still detectable. These tests were conducted using the INSTRON testing machine as described in

section 3.2. Engineering stress-strain curves obtained at the low strain rate agreed well with the stress-strain curves obtained at the quasi-static strain rate using the Zwick tensile testing machine. Blanks AF1-AF3 showed only minor strain rate dependency in terms of strengthening and tensile ductility. The same findings were reported in other research works for Al-Mg-Si alloys in T4 condition at room temperature [111–114]. A slight decrease in the tensile ductility was observed for blanks AF1-AF3. Likely the ductility loss between the low and the mediate strain rate was higher than between the mediate and the high strain rate. Loss of ductility at elevated strain rates was also reported by Monteiro [111] and by Li and Ghosh [112]. However, additional tensile tests with accurate measurements of sample straining would be required to confirm such material behavior. Moreover, engineering stresses were calculated using Equation (1) with  $F$  representing the tensile force measured by the load cell and  $A$  representing the initial sample cross section. The quantitative analysis of strengthening at elevated strain rates can be conducted independently of the straining measurement. The increase of the tensile force is proportional to the increase of material strength. However, due to the effect on adiabatic heating [115], which leads to the softening of material at higher strains, the strengthening of blanks at elevated strain rates was analyzed only at low engineering strains of 1%, 2%, and 3%.

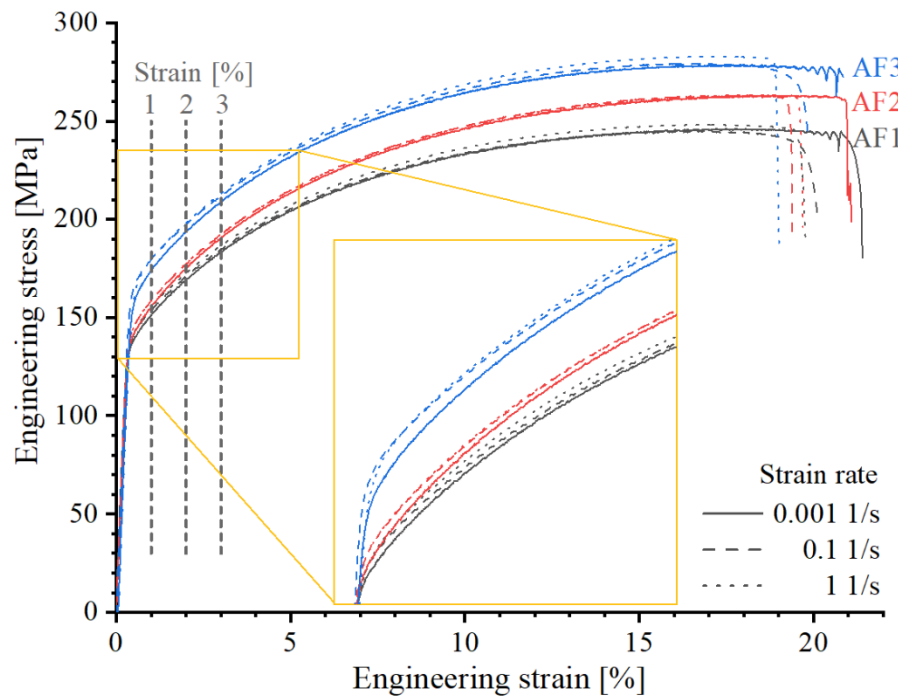


Figure 49 Effect of elevated strain rates on the strengthening of blanks AF1-AF3 obtained after 15 months of NA

Figure 50 shows the relative strengthening of blanks AF1-AF3 at the mediate and the high strain rate with respect to the low strain rate of 0.001 1/s. A strength increase of 3.7 MPa, 3.3 MPa, and 5.9 MPa was observed at the engineering strain of 1% and the mediate strain rate of 0.1 1/s

for blanks AF1, AF2, and AF3, respectively. Additional strength increase was observed for the high strain rate of 1 1/s, so blanks AF1, AF2, and AF3 had a strength increase of 4.5 MPa, 4.8 MPa, and 7.1 MPa at the engineering strain of 1%, respectively. However, the values of relative strengthening decreased at the engineering strains of 2% and 3%. This means that the effect of adiabatic heating has already started. Generally, elevated strain rates affected the strengthening of blanks AF1-AF3 only minorly, which is also reported elsewhere [113,114]. Contrary, Li and Ghosh reported a decrease in strength at elevated strain rates of 0.15 1/s and 1.5 1/s for AA6111-T4 [112]. Surprisingly, the research works about the strain rate dependency of Al-Mg-Si alloys in T4 condition at room temperature are very limited, likely due to the comparatively low influence of strain rate on the strengthening and the tensile ductility. The existing research works analyzed strain rates that are way below the strain rates occurring during the deep drawing on an industrial scale. But alloy blanks of this series are widely used in the automotive industry. Hence, an in-depth study about the influence of strain rates would be necessary for understanding the formability behavior of these alloy blanks in forming simulations as well as in experiments.

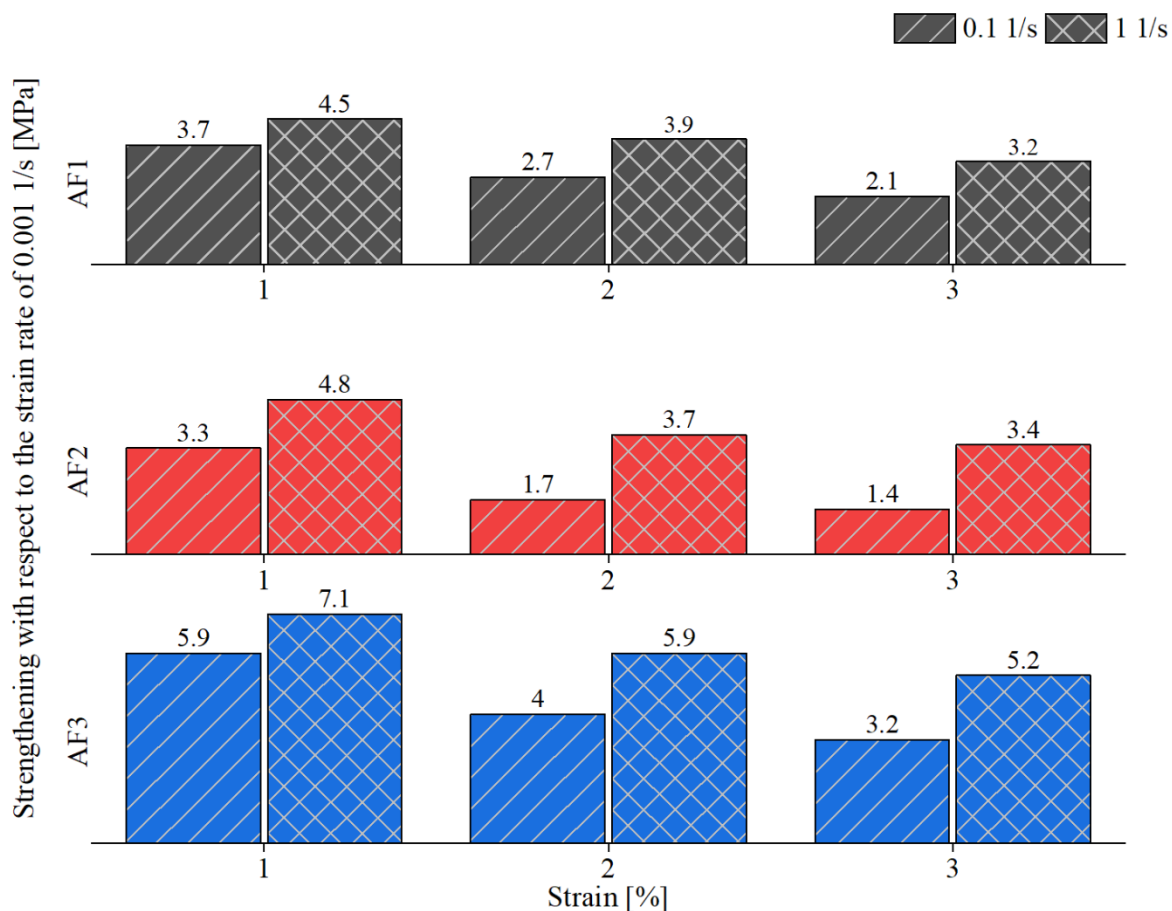


Figure 50 Strengthening of blanks AF1-AF3 at elevated strain rates with respect to the quasi-static strain rate of 0.001 1/s

The strength increase measured at the engineering strains of 2% and 3% was underestimated due to the adiabatic heating. Therefore, a strength increase measured at an engineering strain of 1% was taken for calculating the flow curves at elevated strain rates. The quasi-static flow curves determined after 15 months of NA are described in section 5.3. The measured relative strengthening at 1% of strain was added to the quasi-static flow curves for generating the flow curves at elevated strain rates. The resulting flow curves for blanks AF1-AF3 are shown in Figure 51.

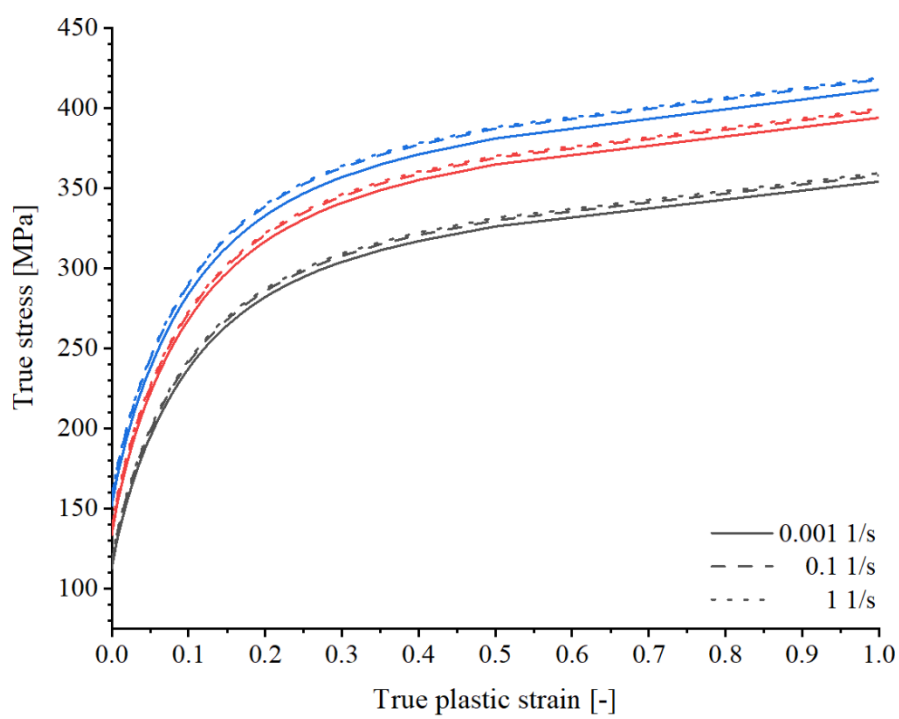


Figure 51 Effect of elevated strain rates on the flow curves of blank AF1-AF3

## 6 Formability of Al-Mg-Si alloy blanks

### 6.1 Influence of chemical composition, lubrication and natural aging on the formability

Figure 52 shows the influence of NA on the formability of blanks AF1-AF4 determined using the A-Tool for the forming velocity of (a) 10 mm/s and (b) 100 mm/s. After 1 month of NA, the maximum BHF for crack-free forming ( $F_{\max}$ ) at the low forming velocity of 10 mm/s were 360 kN, 520 kN, 540 kN and 600 kN for blanks AF1, AF2, AF3 and AF4, respectively. An increase of Si-content in blanks AF2 resulted in better formability than for blanks AF1. The positive effect of higher Si-content on the formability of Al-Mg-Si alloys was also reported elsewhere [116–119]. Although a decrease in the formability was expected for blanks AF3 due to lower Si-content, the formability was similar to the formability of blanks AF2. Likely the decrease of Si-content was somehow compensated by the increase of Mg-content, which also positively affected the formability of Al-Mg-Si blanks. This is contrary to some studies that reported a negative effect of higher Mg-content on the formability of Al-Mg-Si blanks [117,118]. However, the best formability was observed for blanks AF4, which had the same chemical composition as blanks AF1 but with different lubrication. The application of PL 39 SX lubricant instead of Drylube E 1 positively affected the tribological conditions in the contact area between the tool and blanks. This made the material flow easier as the  $F_{\max}$  almost doubled compared to blank AF1. The importance of tribology in deep drawing was also reported by Sabet et al. [101] and Domitner et al. [120]. Moreover, the formability of blanks AF1-AF4 expressed through critical BHF remained constant for the low forming velocity of 10 mm/s within 1-18 months of NA. The width of the transition zone was 40 kN for blanks AF1, 40-60 kN for blanks AF2 and AF3, and 60-80 kN for blanks AF4. Evidently, the width of the transition zone was dependent on the extent of the BHF so wider transition zones were observed at higher critical BHF.

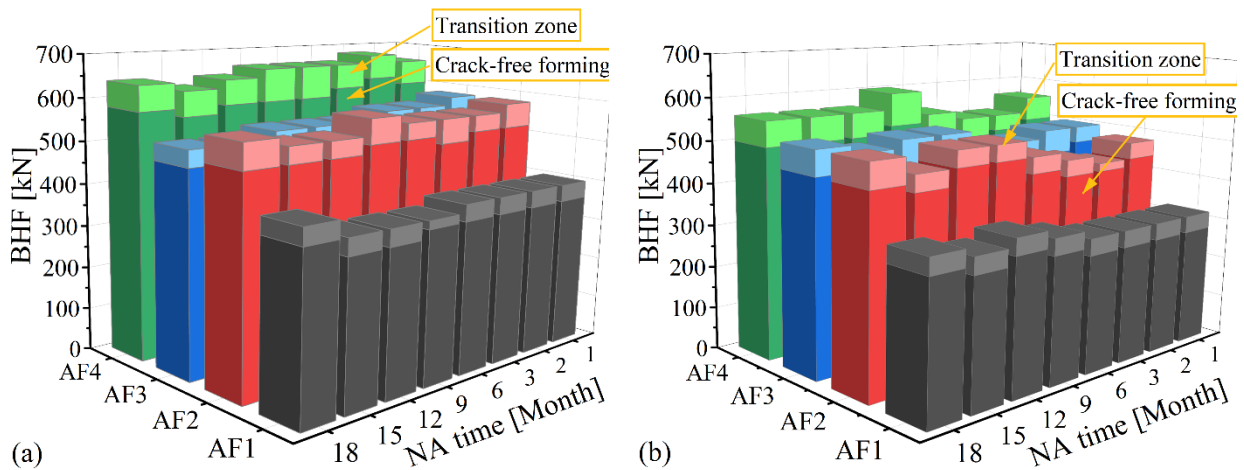


Figure 52 Influence of NA on the formability characterized by maximum blankholder force using the A-Tool and constant forming velocities of (a) 10 mm/s and (b) 100 mm/s

Like at the low forming velocity of 10 mm/s, blanks AF4 also showed the best formability at the high forming velocity of 100 mm/s followed by blanks AF3 and AF2 whereas blanks AF1 had the lowest formability. After 1 month of NA,  $F_{\max}$  determined at the high forming velocity were 280 kN, 440 kN, 460 kN and 500 kN for blanks AF1, AF2, AF3 and AF4, respectively. High forming velocity negatively affected the formability of blanks AF1-AF4, so  $F_{\max}$  decreased for 80-100 kN after increasing the forming velocity from 10 mm/s to 100 mm/s. The high forming velocity induced higher strain rates, which had a negative influence on some of the material properties. Although the strengthening of Al-Mg-Si alloys was not highly affected at the higher strain rates [113,114], it might lead to the decrease of the ductility [111,112]. Thus, the formability deterioration at high forming velocity is likely due to the loss of ductility. Moreover, higher strain rates may also affect the  $r$ -values of aluminum alloys [121–123], which play an important role for the formability. Moreover, formability did not decrease either at the high forming velocity of 100 mm/s within 1-18 months of NA. The critical BHF's even minorly increased after 18 months of NA for some of the investigated blanks. The width of the transition zone was 40 kN for blanks AF1, 40-60 kN for blanks AF2 and AF3 and 60-80 kN for blanks AF4.

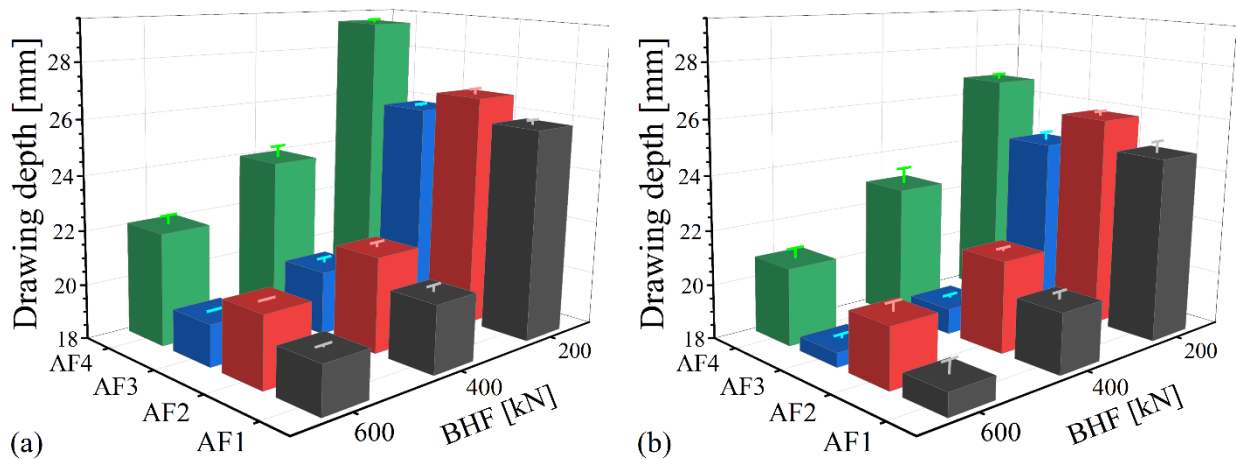


Figure 53 Influence of BHF on the maximum drawing depth determined using the CS-Tool after 1 month of NA for the forming velocities of (a) 10 mm/s and (b) 100 mm/s

Figure 53 shows the influence of BHF on the maximum drawing depth  $D_{\max}$  for the forming velocity of (a) 10 mm/s and (b) 100 mm/s. The deep drawing tests were conducted after 1 month of NA by using the CS-Tool. At the lowest BHF of 200 kN and the low forming velocity of 10 mm/s, average  $D_{\max}$  of 25.9 mm, 26.7 mm, 25.9 mm and 29.1 mm were measured for blanks AF1, AF2, AF3 and AF4, respectively. Thus, the highest  $D_{\max}$  and therefore the best formability was observed for blanks AF4 followed by blanks AF2. Blanks AF1 and AF3 showed comparatively similar formability. The determined formability agreed well with the results obtained by using the A-Tool except for blanks AF3, that showed slightly lower formability. Moreover,  $D_{\max}$  decreased at the same BHF of 200 kN after increasing the forming velocity to 100 mm/s due to strain rate dependency, which agrees well with the results observed by using the A-Tool. Average  $D_{\max}$  of 24.8 mm, 25.9 mm, 24.5 and 26.8 mm were observed at the BHF

of 200 kN and the forming velocity of 100 mm/s for blanks AF1, AF2, AF3 and AF4, respectively.

Further increase of the BHF to 400 kN led to average  $D_{\max}$  of 20.5 mm, 21.5 mm, 20.3 mm and 24.1 at the low forming velocity of 10 mm/s for blanks AF1, AF2, AF3 and AF4, respectively. Increasing the BHF from 200 kN to 400 kN reduced  $D_{\max}$  for each of the blanks but the order of blanks in terms of formability remained unchanged. Higher BHF increased the restraining forces in the flange area of the tool and hindered the flow of blank material into the tool cavity. Hindering the material flow promoted the material thinning and led to earlier cracking. Therefore,  $D_{\max}$  decreased by about 5–5.6 mm after increasing the BHF from 200 kN to 400 kN. Moreover,  $D_{\max}$  additionally decreased after increasing the forming velocity to 100 mm/s at the BHF of 400 kN due to strain rate effects to 20.2 mm, 21.3 mm, 18.9 and 22.9 mm for blanks AF1, AF2, AF3 and AF4, respectively.

At the BHF of 600 kN and the forming velocity of 10 mm/s average  $D_{\max}$  was 19.7 mm, 20.6 mm, 19.6 mm and 22.1 mm for blanks AF1, AF2, AF3 and AF4, respectively. Additional increase of BHF from 400 kN to 600 kN reduced  $D_{\max}$  only for about 0.7–2 mm, which is significantly lower compared to the  $D_{\max}$  reduction after increase of BHF from 200 kN to 400 kN. This effect is very similar to dependency of contact pressure on CoF, that changes radically at low contact pressure but only minorly at high contact pressures [63,101]. Hence, the formability deterioration expressed through  $D_{\max}$  was not linearly proportional with increasing BHF. Moreover, the lowest values for  $D_{\max}$  of 18.3 mm, 20.2 mm, 18.5 and 20.9 mm were observed at the BHF of 600 kN and the forming velocity of 100 mm/s for blanks AF1, AF2, AF3 and AF4, respectively. The negative effect of high forming velocity on  $D_{\max}$  was not dependent on BHF. Increase of forming velocity from 10 mm/s to 100 mm/s reduced  $D_{\max}$  for about  $1 \pm 0.5$  mm of blanks AF1–AF4 at each of three BHF.

Increasing both forming velocity and BHF reduces CoF in the flange area, but it also affects other material properties and the resulting formability. The sliding velocity between the blank and the tool is generally increased by increasing the forming velocities which usually leads to lower CoF. However, if the material properties are strongly dependent on strain rate, this will lead to a decrease in formability at higher forming velocities. However, if the material is not dependent on strain rate, increasing the forming velocity would eventually lead to enhancement of the formability at higher forming velocities. Yet, if the BHF is increased, the contact pressures in the flange area of the tool are increased and the resulting CoF is lower. However, the resulting restraining forces are still higher, so the material flow is generally more limited at higher BHF. Hence, it can be concluded that BHF had more effect on the formability of investigated Al-Mg-Si alloys than the forming velocity. In general, the effect of BHF on the formability is always negative and the influence of forming velocity can be either positive or negative, depending on the dependency of blank material on strain rate.

The influence of NA on  $D_{\max}$  determined using the CS-Tool was analyzed in detail. Figure 54 shows  $D_{\max}$  changes over NA with respect to the values observed after 1 month of NA at the same forming conditions for forming velocities of (a) 10 mm/s and (b) 100 mm/s. The upper, the middle and the lower row represent the changes of  $D_{\max}$  obtained at the BHF of 200 kN, 400 kN and 600 kN, respectively. The fluctuations of  $D_{\max}$  were mainly induced by variable ambient

conditions such as temperature and humidity. The fluctuations of  $D_{\max}$  during the NA observed using the CS-Tool were evidently higher than the fluctuation of critical BHF observed using the A-Tool. This was due to the higher measurement sensitivity of  $D_{\max}$ . Namely, the critical BHF were determined with 20 kN steps which was more robust than determination of  $D_{\max}$  for every 0.1 mm. Hence, even small changes of forming conditions were detectable with the CS-Tool whereas the A-Tool can detect only relatively higher changes of the formability. Hodžić et al. [99] reported that the formability of Al-Mg-Si alloy blanks can be affected by small changes of the contact temperature. Forming tryouts were conducted in ambient conditions similar to the industrial application. The recorded initial blank temperature prior to forming was in the range 19-29 °C. The deep drawing tests were conducted within 1.5 years of time including summer times and winter times. Considering this, a difference in air moisture likely affected the performance of lubricants. An additional cause for fluctuations of  $D_{\max}$  is sensitivity of the accelerometer. The accelerator was placed at the tool surface and not directly at relatively soft aluminum blanks. Cracking vibrations were transmitted through the tool parts, which might be a cause for delayed detection of cracking. Moreover, the fluctuations of  $D_{\max}$  observed at the high forming velocity of 100 mm/s were higher than the fluctuations observed at the low forming velocity of 10 mm/s. This was caused by dynamic effects during the forming at the high velocity using the hydraulic press. The faster dynamic of the press introduced additional vibrations, which were captured by the accelerometer. Force maxima as indicator of cracking initiation was additionally used to improve and control the accuracy of crack detection. The changes of  $D_{\max}$  observed at the low forming velocity of 10 mm/s were typically within  $\pm 0.5$  mm for each of the BHF. The changes of  $D_{\max}$  at the high forming velocity of 100 mm/s reached maximum of about -1.5 mm after 9 months of NA at the BHF of 200 kN. But after 18 months of NA  $D_{\max}$  values were only minorly lower than after 1 month of NA. Slight decreasing trends of  $D_{\max}$  were observed at the forming velocity of 100 mm/s for some cases. For instance,  $D_{\max}$  decreased by about 1 mm after 18 months of NA for blanks AF1 and AF3 at the BHF of 400 kN and for blanks AF2 and AF3 at the BHF of 600 kN. However, the same trend was not observed at the other forming conditions so a significant deterioration of formability can be neglected. Thus, it can be concluded that slight decreasing trends in specific cases were only coincidence. Deterioration of the formability was also not observed using the other deep drawing tool, i.e., the A-Tool. Moreover, deterioration of lubricant properties within 1-18 months of NA can also be excluded. However, the results of this investigation clearly prove that it is recommended to conduct comprehensive studies on formability using various sets of parameters. This would be helpful for better understanding of the formability and the effect of NA on the formability. Conducting the formability investigation only using one specific set of parameters may be misleading.

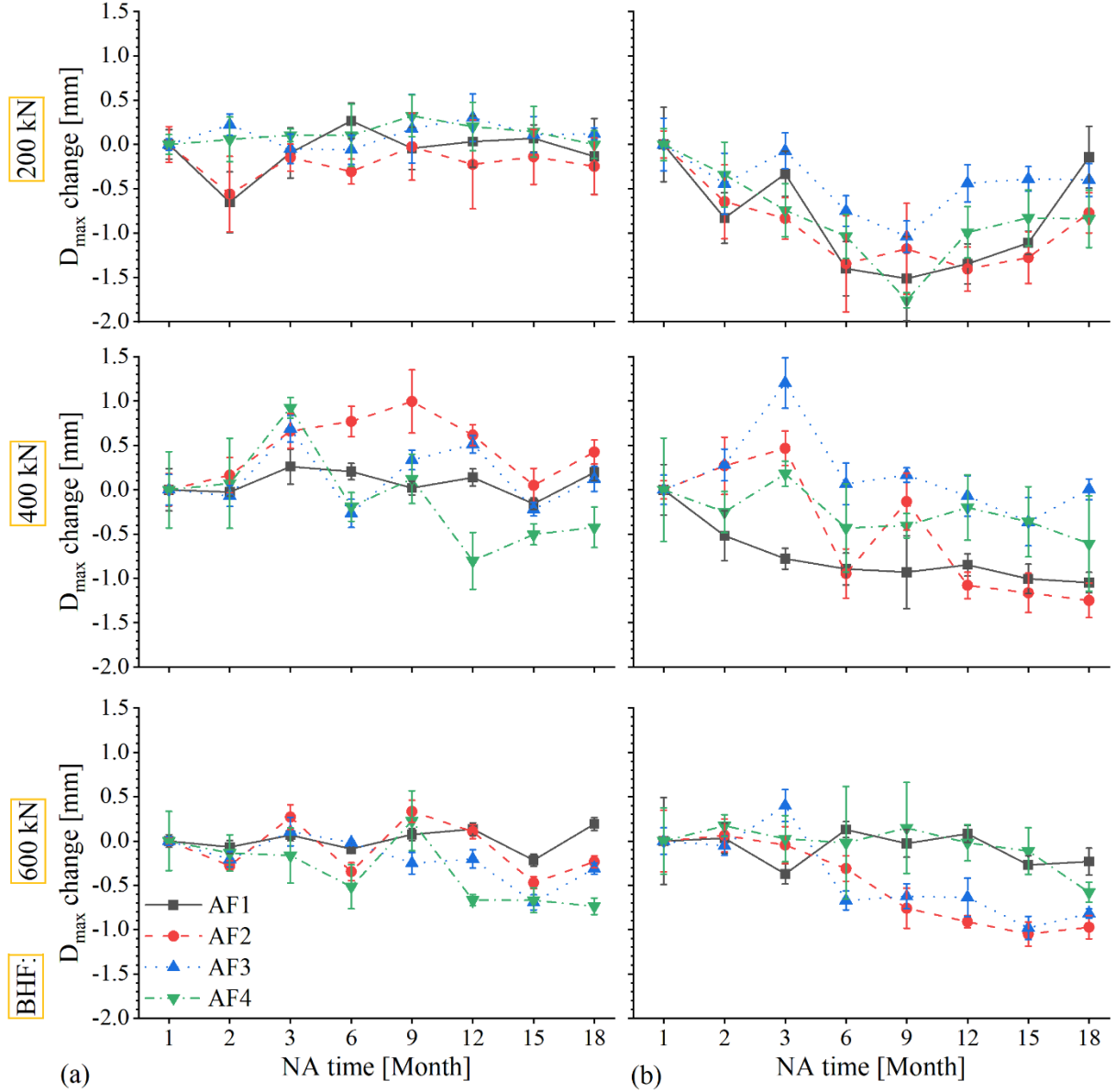


Figure 54 Change of maximum drawing depth  $D_{\max}$  during NA with respect to the maximum drawing depth determined after 1 month of NA for the forming velocities of (a) 10 mm/s and (b) 100 mm/s

### 6.1.1 Influence of the blank alignment, surface roughness and lubricant amount on the formability

The formability of blanks AF3 was similar to the formability of blanks AF2 when formed using the A-Tool. Yet, the formability of blanks AF3 was similar to the formability of blanks AF1 when formed using the CS-Tool. Hence, additional study was conducted about the factors that potentially influence the formability of Al-Mg-Si blanks. The analyzed factors include blank alignment, surface roughness and lubricant amount.

It was visually observed during the forming tryouts, that blanks AF3 slightly changed its initial, plane form after being placed onto the blankholder of the A-Tool. Namely, the initial form of blank AF3 prior to forming was not perfectly planned since some blank corners were not in direct contact with the blankholder surface, as shown in Figure 55. Moreover, the initial form of blanks AF1, AF2, and AF4 also appeared similarly after turning the blanks upside-down before placing them onto the blankholder surface. This effect was not observed for the CS-Tool due to the different shapes of the blankholder and smaller blanks.

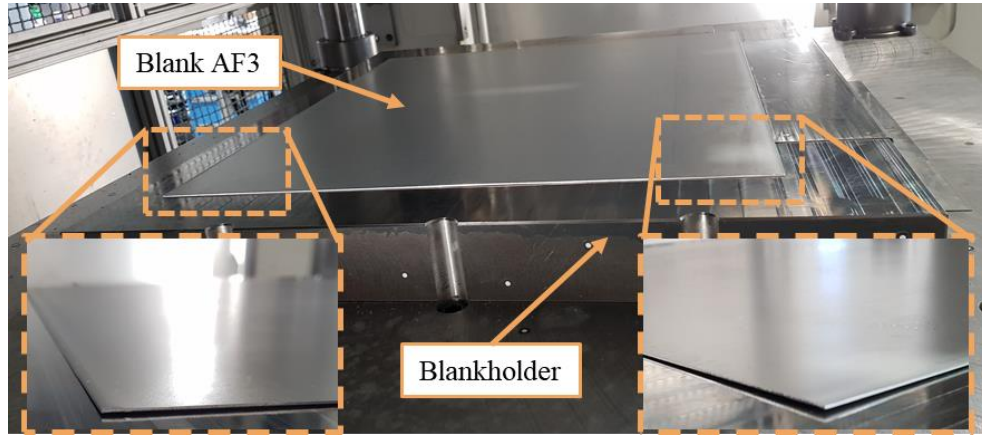


Figure 55 The form of convex curved AF3 blank after positioning at the blankholder

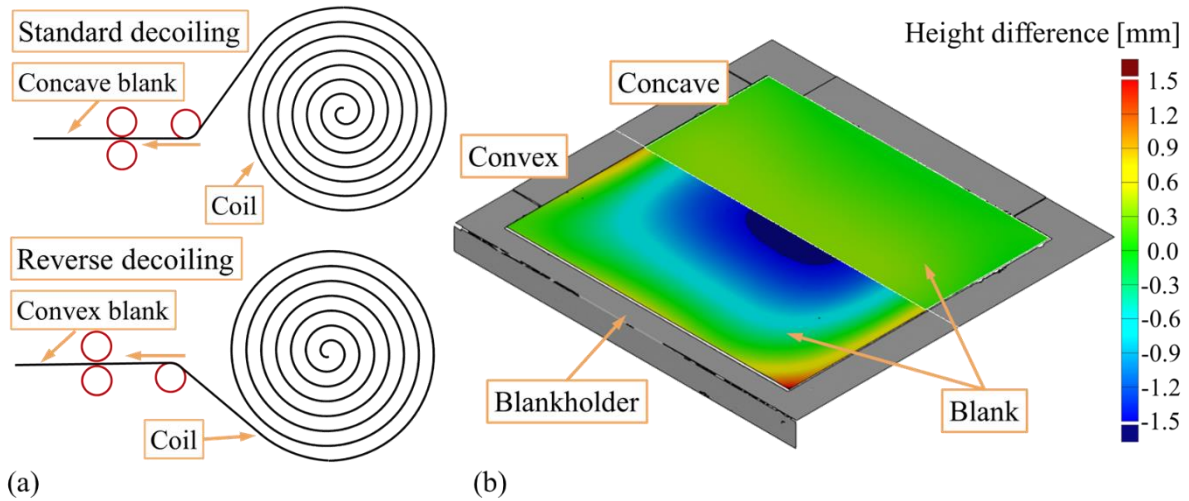


Figure 56 (a) Schematic illustration of standard and reverse decoiling and (b) effect of blank alignment on the initial form of the blank

Namely, the blanks were slightly curved perpendicular to RD as a result of coiling process. Although blanks went through the leveling unit after decoiling and before cutting to length a slight curvature remained present. Two different decoiling procedures are schematically illustrated in Figure 56 (a). The standard decoiling procedure provided minorly concave curved blanks and the reverse decoiling procedure provided minorly convex curved blanks. Note that convex curved blanks in as-received condition become concave after being turned upside-down.

The initial form of convex and concave curved blanks after placing onto the blankholder of the A-Tool was scanned using 3D optical scanning system ATOS. Figure 56 (b) shows height difference of curved blanks after placing onto the blankholder with respect to the perfectly plane blank. The form of the convex curved blank changed significantly, so the blank was about -1.5 mm lower in the central area and about 1.5 mm higher in the corner area than the plane blank. However, this effect was not observed for concave curved blanks. This was due to the effect of gravity, so the form of the relatively thin, concave curved blank became plane blank. Therefore, only forming tryouts conducted with concave curved blanks provided valid information about the formability of investigated Al-Mg-Si alloy blanks.

Since the blank alignment affected the initial form of blank, surface roughness and lubricant amount at upper and lower side of blanks was also analyzed. It is well known that surface roughness and lubricant amount at upper and lower side of blank may differ. In such cases, the tribological system is directly affected, and the formability results may also be affected. Figure 57 shows (a) an average surface roughness  $R_a$  and (b) a lubricant amount for blanks AF1-AF4. The upper side of blanks in as-received condition was designated as side A and the lower side as side B. Blanks AF1, AF2 and AF4 had a surface roughness  $R_a$  of  $0.86 \pm 0.1 \mu\text{m}$  on the side A and of  $0.66 \pm 0.1 \mu\text{m}$  on the side B. Contrary, blanks AF3 have a higher surface roughness  $R_a$  of  $0.86 \mu\text{m}$  on the side B and a lower surface roughness  $R_a$  of about  $0.70 \mu\text{m}$  on the side A. Similar scenario was observed for the lubricant amount, which was generally slightly lower than the target value of  $0.9 \text{ g/m}^2$ . Blanks AF1, AF2 and AF4 had a higher lubricant amount on the side A whereas blanks AF3 had a marginally higher lubricant amount on the side B. Blanks AF1 and AF2 and AF4 had a comparatively similar lubricant amount of about  $0.78 \pm 0.2 \text{ g/m}^2$  on the side A. However, the average lubricant amount for blanks AF4 was about  $0.50 \text{ g/m}^2$  on the side B, which is notably lower than for blanks AF1 and AF2 ( $0.66 \pm 0.1 \text{ g/m}^2$ ). A lower lubricant amount on the lower side of blanks is common, due to the work of gravity force during application of lubricants. This is typically compensated by lower surface roughness so mixed lubrication conditions are still provided during forming operation.

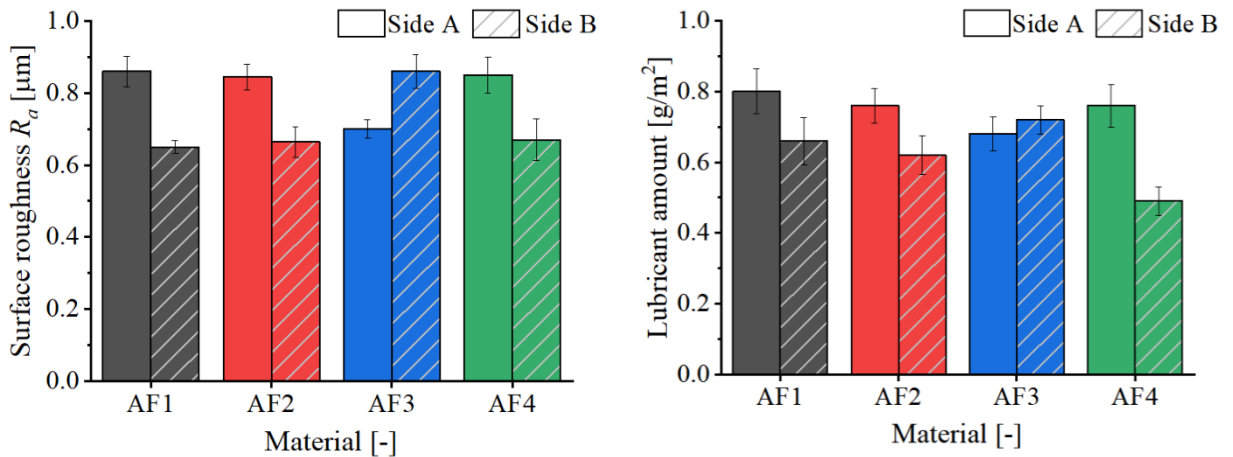


Figure 57 (a) Surface roughness  $R_a$  and (b) lubricant amount of blanks AF1-AF4

Figure 58 shows the influence of blank alignment on the critical BHF's determined after 6 months of NA using the A-Tool and the forming velocity of (a) 10 mm/s and (b) 100 mm/s. Forming in

upside-down alignment provided notably higher critical BHF for blanks AF1, AF2 and AF4 but lower critical BHF for blank AF3. A decrease of  $F_{\max}$  for 120 kN was observed for blank AF3 in upside-down alignment, for each of both forming velocities, i.e., 10 mm/s and 100 mm/s. This was also observed during the forming tryouts after 9, 12, 15 and 18 months of NA. Blank AF4 had the highest increase of  $F_{\max}$ , which increased for 200 kN and 260 kN in upside-down alignment for forming velocities of 10 mm/s and 100 mm/s, respectively. Blanks AF1 and AF2 had an increase of  $F_{\max}$  for 80-100 kN in upside-down alignment. Increase of the critical BHF for blanks AF1, AF2 and AF4 during the forming in upside-down alignment was mainly caused by the initial blank form of convex curved blanks. After the tool closing, i.e., clamping of already bent-in blanks, the initial form of blanks provided slightly more material for the forming operation than for concave blanks. This had a positive effect on the formability and led to the increase of critical BHF. However, this was not observed for concave curved blanks, which had a plane form prior to forming.

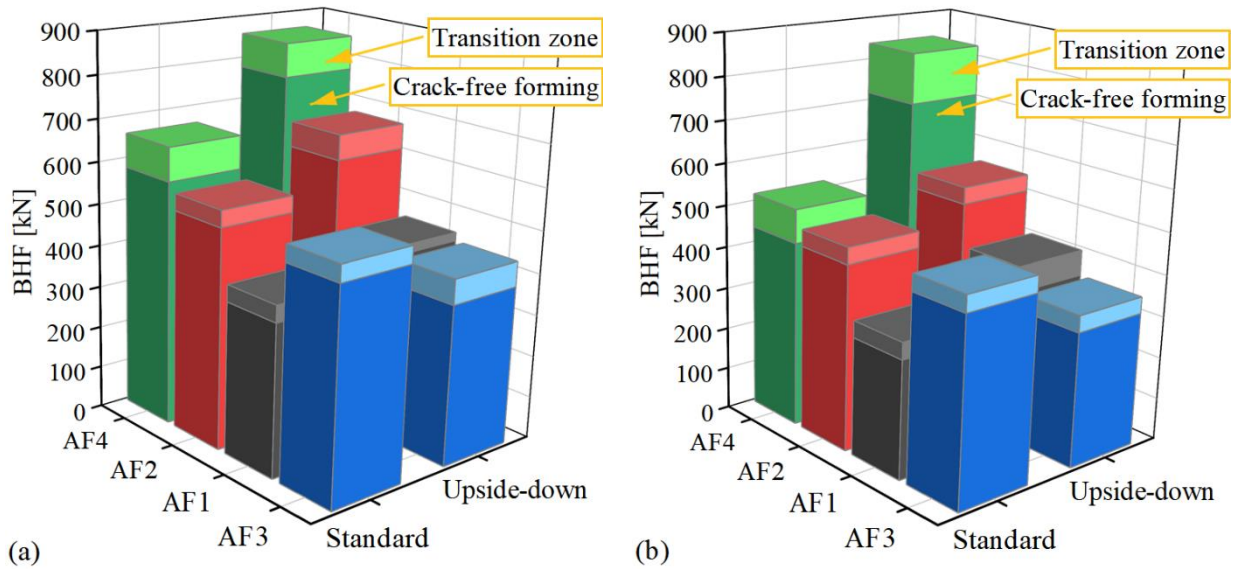


Figure 58 Effect of blank alignment on the critical blankholder forces of blanks AF1-AF4 at the forming velocity of (a) 10 mm/s and (b) 100 mm/s

Figure 59 shows the effect of blank alignment on  $D_{\max}$  determined using the CS-Tool after 9 months of NA at the forming velocity of 10 mm/s and at the BHF of (a) 400 kN and (b) 600 kN. Due to the shape of the blankholder and smaller blank size, the initial blank form was not affected by the blank alignment. Thus, the effect of initial blank form on the formability was neglectable for the CS-Tool. Moreover, forming the circular blanks for the CS-Tool in upside-down alignment provided information about the influence of surface roughness and lubrication amount on  $D_{\max}$ , i.e., the formability. Turning the blanks upside-down prior to forming had no significant effect on  $D_{\max}$  of blanks AF1, AF2 and AF3 at each of both BHF. However,  $D_{\max}$  of blanks AF4 decreased by about 0.6 mm and 1.3 mm after forming the circular blanks in upside-down alignment for BHF of 400 kN and 600 kN, respectively. This is due to the significantly lower lubricant amount measured at the side B of blanks AF4, that negatively affected the tribological

conditions during the forming. Evidently, having better tribological conditions between the die and blank was more beneficial for the formability determined using the CS-Tool than between blank and the blankholder / the punch. This is mainly due to the amount of contact and relative motion between the tool parts and blank material during forming. The contact and relative motion was more extensive over the die radii than over the punch radii. Therefore, enhancing the tribological conditions on the side of the blank that exhibit more extensive contact and relative motion with the tool parts is more beneficial for the formability.

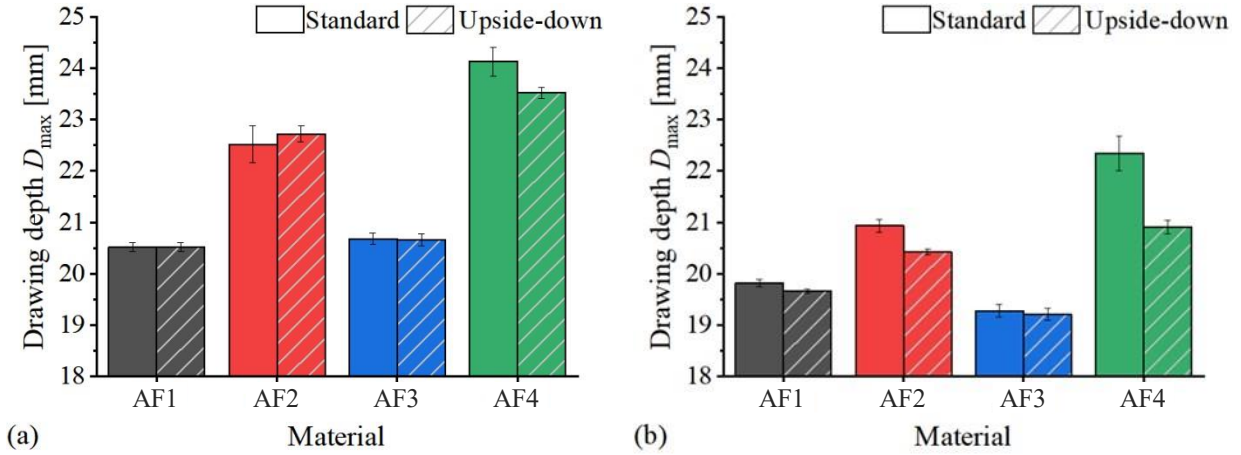


Figure 59 Effect of blank alignment on the maximum drawing depth of blanks AF1-AF4 determined using the CS-Tool, forming velocity of 10 mm/s and BHF of (a) 400 kN and (b) 600 kN

Regarding the convex curvature in as-received condition, lower surface roughness and lower lubricant amount at the side A, a conclusion can be drawn that blanks AF3 were reversely decoiled prior to cutting to length and blanks AF1, AF2 and AF4 were standard decoiled. Forming tryouts using convex curved blanks overestimated the formability determined using the A-Tool, so the valid formability was determined using the concave curved blanks. Thus, the actual formability of blanks AF3 determined using the A-Tool is actually lower than previously estimated. Figure 60 shows  $F_{max}$  for blanks AF1-AF4 determined with forming velocity of (a) 10 mm/s and (b) 100 mm/s using concave curved blanks. Actual  $F_{max}$  for blanks AF3 was 120 kN lower for each of both forming velocities. The resulting formability of blanks AF3 determined using the A-Tool was similar to the formability of blanks AF1, which agrees well with the forming results determined using the CS-Tool.

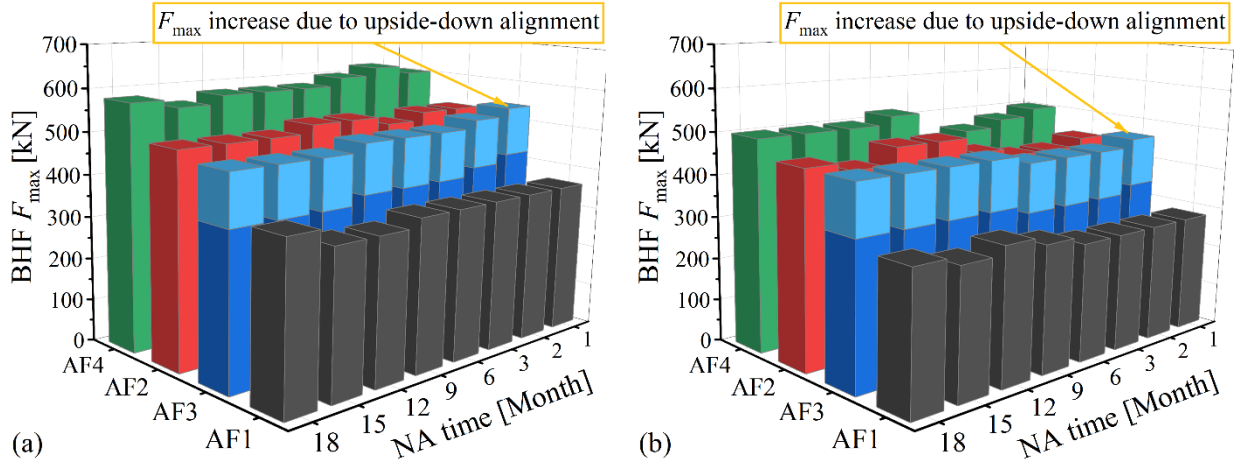


Figure 60 Actual maximum blankholder forces  $F_{\max}$  considering blank alignment for the forming velocity of (a) 10 mm/s and (b) 100 mm/s

### 6.1.2 Formability discussion

The formability analysis of Al-Mg-Si blanks using deep drawing tools is a complex procedure that requires consideration of various influencing factors apart from process parameters. Initial blank form, surface roughness, lubrication type, and amount can affect the formability of the blanks. The curvature of blanks, which can be also interpreted as slight pre-deformation, can be used as an advantage for improving the formability of blanks. Based on the forming results obtained using the A-Tool and the CS-Tool, blanks AF 4 exhibited the best formability, followed by blanks AF2 whereas blanks AF1 and AF3 had comparatively similar formability. Simultaneous increase of formability and strength can be achieved by optimization of chemical composition. Increasing the Si content in blanks AF2 promoted the formability notably compared to blanks AF1, which is also reported in several research works [116–118]. Furthermore, the formability of blanks AF3 was not as high as first determined using the A-Tool because of blank alignment. But despite considerable differences in strength and chemical composition between blanks AF1 and AF3, their formability was in a similar range. It seems that a negative effect on formability that was expected by reducing the Si content for blanks AF3 was compensated by increasing the Mg content. This is in contradiction to some previous studies that reported a negative or an insignificant effect of Mg content on the formability [117,118]. Thus, increasing Si and Mg content promoted the formability of investigated Al-Mg-Si alloy blanks, but the effect of Si was more pronounced. Compared to the optimization of chemical composition, the effect of lubrication and tribological conditions on the formability was even more significant. Applying PL 39 SX lubricant instead of Drylube E 1 improved the tribological conditions during the deep drawing. This led to notable increase of  $D_{\max}$  during the forming using the CS-Tool and almost doubling the critical BHF during the forming using the A-Tool. Moreover, the obtained formability of blanks AF1-AF3 was not in direct relation with the tensile ductility or the  $n$ -values. Blanks AF1, which had the highest tensile ductility and  $n$ -values, showed similar formability to blanks AF3, which had the lowest tensile ductility and  $n$ -values. This finding is contrary to some research works, that reported a positive effect of higher  $n$ -values on the formability of Al-Mg-Si alloys by preventing the strain localization [119,124,125]. However, a relation between the formability and the planar anisotropy  $\Delta r$  was found. Blanks

AF2, which had the lowest planar anisotropy  $\Delta r$  of about 0.2 showed the best formability whereas the blanks AF1 and AF3 with similar planar anisotropy  $\Delta r$  of about 0.3, also showed similar formability. Note that blanks AF1-AF3 had almost identical average normal anisotropy  $r_m$ . This agrees well with the findings of Sidor et al. who reported that formability of AA6016 blanks depends rather on  $r$ -values than on  $n$ -values [126]. Moreover, the formability of Al-Mg-Si blanks was related to  $r$ -values since both remained relatively constant within 1-18 months of NA. Thus, tracing the changes of  $r$ -values during NA might be an indicator of potential formability deterioration. Contrary,  $n$ -values constantly decreased during the NA so a direct relation between the formability and  $n$ -values was not confirmed. However, strengthening due to clustering of the Mg and Si atoms during NA did not affect the formability of the Al-Mg-Si alloy blanks at each of both forming velocities. Therefore, a typical shelf life of 6 months for blanks from this alloy series can also be extended with regards to the formability. Forming at high forming velocity decreased the formability of blanks AF1-AF4 due to strain rate effects. Nevertheless, the decrease of formability at high forming velocity was independent on applied BHF. Although the formability was affected by the increasing BHF and forming velocity, the order of the blanks in terms of  $D_{\max}$  or  $F_{\max}$  remained the same for each of forming parameters.

## 6.2 Influence of NA on the bendability

Influence of NA on the bendability is shown in Figure 61 (a), (b) and (c) for blanks AF1, AF2 and AF3, respectively. Due to issues with the plate bending fixture, the maximum bending angle  $\alpha_{\max}$  observed after 1 month of NA was significantly lower. After 2 months of NA, the highest  $\alpha_{\max}$  of 141.8° was observed for blanks AF1, whereas  $\alpha_{\max}$  of 140.9° was observed for blanks AF3 and of 140.2° for blank AF2. Despite significant differences in the strength and in the tensile ductility, blanks AF1-AF3 showed comparatively similar bendability. However,  $\alpha_{\max}$  observed after 3 months of NA for blanks AF1 was virtually higher (142.6°) than  $\alpha_{\max}$  after 2 months of NA. Generally, clustering of Mg and Si atoms during NA negatively affected  $\alpha_{\max}$ , which constantly decreased. Moreover, the decrease of  $\alpha_{\max}$  was more notable for the Al-Mg-Si blanks with faster aging kinetics. Compared to the highest  $\alpha_{\max}$  observed during the NA, a decrease of about 8.3°, 7.6° and 4.5° was observed after 18 months of NA for blanks AF3, AF2 and AF1, respectively. Constant decrease of maximum bending angle during NA was also reported by Prillhofer et al. [43] for 4 Al-Mg-Si alloy blanks. They observed a decrease of 5–12° within 1-6 months of NA. Deterioration of the bendability with increasing NA time was also observed elsewhere [31,93,94].

Since  $n$ -values constantly decreased within 1-18 months of NA, it seems that the deterioration of bendability during NA correlated with the decrease of strain hardening exponent. Higher  $n$ -values are generally beneficial for the bendability [127]. Decreasing  $n$ -values reduced the width of plastic deformation zone during the bending and promoted the localization of plastic straining at the outer bending radius. The strain localization led to earlier cracking and therefore to reduction of  $\alpha_{\max}$ . Ogura et al. [39] also found a correlation between  $n$ -values, which decreased during NA, and bendability deterioration for AA6022. They concluded that the bendability is influenced by the interaction between clusters and dislocation movement, which represented

plastic deformation. Moreover, D.K. Leu [68] reported that the bendability of anisotropic sheet metals depends more on  $n$ -values than on  $r$ -values.

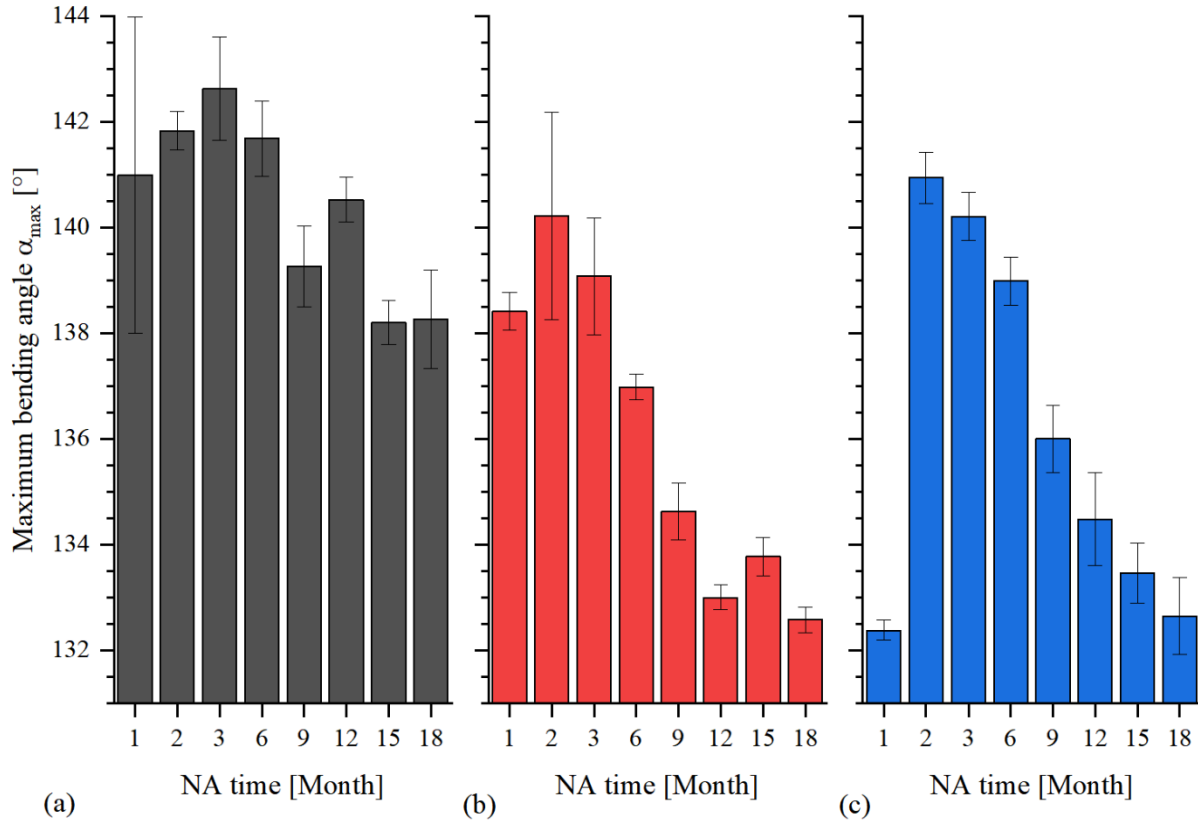


Figure 61 Influence of NA on maximum bending angle of blanks (a) AF1, (b) AF2 and (c) AF3

Effect of 10% pre-straining on the bendability of blanks AF1, AF2 and AF3 after 18 months of NA is shown in Figure 62. Obviously, the bendability of blanks AF1 was only slightly better than the bendability of blanks AF2 and AF3 for bending plates without pre-strain. However, application of 10% pre-strain reduced  $\alpha_{\max}$  of blanks AF2 and AF3 significantly, from about  $132.5^\circ$  to about  $110^\circ$ . Decrease of  $\alpha_{\max}$  after pre-straining was related to the failure mechanism at the outer surface, which occurs due to tensile strains. Additional tensile strains accelerated the crack initiation at the outer surface of bent samples. Surprisingly, the pre-straining of the plate bending samples did not affect the  $\alpha_{\max}$  for blanks AF1. Bendability deterioration of Al-Mg-Si blanks due to pre-straining was also reported elsewhere [31].

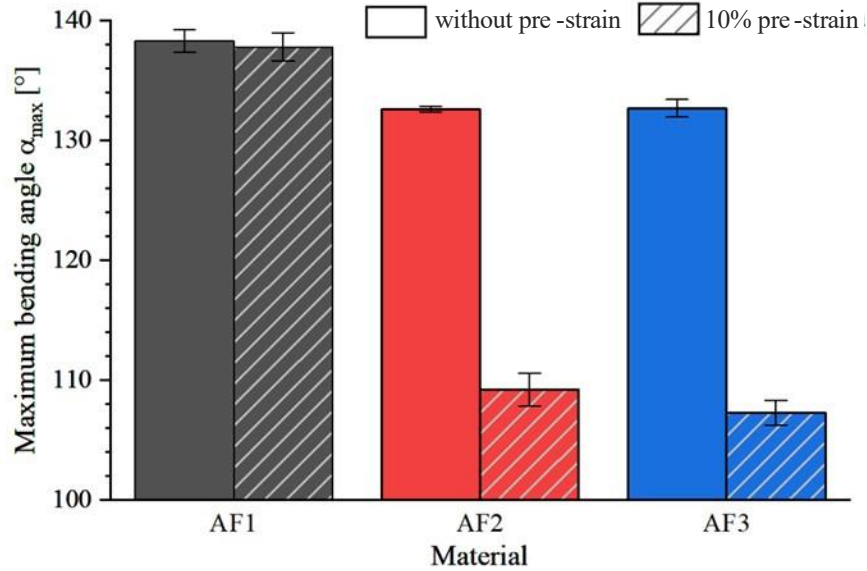


Figure 62 Influence of pre-straining on the maximum bending angle of blanks AF1, AF2 and AF3

### 6.3 Influence of NA on the forming limits

The influence of the NA on the forming limits of blanks AF1, AF2, and AF3 is shown in Figure 63 (a), (b), and (c), respectively. Forming limits were analyzed for 3 specific areas of the forming limit diagram, i.e., tension-compression (minor strain < 0), plane strain (lowest major strain and minor strain about 0), and biaxial tension (minor strain > 0). The investigated Al-Mg-Si blanks obtained comparatively similar forming limits despite relatively big differences in strength and in ductility. After 3 months of NA., each of the blanks had a major strain of about 0.22 for the limiting strains in the plain strain area. A high scattering was observed for the limiting strains in the biaxial tension area so a clear trend during the NA was not detectable. However, the forming limits remained relatively constant in the tension-compression diagram area within 1-18 months of NA and the plane strain diagram area within 3-6 months of NA for each of the blanks. The forming limits in the plane strain area were not determined after 1 month of NA, and after 18 months of NA the Nakajima samples were not cracking in the central area but near the clamping area as shown in Figure 64. According to the standard ISO 12004, the test is valid only when cracks occur in the central area of the sample. Since the limiting strains were evaluated in the central area of the sample, they were significantly lower in the moment of cracking and therefore invalid. The cracking of the samples near the clamping area also occurred for the biaxial tension samples after 18 months of NA. This phenomenon might be related to the bendability deterioration due to NA, but additional investigation is required. Prillhofer et al. [43] observed a slight decrease in the forming limits within 2-6 months of NA for 4 Al-Mg-Si alloy blanks. Moreover, Tian et al. observed a slight decrease of the forming limits in the biaxial tension area of the FLD for Al-Mg-Si alloy blanks in T4 condition compared to the same blanks in solutionized condition. However, the decreases of the forming limits observed by Prillhofer et al. [43] and Tian et al. [49] were significantly lower than scattering of the limiting strains shown in Figure 63. Hence, the influence of NA on the forming limits of Al-Mg-Si alloy blanks can be seen as neglectable.

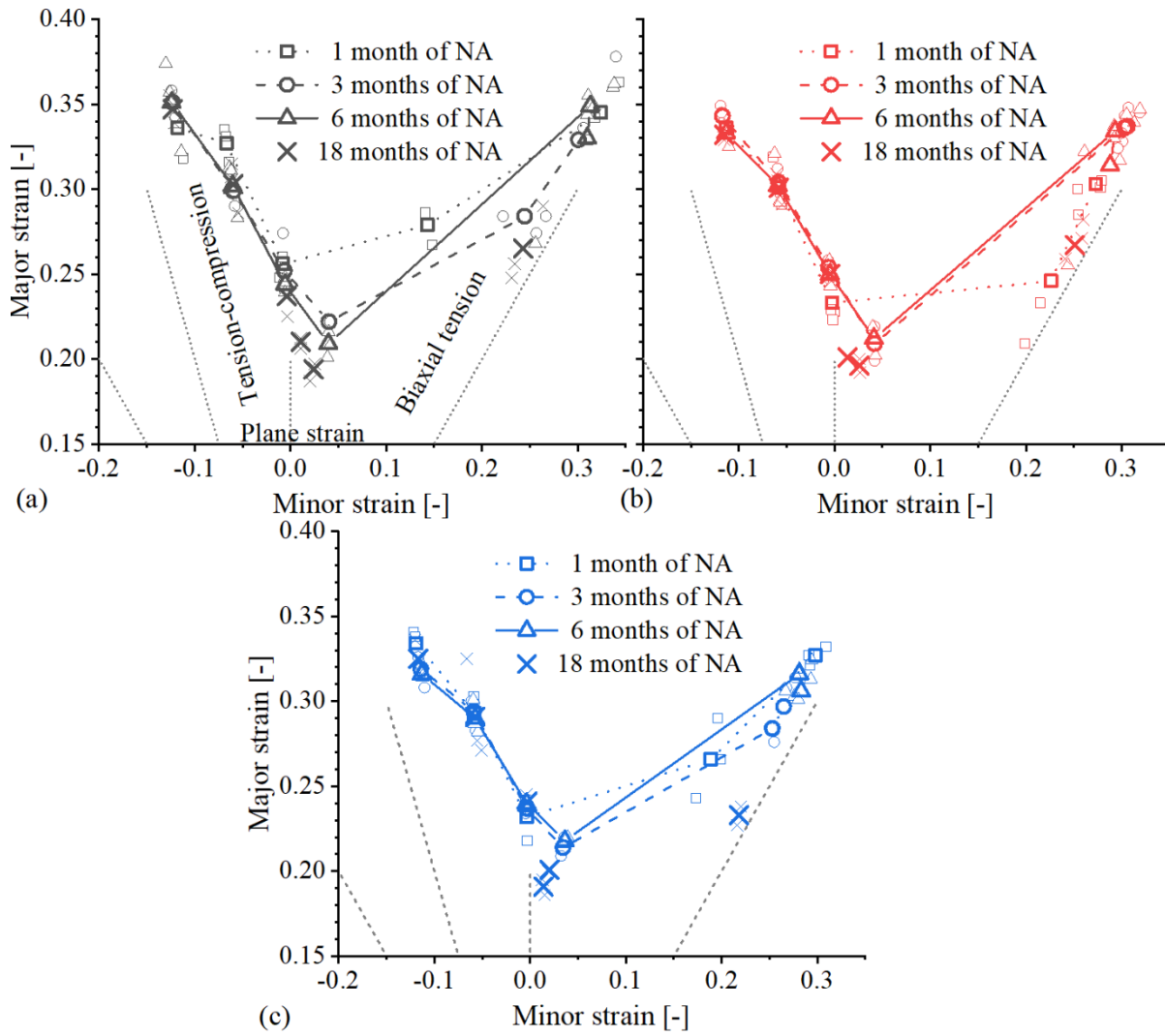


Figure 63 Influence of NA on the forming limits of blanks (a) AF1, (b) AF2 and (c) AF3

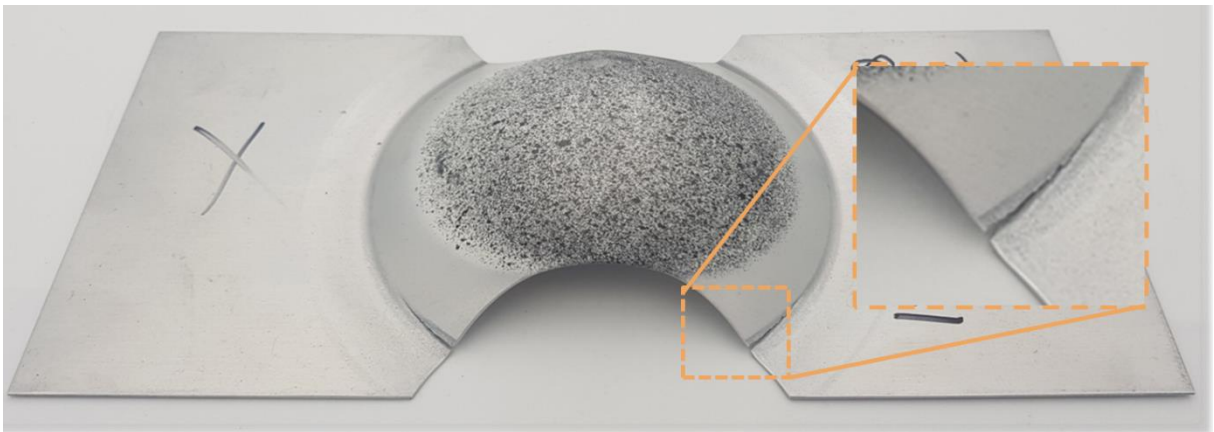


Figure 64 Cracking of the Nakajima samples close to the clamping area

## 7 Pin-on-plate friction tests

Figure 65 (a) – (d) exemplary illustrates the influence of initial contact pressure on CoF profiles over sliding distance for blanks AF1-AF4, respectively. Sharp peaks observed at the beginning of the sliding represented the transition from static friction to dynamic friction. Subsequently, the CoF stabilized and remained relatively constant over the remaining sliding distance for each sliding condition. Continuous fluctuations of the CoF were observed during the sliding of steel pins. However, the amplitude of fluctuations over the sliding distance decreased with increasing initial contact pressures. This indicates that the friction tests were more stable at higher contact pressures. Moreover, increasing the initial contact pressure between the pin and the aluminum plates also resulted in a reduction of CoF.

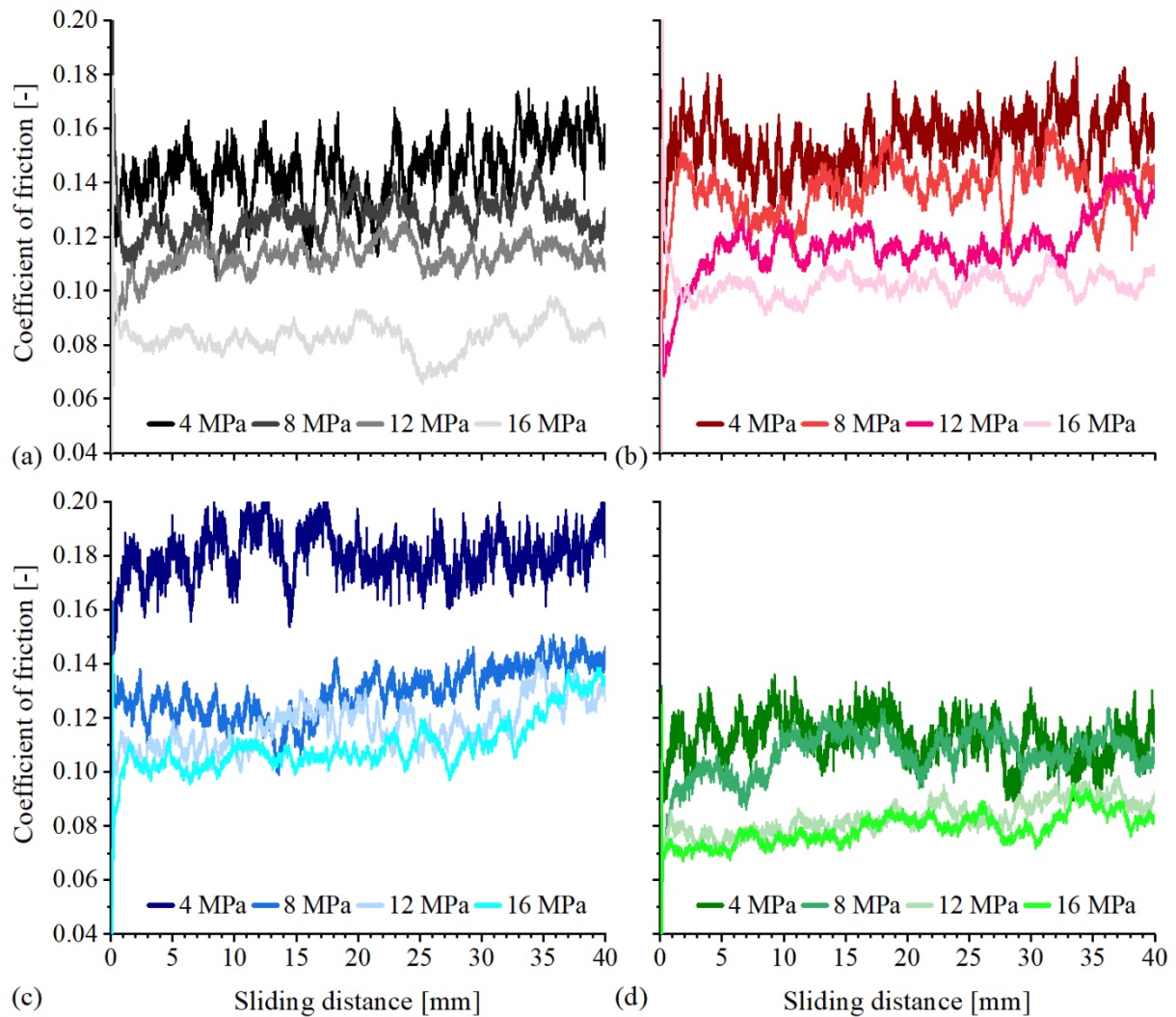


Figure 65 Exemplary illustration of CoF profiles as function of the sliding distance for blanks (a) AF1, (b) AF2, (c) AF3 and (d) AF4

Average CoF at initial contact pressures of 4-16 MPa for blanks AF1-AF4 are shown in Figure 66. As expected, the average CoF constantly decreased with increasing contact pressures for

each of the investigated Al-Mg-Si blanks. However, the decrease of the CoF was more dominant at the low initial contact pressures than at high contact pressure. Evidently, this implies the exponential dependency of CoF on the initial contact pressures. Moreover, only minor changes of CoF for initial contact pressures higher than 16 MPa are expected.

The highest average CoF was observed for blanks AF3. This is likely due to the high strength of blanks AF3, which was the main difference compared to other investigated blanks. The remaining factors that can affect the tribological conditions such as surface roughness and lubricant amount were almost identical for each of blanks. The average CoF for blanks AF3 decreased from about 0.18 at the lowest initial contact pressure of 4 MPa, to about 0.11 at the highest initial contact pressure of 16 MPa. Blanks AF1 and AF2 showed comparatively similar average CoF, which decreased from about 0.15 at 4 MPa to about 0.10 at 16 MPa. The difference in average CoF between blanks AF1-AF2 and blanks AF3 was higher at comparatively low contact pressures but decreased to about 0.01 at the highest initial contact pressure. This may be related to the mechanism of plastic deformation of surface asperities. The angle of attack changes at high contact pressures, and the contact area enlarges. This leads to an unproportional increase of the normal and the frictional forces, which directly affects the value of CoF. Moreover, it seems that the average CoF converged to a value of about 0.10 at contact pressures significantly higher than 16 MPa. However, the lowest average CoF was observed for blanks AF4. Compared to blank AF1, the average CoF was lower by about 0.04 at 4 MPa and by 0.02 at 16 MPa. Note that the only difference between blanks AF1 and AF4 was the type of lubricant. Thus, it can be concluded that the improvement of the formability observed for blanks AF4 was only due to the improvement of tribological conditions through the reduction of CoF.

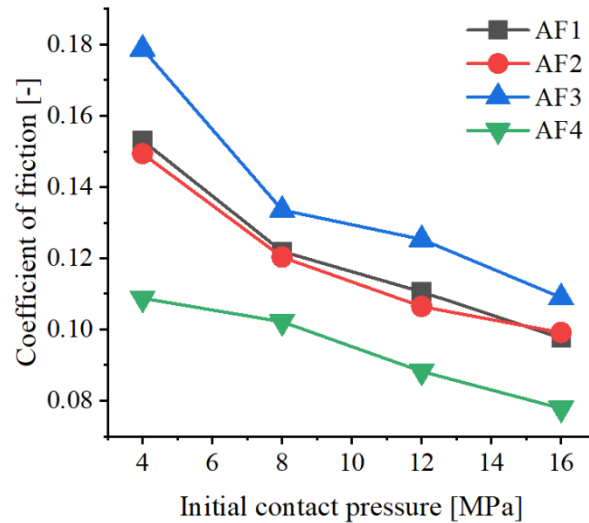


Figure 66 (a) Average CoF as function of the initial contact pressure for blanks AF1-AF4 and

## 8 Numerical forming simulation

### 8.1 TriboForm friction model

Figure 67 illustrates the effect of the contact pressure and the sliding velocity on CoF in the TF models for blanks AF1-AF4. CF models with the constant CoF of 0.10 and of 0.08 are also illustrated in Figure 67. Exponential functions were used to describe the dependency of CoF on the contact pressure and the sliding direction in the TF models. Based on the surface shapes of these models, some conclusions can be drawn. Evidently, the effect of the contact pressure on CoF is more significant than the effect of the sliding velocity. Visual change of CoF was detectable for slight changes of the contact pressure whereas high variations of the sliding velocity were necessary for visually detecting the changes of CoF. Moreover, the effect of sliding velocity on CoF was minor at very low contact pressures, but it was more pronounced at comparatively high contact pressures. CoF in the TF models was clearly higher than for CF models at the low contact pressures. However, CoF in the TF models was significantly lower than for CF models at very high contact pressures and sliding velocities. This indicates that the TF models could be particularly meaningful for numerical forming simulations of complex components, that may locally exhibit various combinations of contact pressure and sliding velocity. On the other hand, CF models can provide accurate results in numerical forming simulations if the combination of contact pressures and sliding velocity remains locally similar over the entire component geometry for the entire period of forming operation.

As expected, the trends of the CoF in the TF models were identical to the results from the friction tests. The highest CoF were predicted for blanks AF3 and the lowest for blank AF4 whereas blanks AF1 and AF3 had comparatively similar CoF. Moreover, the differences between the TF models were higher at low contact pressures and low sliding velocities. CoF converged to the same value of about 0.03 for each of the blanks at high contact pressures and high sliding velocities.

The blank surface in the flange area shrinks during the forming operation due to the material flow into the tool cavity. Since the blankholder force is directly applied at this area of blank, the reduction of the blank surface leads to an increase of local contact pressures during forming operation. At the BHF of 400 kN the contact pressures in the flange area of the CS-Tool were about 11 MPa after the tool closing and about 12.5 MPa at the drawing depth of 20 mm. At the same BHF of 400 kN, the contact pressures in the flange area of the A-Tool were about 4.5 MPa at the moment of tool closing and about 5.5 MPa at the bottom dead center of the tool. This range of contact pressures correlates well with the range of contact pressures applied in the friction tests. Hence, the validation of the TF model was done using the CS-Tool for the high contact pressures and using the A-Tool for the low contact pressures. Moreover, the TF models were validated at the forming velocity of 10 mm/s for the A-Tool and CS-Tool, and at the forming velocity of 100 mm/s for the A-Tool. However, the forming velocity differs from the sliding velocity. The forming velocity was related to the tool displacement and the sliding velocity to the relative movement between blank and the tool surfaces. The actual sliding velocities were locally very different but, in general, they were lower than the forming velocity. The forming

operations were performed at room temperature so the effect of temperature was not investigated in numerical forming simulations although the initial tool surface temperature may increase during the forming operation. Rapid forming of aluminum components may induce heat through friction and plastic deformation, which can occur in industrial applications. However, the hydraulic press used in the forming tryouts required relatively high waiting times for the refilling of the oil container between each forming operation. Hence, relatively high waiting times allowed the generated heat to dissipate from the tool surface, so the initial temperature of the tool surface remained similar to the ambient temperature during the forming tryouts.

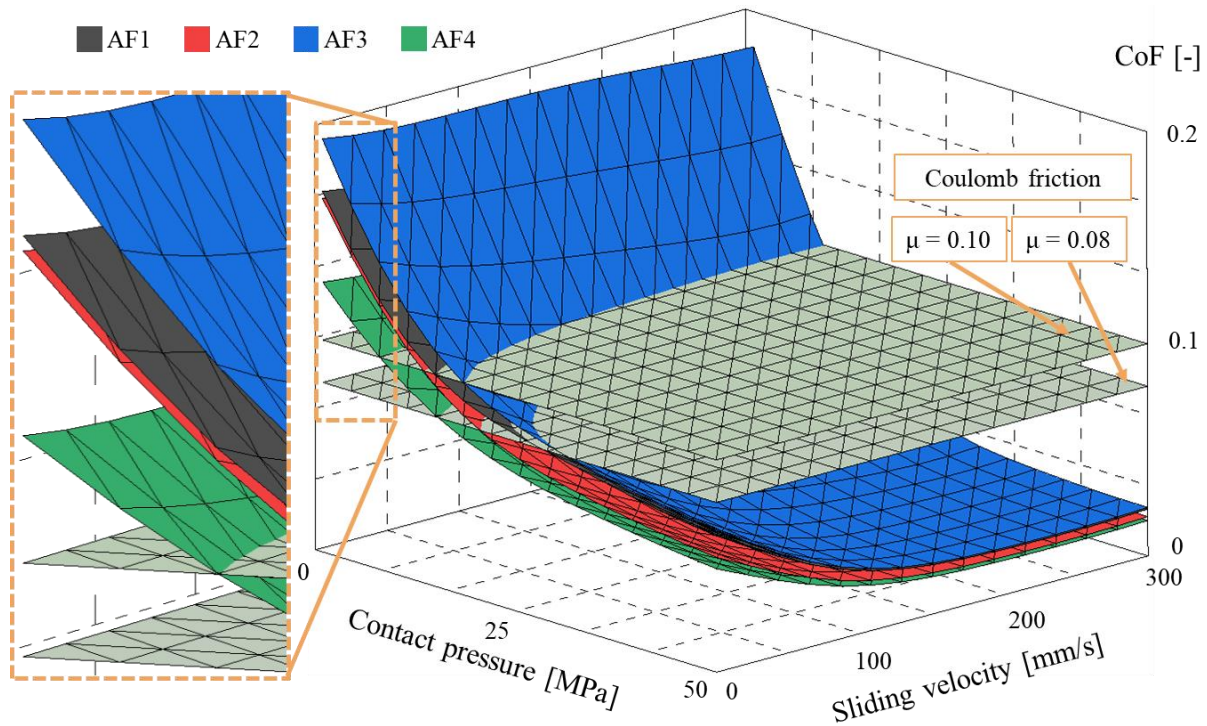


Figure 67 Dependency of CoF on contact pressure and sliding velocity in TriboForm friction models for blanks AF1-AF4

## 8.2 Forming simulation at low forming velocity of 10 mm/s

### 8.2.1 Strains

Experimentally and numerically determined FLDs of components formed using the A-Tool are shown in Figure 68 for blanks (a) AF1, (b) AF2, (c) AF3 and (d) AF4. The FLDs of components from the experiments, numerical forming simulation with the TF model and numerical forming simulation with the CF model are shown in the upper, the middle, and the lower row, respectively. FLDs of the experimentally and numerically formed components were analyzed based on the shape of the diagrams using peaks marked 1-5. The occurrence of peaks was related

to differences in strain state in different component areas. Figure 69 shows changes in blank material due to straining for a component formed using the A-Tool.

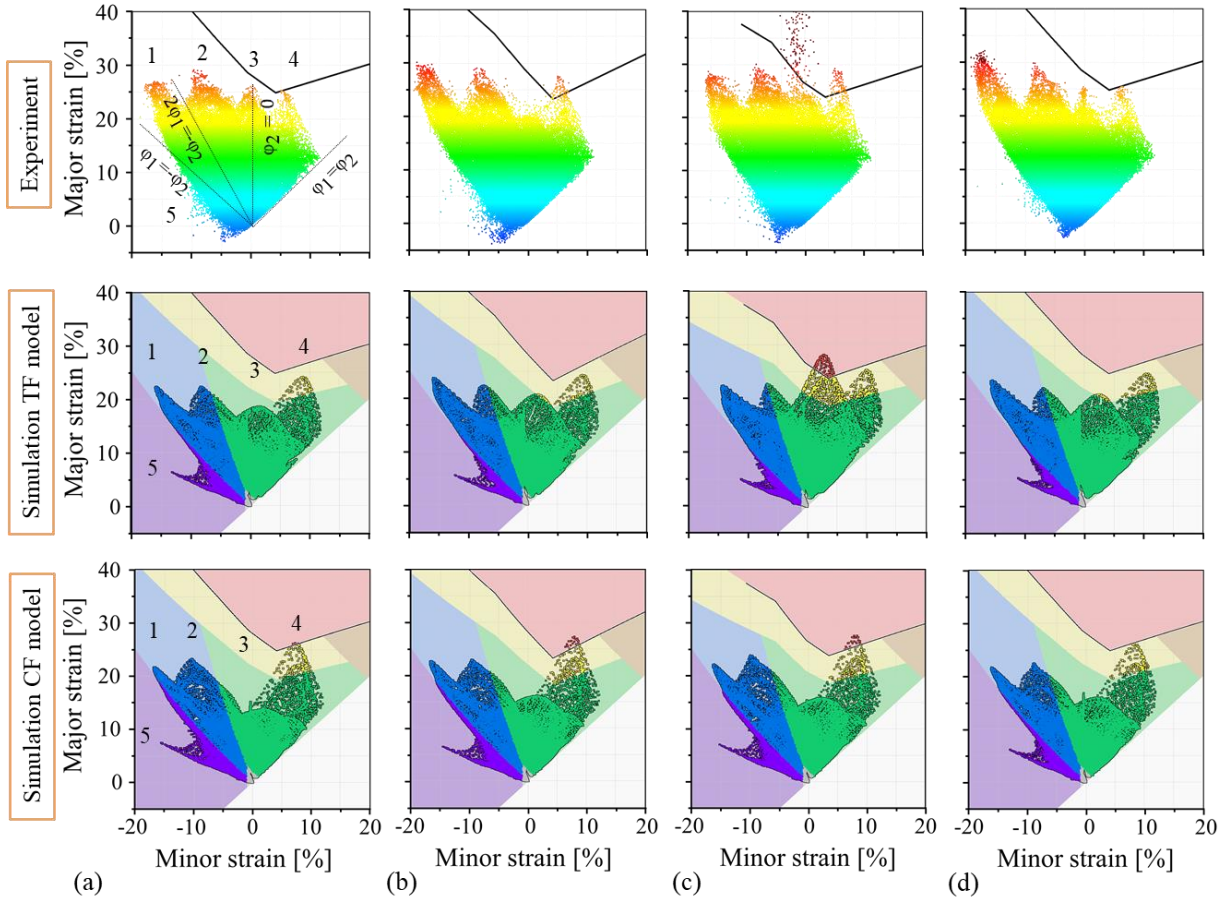


Figure 68 Experimentally and numerically determined FLDs using the A-Tool for blanks (a) AF1, (b) AF2, (c) AF3 and (d) AF4 after 3 months of NA

Peak 1 occurred between pure shear and uniaxial tension strains. The strains obtained in peak 1, which are typical for deep drawing behavior, were detected around the corners of rectangular A-Tool components close to the die radii area. Major strains of about 26-31% were measured for the experimentally formed components. However, the numerically determined strains were lower by about 3-5%, for each of both friction models. Yet, the numerical forming simulation with the TF model provided marginally better results for peak 1. Peak 2 occurred between uniaxial tension and plane strains. These strains were observed at the component area that passed the drawbeads, and around the strains of peak 1. Maximum major strains of about 30% were obtained in the experiment, and numerical forming simulations with each of both friction models provided similar major strains of about 25% for peak 2. Peak 3 occurred due to an increase of plane strains at the critical corner marked with an arrow in Figure 29. This peak is the most important for failure prediction since components cracked due to exceeding strain limits in this area. The strains of peak 3 were close to the FLC for the experimentally formed components,

except for blanks AF3 which notably exceeded the FLC. Just slightly lower major strains for peak 3 were predicted by the numerical forming simulations with the TF model. This model also successfully predicted the cracking of the component for blanks AF3. However, the numerical forming simulation with the CF model evidently underestimated the strains of peak 3 and even for the blank AF3 remained far below the FLC. Peak 4 is characterized by biaxial tension. This type of strain occurred due to the forming of the 3 hemispherical hollows in the central area of components, which represents the door handle cups. Although the experimentally obtained strains were close to the FLC or exceeded the FLC, cracks were not observed during the forming tryouts. Numerical forming simulations with each of both friction models showed a good agreement with the experiments but simulations with the TF models showed slightly lower strains for peak 4. Furthermore, a miniature peak 5 with compressive strains was located under the pure shear strains. The strains in this peak were detected in the flange area on the outer side of the drawbeads. The flow of blank material through drawbead is restricted, which leads to the thickening of the blank material on the drawbead entrance. Peak 5 was clearly visible in the numerical forming simulations. This type of compressive strain was also visible in the experiments in the form of scattered points.

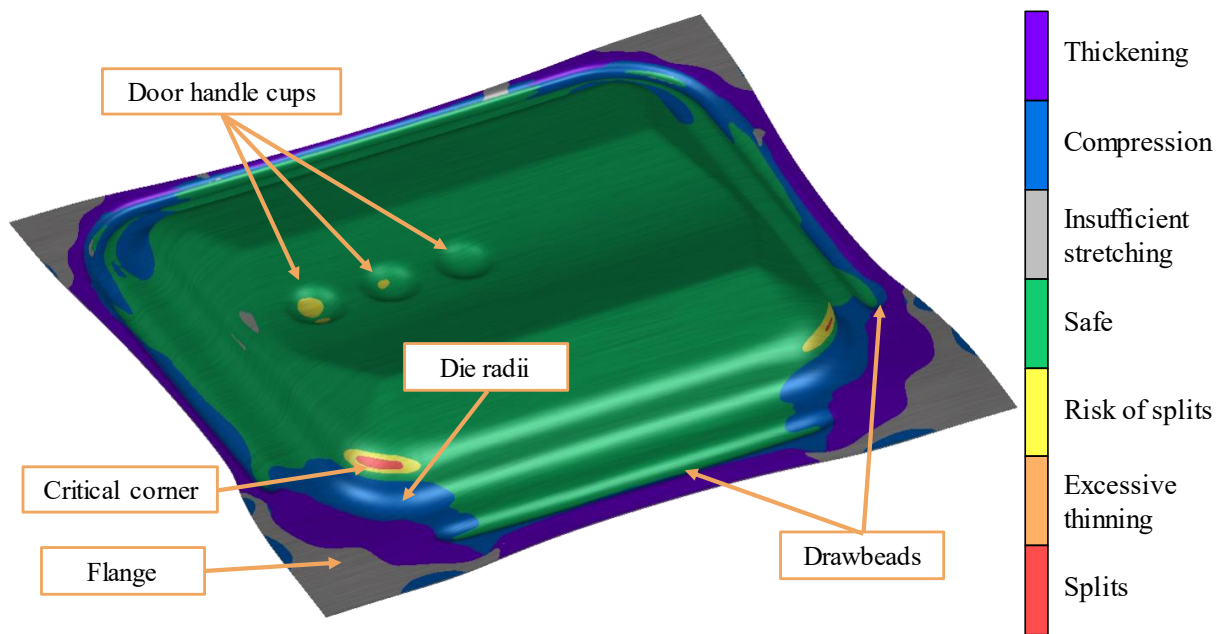


Figure 69 Behavior of blank material based on the induced strains for components formed using the A-Tool

Experimentally and numerically determined FLDs of components formed using the CS-Tool are shown in Figure 70 for blanks (a) AF1, (b) AF2, (c) AF3 and (d) AF4. The FLDs of components from the experiments, numerical forming simulations with the TF model and numerical forming simulations with the CF model are shown in the upper, the middle and the lower row, respectively. FLDs of the experimentally and numerically formed components were analyzed based on shape of the diagrams using peaks marked 1-4. The occurrence of peaks was related to

differences in strain state in different component areas. Figure 71 shows changes of blank material due to straining for a component formed using the CS-Tool. Peak 1 was observed close to uniaxial tension strains. These strains, which are typical for deep drawing operations, were detected on the transition from the flange to the die radius but only in the direction of cross arms and not between the cross arms as shown in Figure 71. The height of this peak depends on material flow and drawing depth so components with a higher drawing depth obtain higher major strains for this peak. However, the numerical forming simulations evidently underestimated the major strains in this area by about 5-10%. Peak 2 mainly occurred due to increasing plane strains at the upper corners of the cross arms as shown in Figure 71. However, high plane strains also occurred around the critical corner, which led to crack initiation. Shortly after crack initiation at the critical corner, cracks also initiated at the upper corner of the cross arms. In general, numerical forming simulations slightly underestimated the major strains for peak 2. Peak 3 occurred due to equibiaxial tension strains. These strains were detected at the transition area from the flange to the die radii between the cross arms. A good agreement between the experiments and the numerical forming simulations was detected for peak 3 since major strains in the range of 15-20% were obtained in both cases.

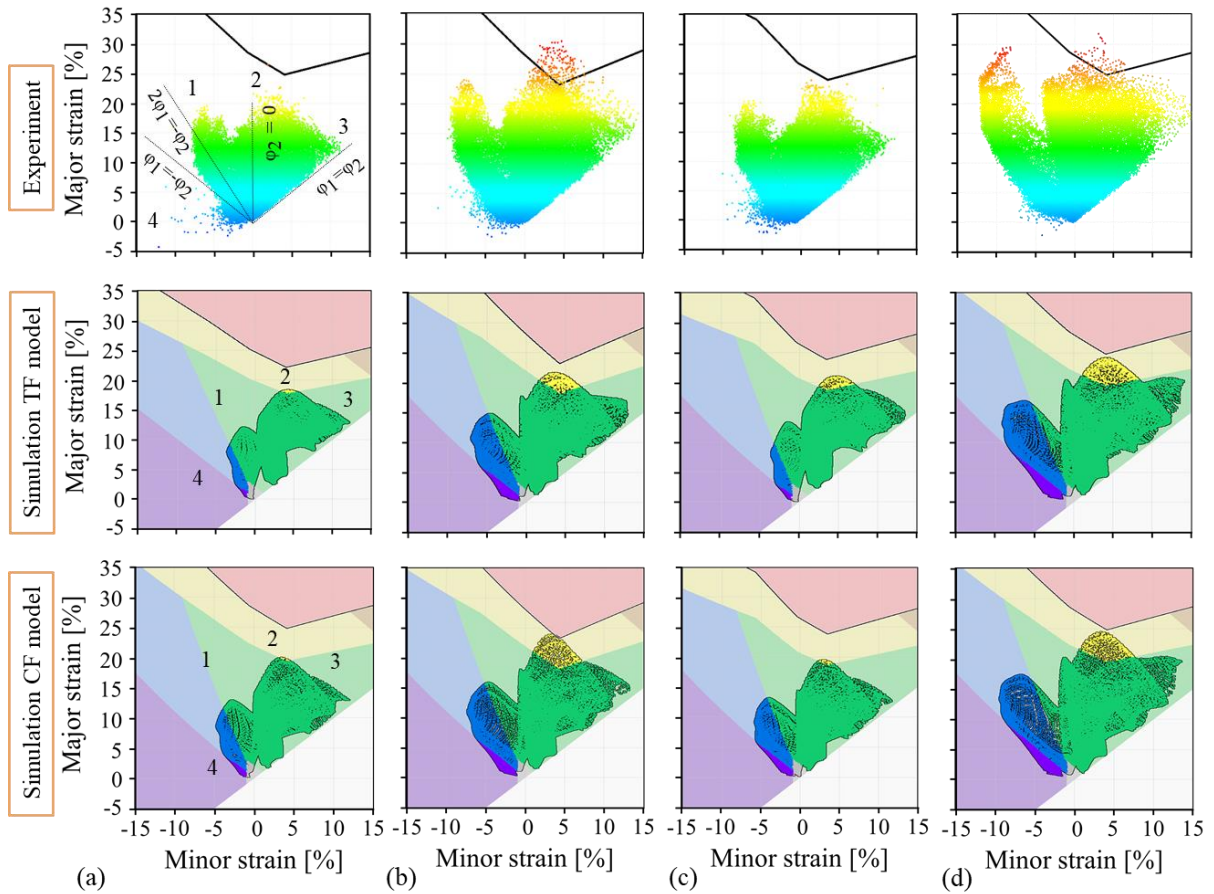


Figure 70 Experimentally and numerically determined FLD using the CS-Tool for blanks (a) AF1, (b) AF2, (c) AF3 and (d) AF4 after 3 months of NA

Both friction models provided very good predictions of the plastic strains distribution in numerical forming simulations. Moreover, the observed differences between the friction models were only minor but still notable. The notable difference occurred exactly at the most important area of the FLD for the failure prediction of deep-drawn components, i.e., plane strain. Namely, the prediction of the plastic strains was more accurate in this area of FLD for the numerical forming simulation with the TF Model than with the CF Model. This is likely due to the complex geometry of the A-Tool and complex tribological conditions observable during the forming of Al-Mg-Si alloy blanks. The TF model was able to successfully predict the critical plane strains and therefore potential failure due to crack initiation whereas the forming simulations with the CF model remained notable below the FLC in this area. However, a significant difference was not observed for the comparatively simple components formed using the CS-Tool. Note that the CoF for the CF models was chosen based on the experimentally obtained results so further improvement of the numerically obtained results was not possible. Moreover, this retroactive adaptation of the CoF is not possible for the tool design in the automotive industry. The tool makers require accurate forming simulation already in the design phase.

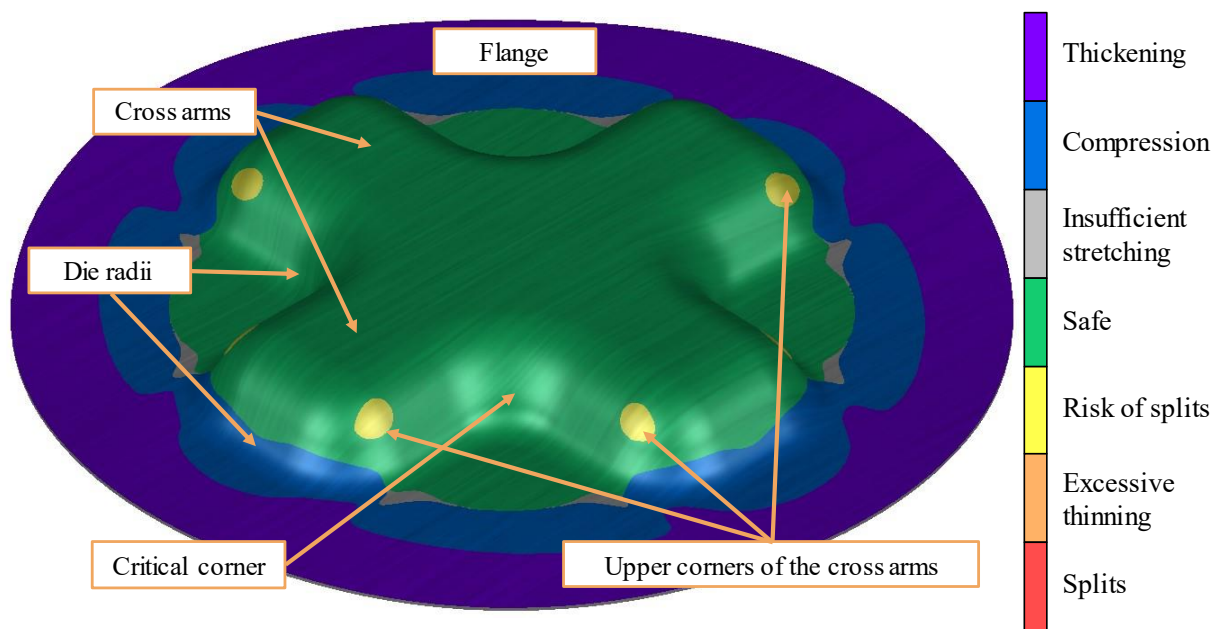


Figure 71 Behavior of blank material based on the induced strains for components formed using the CS-Tool

### 8.2.2 Forming forces

Figure 72 shows the experimentally and the numerically obtained forming forces using the A-Tool as a function of the tool displacement for blanks AF1-AF4. The forming forces profiles were displayed from the first punch-blank contact (tool displacement of 0 mm) to the bottom dead center (tool displacement of 53.4 mm). The forming forces were measured under the punch, which resulted in a vertical increase of the forming forces after reaching the bottom dead center. This was due to direct contact between the punch, the die and blank but without additional blank

deformation or tool displacement. The vertical increase of the forming forces was not included in the investigation since this phenomenon was not related to the plastic deformation of blanks or to the tribology. The forming forces remained relatively low during the first 20 mm of the tool displacement which was due to only local deformation of blanks around the higher design ridge. Subsequently, plastic deformation occurred in the other areas and the material flow intensified, which led to the exponential increase of the forming force profiles. CoF used in the numerical forming simulations with the CF model were chosen based on the best fit with the forming forces. Therefore, a very good agreement between the experiments and the simulations with the CF model was observed. Moreover, a good agreement was also observed between experiments and the numerical forming simulation with the TF model. However, the forming forces obtained with the TF model were minorly higher than the experimentally obtained forming forces for the tool displacement range of 25-45 mm.

Generally, the forming forces during cold forming are mainly affected by the applied BHF, material strength, blank thickness, and tribological conditions. Despite significant differences in the applied BHF, the lowest and comparatively similar forming forces were observed for the components formed with blanks having the same material strength, i.e., blanks AF1 and AF4. A higher BHF of 600 kN applied for the component formed with the blank AF4 was compensated with better tribological conditions, which resulted in similar forming forces as for the component formed with the blank AF1 and a BHF of 380 kN. BHF of 500 kN was applied during the forming of blanks AF2 and AF3. Due to higher material strength, slightly higher forming forces were needed for the forming of blanks AF3.

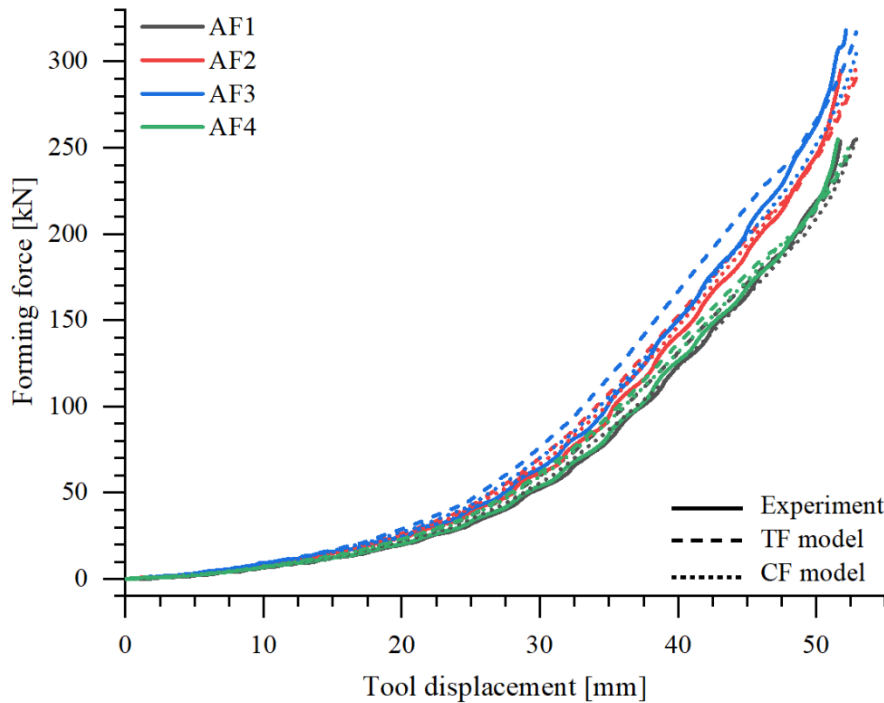


Figure 72 Experimentally and numerically obtained forming forces for the components formed using the A-Tool

Figure 73 shows the experimentally and the numerically obtained forming force using the CS-Tool as a function of the tool displacement for blanks AF1-AF4. The forming forces were displayed from the first punch-blank contact (tool displacement of 0 mm) to the maximum drawing depth, which was individually defined for each of the blanks. After the slower initiation phase in the first 5 mm of tool displacement, the forming forces almost linearly increased over the remaining tool displacement. The main forming mechanism was the bending of blanks over the die and the punch radius for the first 5 mm of the tool displacement. Subsequently, material flow and plastic deformation intensified, which resulted in a significant increase of the forming force. The increase in forming forces was comparatively faster than for the A-Tool despite smaller tool geometry. This is due to the geometry of the CS-Tool that ensured nearly full punch-blank contact from the forming start.

Application of the same BHF of 400 kN for each of the formed components provided a clear distinguishment between the forming force profiles. The slope of the profiles clearly increased with increasing strength for blanks AF1-AF3, which were lubricated with the Drylube E 1. Moreover, the better tribological conditions between the tool surface and blanks AF4 reduced the slope of the forming force profiles during the forming. Thus, the slope of the forming force profiles was notably affected by the strength of blanks and the tribological conditions. However, numerical forming simulations with each of both friction models, i.e., TF and CF model, provided a very good agreement with the experimentally obtained forming force profiles.

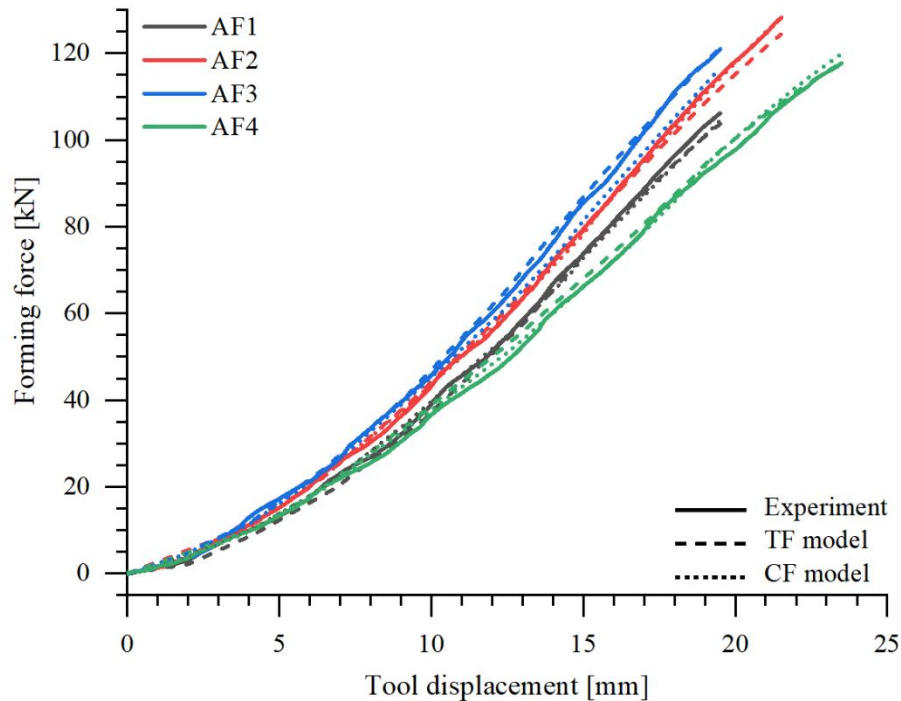


Figure 73 Experimentally and numerically obtained forming forces for the components formed using the CS-Tool

### 8.2.3 Thickness

Accurate computation of thickness change in numerical forming simulation is important for predicting potential failures of blank material such as necking or cracking. Necking, which refers to local, excessive thinning of blank material, occurs prior to cracking. The occurrence of excessive thinning is frequently not visually detectable. Thus, an in-depth analysis of thinning is necessary for detecting the onset of excessive thinning, which is an indicator of failure. The thickness analysis of the experimentally and the numerically formed components was conducted at the corners that cracked during forming when forming limits were exceeded. Figure 74 shows the corners and section planes that were used for the thickness analysis of components formed with (a) the A-Tool and (b) the CS-Tool. The section started in the flange area for each of the components (length along section = 0 mm), continued through the critical zone, and ended at about 140 mm of length along section. The ending point was the lower design ridge for the components formed using the A-Tool and the geometric center for the components formed using the CS-Tool. A positive thickness change represented the thickening, and a negative thickness change represented the thinning of the blank material. The thickness change at the experimentally formed components was measured using 3D optical scanning systems ARGUS and ATOS.

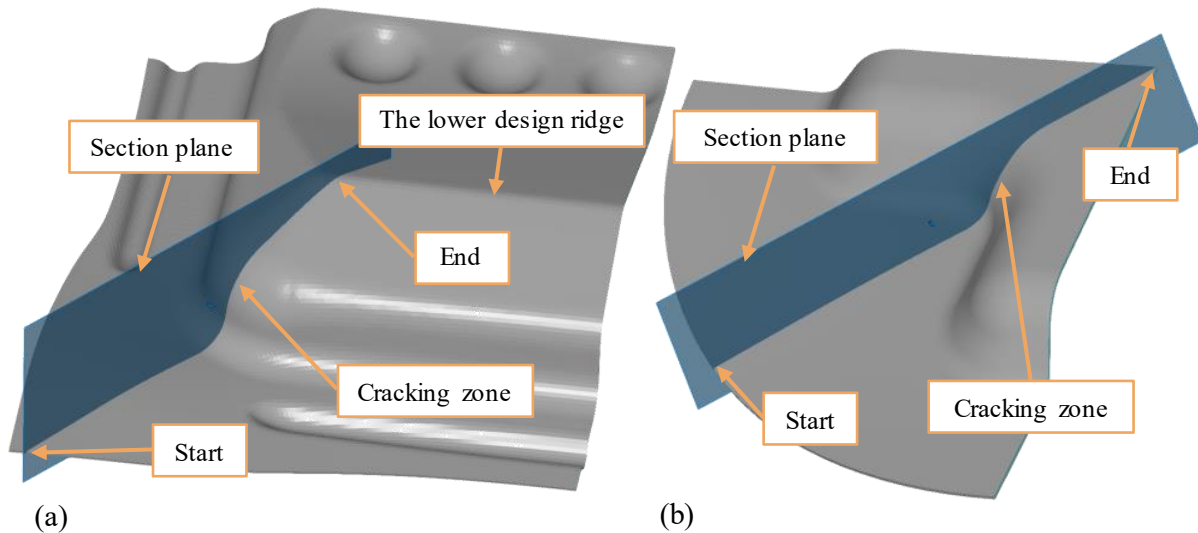


Figure 74 Section planes for the analysis of the thickness change at the components formed using (a) the A-Tool and (b) the CS-Tool

Figure 75 shows the thickness change profiles at the cross-section of the components formed using the A-Tool for blanks (a) AF1, (b) AF2, (c) AF3, and (d) AF4. The thickness change profiles captured by ARGUS were more jagged than the profiles captured by ATOS. Combined capturing the inner and outer surfaces of components was necessary for the thickness evaluation using ATOS. This procedure was more time-consuming than thickness evaluation using ARGUS, but the resulting surface quality was better, and the resulting thickness profiles were smoother. Moreover, the distance between the evaluation points for ARGUS is limited to the distance between the etched dots. This means that only 1 value of thickness change was provided

for about each of 1.5 mm of the section distance. The distance between the evaluation points was not limited for ATOS, so a value of thickness change was evaluated for each 0.3 mm of section length. However, the difference between the two systems was only minor since both systems provided very similar thickness change profiles. A slight thickening of blank material was observed in the flange area for the experimentally formed components reaching a maximum of about 2-3% at the distance along a section of about 55 mm. This was a consequence of tensile-compressive stresses observable in the transition zone from the flange area to the die radius. Furthermore, the blank material was drawn over the die radius, and the thinning of the blank material started due to biaxial tensile stresses. The maximum thinning of about 20% was observed at the distance along a section of about 95 mm for the crack-free formed components. For the cracked component formed using blank AF3, the maximum thinning exceeded the value of 25%. Considering that an additional increase of the BHF would lead to necking or cracking of these components, the maximum allowed thinning of the blank material for the components formed using the A-Tool was 20%. Afterwards, the thickness decreased to about 10% at the lower design ridge.

In general, the numerical forming simulations with the TF and the CF friction models provided good agreement with the experiments. Yet, slight differences between the models were observed and analyzed. The numerical forming simulations predicted slightly lower thickening in the flange area of the components than observed in the experiments. This was probably due to the utilization of shell elements for meshing of blanks since the solid elements are better for the analysis of thickening. The focus of simulations was not on this area since the difference was less than 2% and the slight thinning is not considered a failure. Moreover, similar maximum thinning was obtained by the numerical forming simulations for each of both friction models except for the component formed using blank AF3. The CF model predicted a maximum thinning of about 18% for blank AF3 whereas the TF model predicted a maximum thinning of 24.5%. Evidently, the CF model underestimated notable the maximum thinning, and the TF model provided more accurate results and successfully predicted the excessive thinning of blank material. Moreover, the numerical forming simulations with the TF model predicted slightly higher maximum thinning than the numerical forming simulations with the CF model for the components formed using blanks AF1 and AF2. The maximum thinning predicted by the numerical forming simulation with the TF model agreed better with the experiments for each of these two components. For the component formed using blank AF4, the numerical forming simulation predicted the same maximum thinning using the TF and the CF model, which agreed very well with the experiment. The numerical forming simulation and experiment provided similar thickness changes for distances along sections greater than 100 mm. Thus, utilization of the TF models can be especially important for simulating the critical forming conditions.

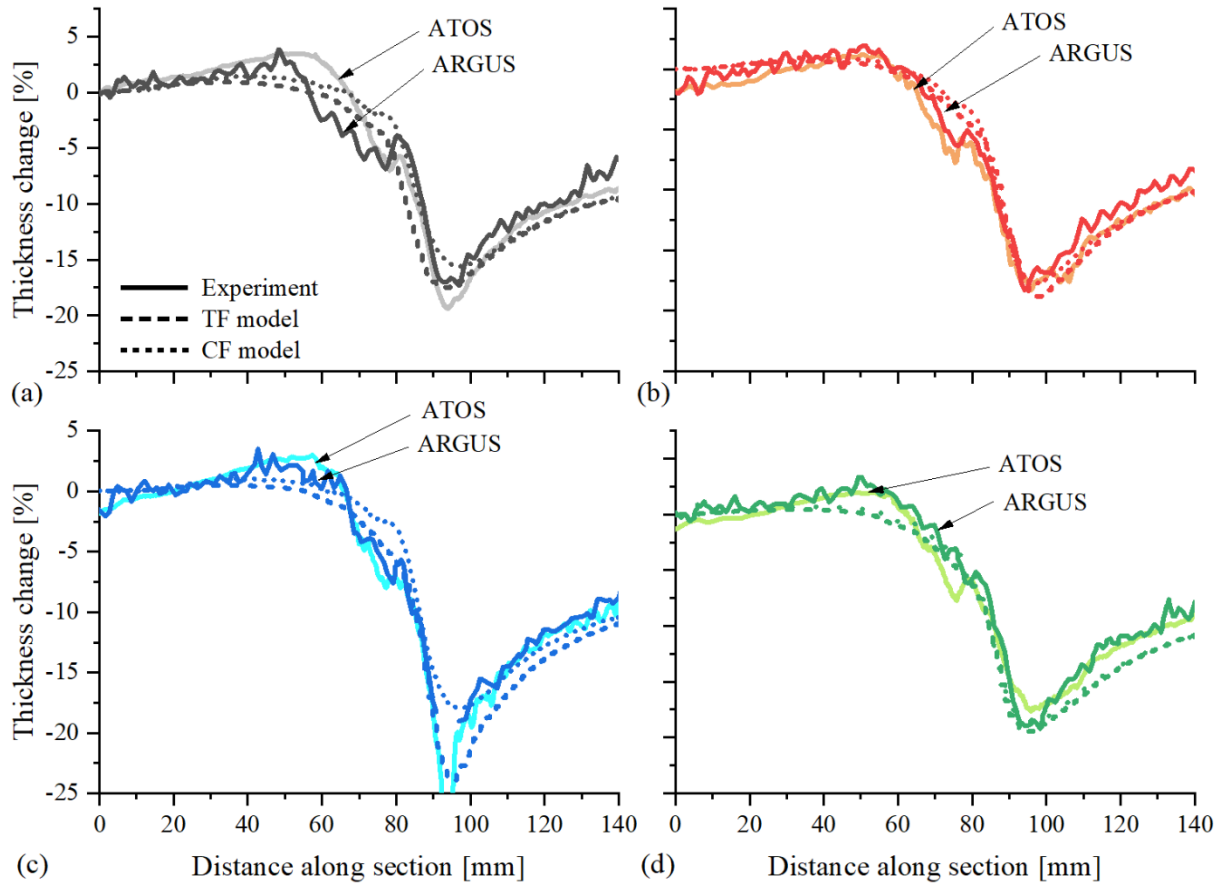


Figure 75 Thickness change at the cross-section of components formed using the A-Tool for blanks (a) AF1 (b) AF2 (c) AF3 and (d) AF4

Figure 76 shows the thickness change profiles at the cross-section of the components formed using the CS-Tool for blanks (a) AF1, (b) AF2, (c) AF3, and (d) AF4. The thickness change profiles of experimentally formed components were captured by ATOS and ARGUS, which again provided similar results. Notable thickening of blank material in the flange area was not observed whether for the experimentally or for the numerically formed components using the CS-Tool. The thinning of blank material started already in the flange area and reached a maximum at the distance along a section of about 80 mm. The maximum thinning was observed in the critical zone, which was close to the die radius as shown in Figure 74 (b). The components formed using blanks AF1 and AF3 had a maximum thinning of about 20%, whereas the components formed using blanks AF2 and AF4 had a maximum thinning of about 25%. Moreover, a necking onset was visible for the components formed using AF2 and AF4 blanks indicating that these components were close to cracking. Thus, the maximum allowed thinning of blank material for avoiding the cracking of components formed using the CS-Tool was 25%. Moreover, the thinning reduced at the further distance along the section, and reached a value of about 0% for the range of 100–140 mm. Thus, it can be concluded that material flow was not observed in the central area of the components formed using the CS-Tool. This is likely due to

the comparatively small punch radius that blocked the material flow. The material flow was eased from the flange area due to the comparatively bigger die radius.

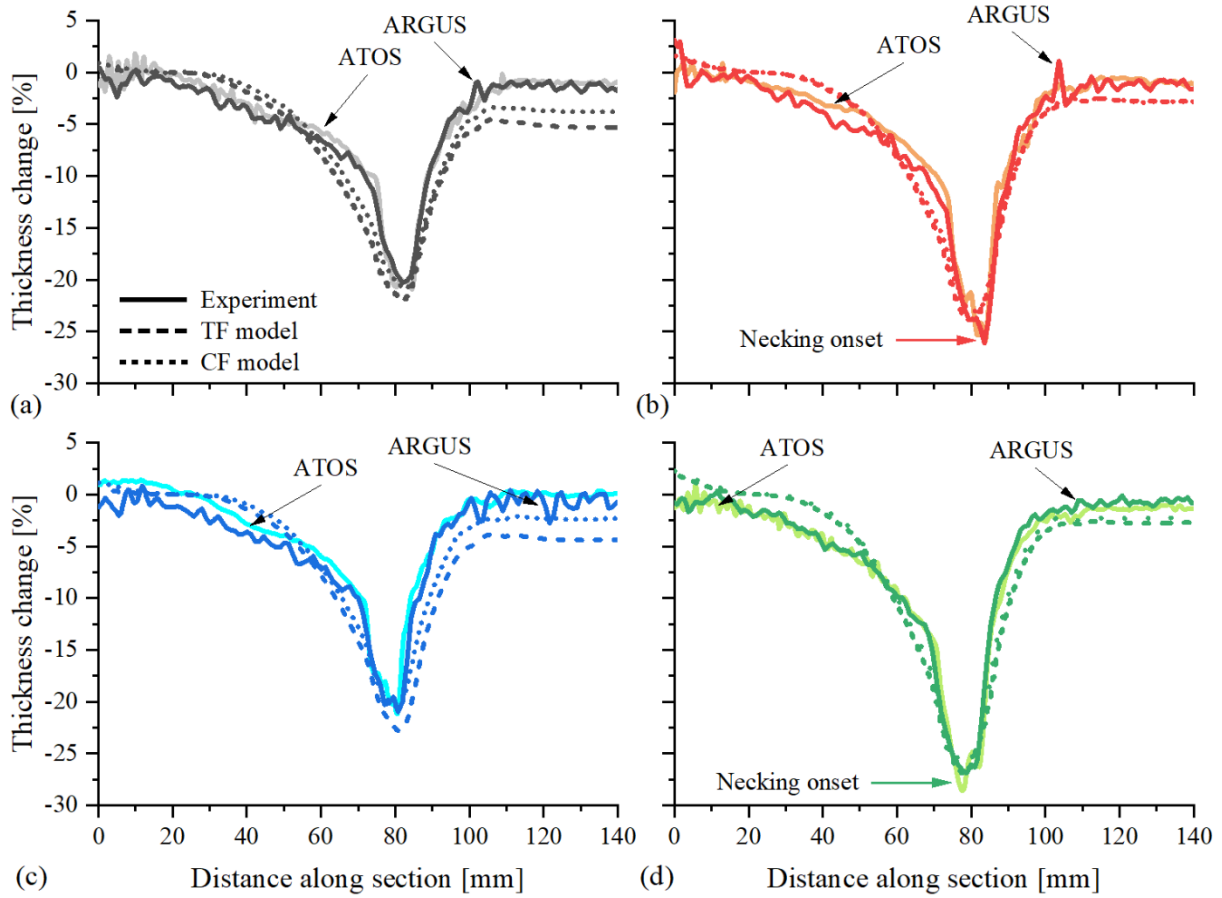


Figure 76 Thickness change at the cross-section of components formed using the A-Tool for blanks (a) AF1 (b) AF2 (c) AF3 and (d) AF4

Prediction of the thickness change by the numerical forming simulation agreed well with the experiments for each of blanks AF1-AF4 formed using the CS-Tool. A minor thickening of the blank material ( $< 2\%$ ) was observed in the numerical forming simulations at the outer edge of the flange area. This was not clearly identified in the experiments due to slight fluctuation of the thickness change profiles. The thickness change profiles were almost identical for the numerical forming simulations with the TF and the CF friction model for the components formed using blanks AF2 and AF4. However, each of the numerical forming simulations almost perfectly predicted the maximum thinning. But, contrary to the experiments, each of the numerical forming simulations predicted thinning of about 3-5% in the central area of the components. The thinning prediction in this area was identical for the components formed using blanks AF2 and AF4, whereas the simulations with the TF model predicted marginally higher thinning than with the CF model for the components formed with blanks AF1 and AF3. The conclusion can be

drawn, that the numerical forming simulations with the TF model did not provide better results than with the CF model for relatively simple tool geometry such as the CS-Tool.

Based on the experimental and numerical thickness change results of the crack-free components, the numerical forming simulations with the TF model showed slightly better results for the complex geometry than with the CF model. However, the prediction of the thinning with the TF model for the cracked component was significantly better than with the CF model. Note that the CoF used in the CF model was retroactively determined for fitting the simulation results. Yet, numerical forming simulations with the CF model can still predict acceptable thickness change results but the TF model can additionally improve these. Moreover, the CoF cannot be retroactively determined during the tool design phase, so the numerical forming simulations are frequently conducted with a standard CoF of about 0.15. Utilization of the TF model in such cases would provide reliable thickness change results at various different forming conditions. Moreover, the critical value of the maximum thinning prior to localized thinning depends on the component geometry.

#### **8.2.4 Surface comparison**

Accurate geometry of numerically formed components is important for several reasons. The main reason for the deviation of component geometry is springback. The highest amount of springback occurs in the flange area but it also can occur in other component areas. Based on the predicted component geometry, cutting tools for the following trimming operation were designed and manufactured. Moreover, accurate prediction of component geometry is necessary for subsequent joining operations in the car assembly procedure. Therefore, the geometries of experimentally and numerically formed components were aligned and the height difference was analyzed.

Figure 77 shows the height difference between the experimentally and the numerically formed components using the A-Tool for blanks (a) AF1 (b) AF2 (c) AF3 and (d) AF4. The upper and lower rows show the comparison between the components from the experiments and the numerical forming simulation with the TF model and with the CF model, respectively. The components from the numerical forming simulation were defined as target bodies and the components from experiments were positioned according to best fit alignment. Therefore, the height difference shown in Figure 77 represents the deviation of the experimentally formed components from the numerically formed components. A positive height difference implies that the component from the experiment is comparatively higher than the component from the numerical forming simulation. Since the digitalized geometry of the components consisted of small triangular, plane elements, the deviation was determined in the normal direction, which is perpendicular to the triangular elements. Generally, the component geometry from the numerical forming simulations agreed well with the experimentally formed components having only minor height deviations. The highest height difference was observed in the corners of the flange area for each of both friction models, with the height difference lower than -1.2 mm. This is mainly due to the relatively simple approach for the release of elastic strains, so the numerical forming simulation predicted a slightly lower springback in this area. Moreover, a difference of about 0.3-0.6 mm was observed in the central area of the components and around the drawbeads. The

numerical forming simulation with the CF model provided slightly better results concerning the deviations in the flange range and the numerical forming simulation with the TF model provided better agreement with the experiments in the central area of components. A deviation of about 1.2 mm was observed around the block beads for blanks AF2–AF4 in the case of the TF model. This is due to the extensive material flow in this area, which significantly affected the geometry around the block beads.

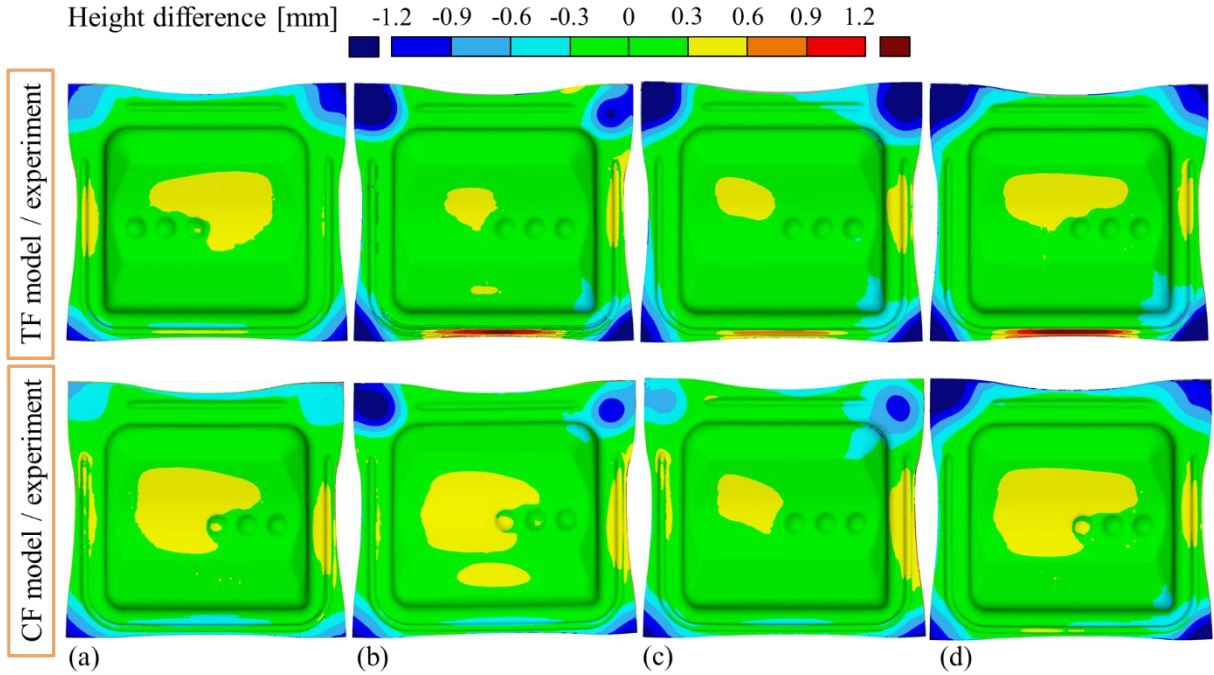


Figure 77 Height different between the experimentally and the numerically formed components using the A-Tool for blanks (a) AF1 (b) AF2 (c) AF3 and (d) AF4

Figure 78 shows the height difference between the components formed using the CS-Tool in the experiment and in the numerical forming simulations (a) with the TF model and (b) with the CF model. Only minor deviations in height difference were observed for this component geometry. The biggest height difference occurred again in the flange area. A height difference of about -1.2 mm was observed in the direction of cross arms whereas a height difference of about 1.2 mm was observed in the flange area between the cross arms. Moreover, only a minor height difference of about 0.3-0.6 mm was observed in the central area of the components. However, each of both friction models provided very similar results and a clear difference between them cannot be distinguished.

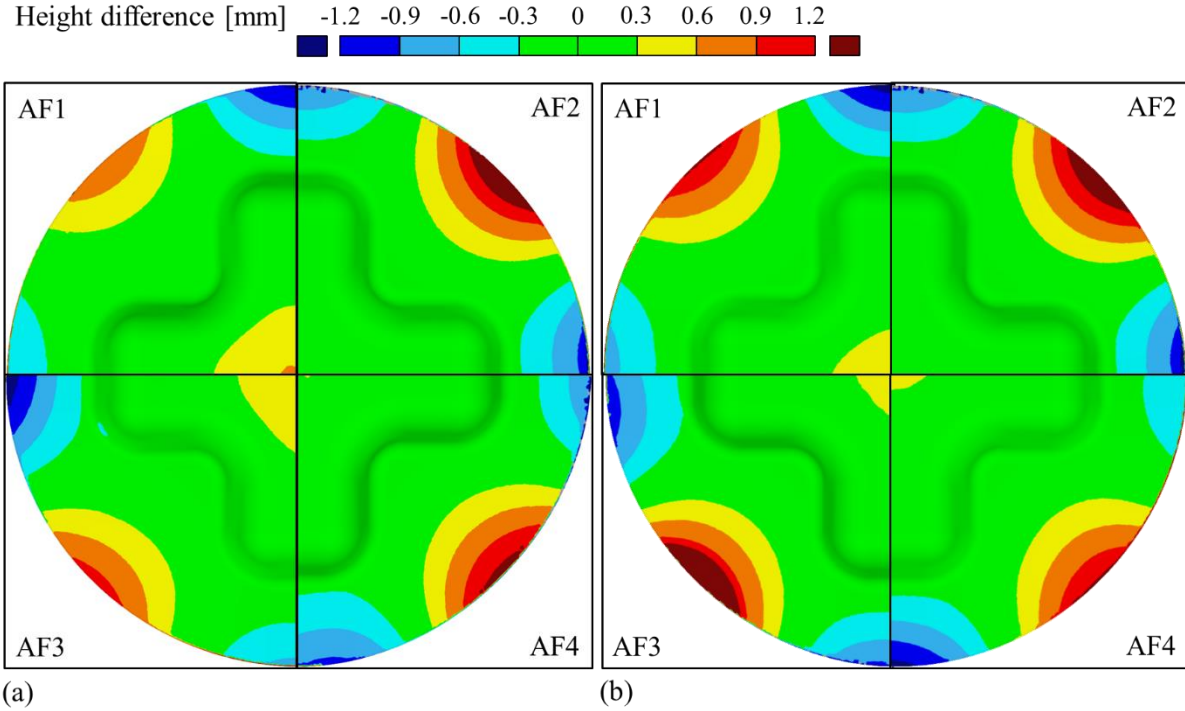


Figure 78 Height difference between the components formed using the CS-Tool in experiment and in numerical forming simulation with (a) the TF model and (b) the CF model

### 8.3 Influence of variable flow curves on the formability of Al-Mg-Si alloys

This section is concerned with the second type of simulation described in section 4.2. The main input parameters for describing the material model in numerical forming simulations are flow curve,  $r$ -values and FLC, as described in section 4.2. Yet,  $r$ -values and FLC of investigated Al-Mg-Si alloy blanks remained relatively stable during the NA but the flow curves changed notably. Moreover, the formability of investigated Al-Mg-Si alloy blanks remained stable during the NA. Thus, the influence of due to NA variable flow curves on the formability of blanks AF3 was numerically investigated. The forming simulations were performed with the TF friction model and a constant blankholder force of 500 kN, which led to the cracking of the components for the entire period of NA. Figure 79 shows numerically obtained FLDs of components formed after (a) 1 month, (b) 2 months (c) 3 months, (d) 6 months (a) 9 months, (b) 12 months, (c) 15 months and (d) 18 months of NA. Notable changes of FLDs were observed for peak 3 and peak 5 whereas the other peaks remained visually unchanged. Strengthening due to NA led to virtually higher flow curves, which decreased the strains in peak 3. Peak 3 exceeded the FLC notably in the forming simulations after 1 month of NA and ended just below the FLC after 18 months of NA. This would lead to the formability enhancement of blanks AF3 during the NA since the cracks occurred because peak 3 exceeded the FLC. However, experimental analysis of formability showed that the formability of blanks AF3 remained constant within 1-18 months of NA. Thus, it is necessary to deeply analyze the factors that may affect the numerical simulations, which consist of three models, i.e., simulation model, material model, and friction model. The simulation model did not change since the geometry of the tool remained unchanged. Experiments showed that  $r$ -values and FLC remained relatively constant during the NA, and

only flow curves were exposed to changes considering the material model. Therefore, the friction model may also be variable during the NA. It is well known that the strength of blanks frequently, as expressed through the hardness, is one of the major impacting factors on the tribology. Therefore, the increase of material strength during the NA likely affected the tribological conditions.

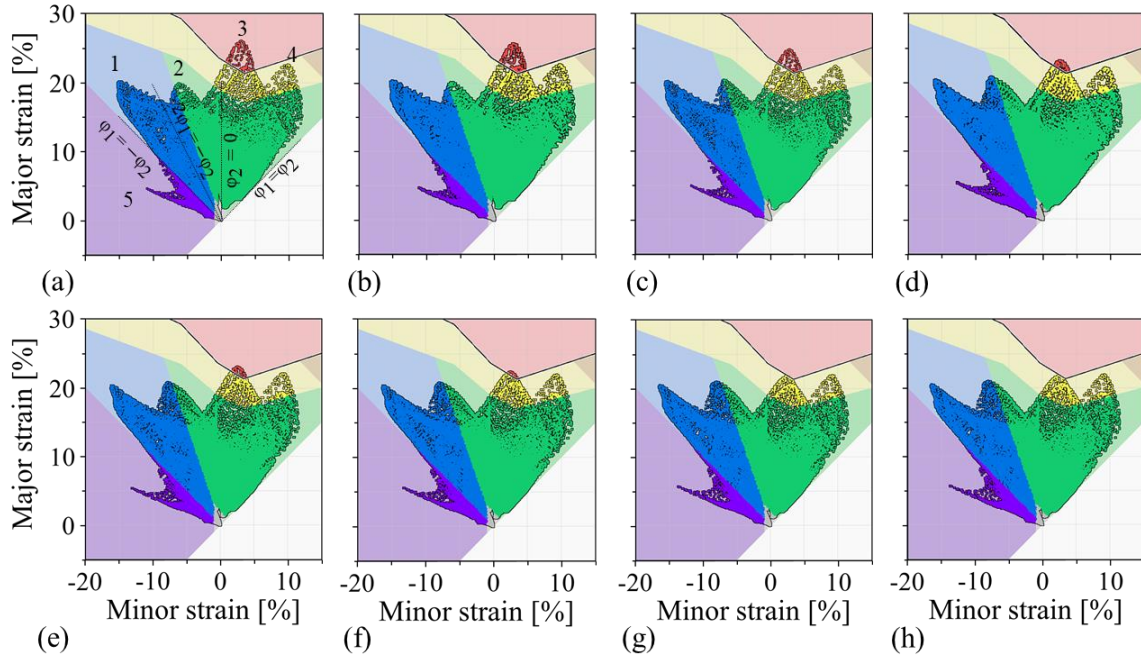


Figure 79 FLD of blanks AF3 formed using the A-Tool, forming velocity of 10 mm/s and BHF of 500 kN after NA of (a) 1 month, (b) 2 months (c) 3 months, (d) 6 months (a) 9 months, (b) 12 months, (c) 15 months and (d) 18 months

The answer may be found in the friction tests conducted for blanks AF1-AF3. These blanks had the same lubricant type, the lubricant amount, and the same roughness. The only difference relevant to the tribology between these blanks was the material strength. Based on the results of pin-on-plate friction tests shown in Chapter 7, tribological conditions were clearly affected by the strength of the blank material. In fact, the highest CoF was observed for the material with the highest strength. Analog to these results, the strengthening of blanks due to NA may also lead to higher CoF. This is likely due to plastic deformation of surface asperities, so higher frictional forces are necessary if the material strength increases. Consequently, this would mean that the friction models of heat-treatable Al-Mg-Si alloys are only valid for a specific period of NA. This means also that friction models should be developed for various stages of NA. In the case of numerically investigated formability of blanks AF3 it can be concluded that the tribology and flow curves were affected by the strengthening. However, the improvement of the formability due to the increasing flow curves was compensated by the worsening of the tribological conditions so the formability remained constant. Yet, additional investigations on this phenomenon are necessary for full understanding.

#### 8.4 Numerical forming simulations at high forming velocity of 100 mm/s

This section is concerned with the third type of simulation described in 4.2. Figure 80 shows numerically determined FLDs for the components formed using the A-Tool and blanks AF1-AF4 at the high forming velocity of 100 mm/s. Note that the applied BHF's were equal to  $F_{\max}$ , so an increase in BHF would lead to failures in the experiments. The strain distribution was similar to the strain distribution of components formed at the low forming velocity of 10 mm/s but with a notably lower peak 3. In general, the cracks occurred at components formed using the A-Tool when the strains of peak 3 exceeded the FLC. Therefore, the FLDs of numerically formed components shown in Figure 80 cannot be classified as critical. The accuracy of the numerical forming simulation at high forming velocity of 100 mm/s was affected by several reasons. The main goal of these simulations was the validation of predicted CoF in the TF models at higher sliding velocities. These tribological conditions were not experimentally investigated, and the data was generated based on the default TriboForm model for Al-Mg-Si alloy blanks. Likely, CoF at higher sliding velocities proposed by the TriboForm friction model was too low, and a critical strain state was not induced. Additional friction tests at higher sliding velocities would be necessary to improve the accuracy of the TF friction models. Moreover, the material model consisted of variable flow curves of constant  $r$ -values and FLC. Higher flow curves at elevated strain rates decreased the strains of peak 3 in the numerical forming simulations. This is similar to the phenomenon observed with variable flow curves due to the NA for blanks AF3 as shown in Figure 79.

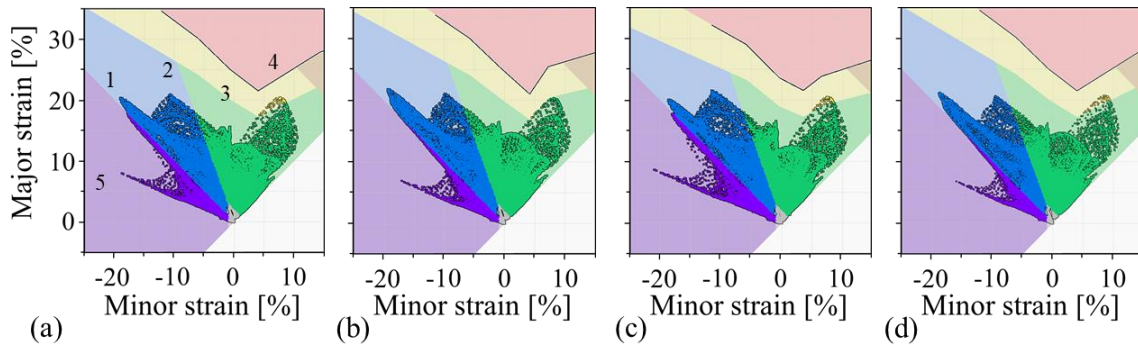


Figure 80 Numerically determined FLD at the forming velocity of 100 mm/s for blanks (a) AF1, (b) AF2, (c) AF3 and (d) AF4

Moreover, Khan and Baig [122] reported that FLC of anisotropic aluminum alloys is affected by the strain rates. The FLC of blanks AF1-AF4 were determined at the quasi-static strain rate. At higher strain rates, a loss of ductility is expected as already shown during the analysis of the formability and of the tensile ductility. This would lead to comparatively lower FLC at higher strain rates and would decrease the gap between the determined strains of peak 3 and the FLC. A negative influence of elevated strain rates on the FLC was also reported elsewhere [89,128,129]. Additionally, elevated strain rates may also affect the  $r$ -values of Al-Mg-Si alloy blanks [121–123]. Considering the variable  $r$ -values in numerical forming simulation would not only require advanced equipment for material testing but also an advanced material model that can implement this effect in numerical forming simulations.

## 9 Conclusions

Experimental and numerical investigations on the formability of 4 Al-Mg-Si alloy blanks named AF1, AF2, AF3, and AF4 were conducted in this work. The influence of NA on the formability and the formability-related material properties was analyzed within 1-18 months. The formability was described using critical blankholder forces for the A-Tool and maximum drawing depth  $D_{\max}$  for the CS-Tool. Moreover, the influence of chemical composition and lubrication on the formability was also investigated. This work also included an in-depth analysis of numerical forming simulations conducted with the constant friction coefficient and with the advanced friction models generated in the TriboForm software. Pin-on-plate frictional tests were conducted for each of the blanks to generate the advanced friction models. Based on the results presented in this work, the following conclusions can be drawn:

1. The strength of Al-Mg-Si alloys blanks can be promoted by increasing Mg and Si content. However, increasing the Mg content and Mg/Si ratio had a higher impact on the strength increase. Yet, the tensile ductility and  $n$ -values of Al-Mg-Si alloy blanks decreased parallel to the strength increase.
2. Increasing of Mg content and Mg/Si ratio enhanced the natural aging kinetics parameter  $k$  of Al-Mg-Si alloys. Moreover, Si content did not influence the natural aging kinetics but rather the initial yield strength  $\sigma_{1h}$  of the blanks.
3. The strengthening of the Al-Mg-Si alloy blanks was due to the clustering of Mg and Si atoms during natural aging. Notable strength increase did not significantly affect the following mechanical material parameters determined using the tensile testing. The tensile ductility and  $r$ -values remained relatively constant whereas  $n$ -values decreased slightly.
4. The formability characterization of Al-Mg-Si alloy blanks using the deep drawing tools was a challenging procedure that required considering various side effects during forming operations. The formability was affected by variable ambient temperature, initial form of blank, surface roughness and lubricant amount.
5. The increase of both Mg and Si content promoted the formability of Al-Mg-Si alloy blanks, but the effect of Si was more significant. However, the effect of lubrication on the formability was even more dominant. The determined formability was related to the planar anisotropy of the blank. A direct relation between the formability and the tensile ductility or  $n$ -values was not found.
6. The formability of Al-Mg-Si alloy blanks decreased after increasing the forming velocity from 10 mm/s to 100 mm/s. This is likely due to the negative effects of higher strain rates on some material properties.
7. The formability of Al-Mg-Si alloy blanks remained constant within 1-18 months of natural aging at each of both forming velocities, i.e., 10 mm/s and 100 mm/s. The formability of the blanks was related to  $r$ -values since both stayed constant during natural aging. Relative stable formability within 1-18 months of natural aging was also an indicator of stable lubricant properties.
8. The bendability of investigated Al-Mg-Si alloy blanks was comparatively similar after 1 month of natural aging for each of blanks AF1-AF3. However, the bendability constantly deteriorates during natural aging. The decrease of  $\alpha_{\max}$  was higher for blanks with faster

- aging kinetics. A relation between the bendability and  $n$ -values was found since both constantly decreased within 1-18 months of natural aging.
9. Despite the notable difference in material strength between the investigated Al-Mg-Si alloy blanks, comparatively similar forming limit strains were observed for each of the blanks. Moreover, the limiting strains were not influenced by natural aging. Despite scattering observed in biaxial tension area of forming limit diagrams, a decrease in limiting strains due to natural aging was neglectable.
  10. The average CoF determined using pin-on-plate tribometer decreased with increasing contact pressure for each of blanks AF1-AF4. However, the average coefficient of friction was about 0.02-0.04 lower for blanks lubricated with PL 39 SX than for blanks lubricated with E 1 Drylube. Moreover, the average coefficient of friction of blanks lubricated with E1 Drylube was also slightly higher for blanks with the highest strength. In general, the average coefficient of friction converged to the value of about 0.10 at high contact pressures for each of blank lubricated with E 1 Drylube.
  11. Numerical forming simulations showed a very good agreement with the experiments for each of both friction models, a constant friction model, and an advanced friction model generated using the TriboForm software. A good agreement was observed in terms of the most important evaluation criteria such as forming limit diagram, thinning, forming force and springback. TriboForm friction model showed slightly better results than the constant friction model for the more complex components formed using the A-Tool whereas the results were similar for the components formed using the CS-Tool.
  12. The coefficients of friction used for the constant friction models were retroactively determined with the aim to achieve the best possible agreement with the experimental results, which is clearly unrealistic when designing deep drawing tools in industrial application. Since numerical forming simulation with the TriboForm friction models provided accurate results for two different types of tools, these models can be applied in numerical forming simulations during the designing phase. This would improve the accuracy of numerical forming simulations, which can be affected by overestimated or underestimated coefficient of friction.
  13. The flow curves evidently changed during NA due to the strengthening of blanks whereas  $r$ -values, the forming limit curves and the formability remained constant. Higher flow curve tended to improve the numerically determined formability of Al-Mg-Si alloy blanks. Thus, frictional models should also be adapted during natural aging since higher material strength may lead to an increase in coefficient of friction.
  14. Conducting the numerical forming simulations at high forming velocity and high strain rates is a complex procedure that needs adequate material and friction modeling. The material model should include information about the dependency of strength, FLC, and  $r$ -values on the strain rates. Moreover, friction tests at high sliding velocities are also necessary.
  15. The formability of Al-Mg-Si alloy blanks remained stable within 1-18 months of NA. Therefore, the typical shelf life of 6 months for these alloy blanks can be extended to periods larger than 6 months. This would eventually reduce the waste material and save recycling costs. However, decreasing bendability during NA might be an issue for eventual hemming operations.

## 10 Outlook

The formability of Al-Mg-Si alloy blanks is a complex material property that can be influenced by various factors. Hence, this topic is surely of interest for some future studies. The author of this work would like to propose some future topics that can be useful for a better understanding of the forming behavior of Al-Mg-Si alloy blanks. The investigated blanks have shown only a minor influence of natural aging on  $r$ -values, which are extremely important for the formability of blanks. On the contrary, Gu et al. [33] reported that  $r$ -values of AA6014 massively decreased within 1-6 months of natural aging. Thus, it would be of utmost interest to analyze the influence of natural aging on formability using an Al-Mg-Si alloy with a similar behavior. This would provide a general overview of changes in the formability of Al-Mg-Si alloys during natural aging. In the scope of these studies, the influence of natural aging on tribological conditions should be investigated. However, it must be separated between the changes of tribological conditions due to the strengthening of blanks and due to the potential deterioration of lubricant properties. Moreover, the influence of elevated strain rates on the mechanical properties of Al-Mg-Si alloy blanks in T4 conditions should be analyzed in detail. The focus of such studies should be on investigating the influence of strain rates ranging from 0.001-10 1/s on the tensile strength, tensile ductility,  $r$ -values,  $n$ -values, FLC and correlating these with the formability. Additionally, frictional tests at elevated sliding velocities should be conducted, so the generated TriboForm friction models can be validated accordingly. Finally, the interaction between the lubricant E 1 Drylube and water additives from the wire eroding machine is to be analyzed.

## 11 References

- [1] J.C. Benedyk. Aluminum alloys for lightweight automotive structures. In *Materials, Design and Manufacturing*. Woodhead Publishing (2010) 79–113.
- [2] F. Ostermann. *Anwendungstechnologie Aluminium*. Springer-Verlag (2015).
- [3] J. Hirsch. Recent development in aluminium for automotive applications. *Transactions of Nonferrous Metals Society of China* 24(7) (2014) 1995–2002.
- [4] G. Pasaoglu, M. Honselaar and C. Thiel. Potential vehicle fleet CO<sub>2</sub> reductions and cost implications for various vehicle technology deployment scenarios in Europe. *Energy Policy* 40 (2012) 404–421.
- [5] W.S. Miller, L. Zhuang, J. Bottema, A.J. Wittebrood, P. De Smet, A. Haszler and A. Vieregge. Recent development in aluminium alloys for the automotive industry. *Materials Science and Engineering A* 280 (2000) 37–49.
- [6] R.S. Long, E. Boettcher and D. Crawford. Current and Future Uses of Aluminum in the Automotive Industry. *JOM* 69(12) (2017) 2635–2639.
- [7] O. Çavuşoğlu, H.I. Sürücü, S. Toros and M. Alkan. Thickness dependent yielding behavior and formability of AA6082-T6 alloy: experimental observation and modeling. *The International Journal of Advanced Manufacturing Technology* 106(9-10) (2020) 4083–4091.
- [8] J. Hirsch. Aluminium in innovative light-weight car design. *Materials transactions. Materials Transactions* 52(5) (2011) 818–824.
- [9] A. Arowosola and G. Gaustad. Estimating increasing diversity and dissipative loss of critical metals in the aluminum automotive sector. *Resources, Conservation and Recycling* 150 (2019) 104382.
- [10] Ducker Research and Consulting. Aluminum Content in Passenger Vehicles (Europe) (2023). [July 03, 2023]; Available from: [https://european-aluminium.eu/wp-content/uploads/2023/05/2023\\_04\\_Aluminum-Content\\_Ducker-Study\\_EA-Public-Summary\\_190423.pdf](https://european-aluminium.eu/wp-content/uploads/2023/05/2023_04_Aluminum-Content_Ducker-Study_EA-Public-Summary_190423.pdf).
- [11] Repairer driven news. <https://www.repairerdrivennews.com/2018/07/13/mixed-material-2019-audi-q8-14-4-hot-formed-steel-has-much-aluminum/>.
- [12] J. Rowe. *Advanced materials in automotive engineering*. Elsevier (2012).
- [13] J.R. Davis. *Alloying: Understanding the Basics*. ASM International (2001) 351–416.
- [14] J.G. Kaufman. *Introduction to aluminum alloys and tempers*. ASM international (2000).
- [15] C. Vargel. *Corrosion of aluminium*. Elsevier (2020).
- [16] A. Birkert, S. Haage and M. Straub. *Umformtechnische Herstellung komplexer Karosserieteile*. Springer Berlin Heidelberg (2013).
- [17] E. Hodžić, J. Domitner, A. Thum, A.S. Sabet, N. Müllner, W. Fragner and C. Sommitsch. Influence of natural aging on the formability of Al-Mg-Si alloy blanks. *Journal of Manufacturing Processes* 94 (2023) 228–239.
- [18] J. Banhart, C.S.T. Chang, Z. Liang, N. Wanderka, M.D.H. Lay and A.J. Hill. Natural Aging in Al-Mg-Si Alloys - A Process of Unexpected Complexity. *Advanced Engineering Materials* 12(7) (2010) 559–571.

- [19] A. Kahrmanidis. Thermisch unterstützte Umformung von Aluminiumblechen. Friedrich-Alexander-Universität Erlangen-Nürnberg (FAU) (2016).
- [20] H.W. Zandbergen, S.J. Andersen and J. Jansen. Structure Determination of Mg<sub>5</sub>Si<sub>6</sub> Particles in Al by Dynamic Electron Diffraction Studies. *Science* 277(5330) (1997) 1221–1225.
- [21] P. Dumitraschkewitz, S.S. Gerstl, L.T. Stephenson, P.J. Uggowitzer and S. Pogatscher. Clustering in Age-Hardenable Aluminum Alloys. *Advanced Engineering Materials* 20(10) (2018) 1800255.
- [22] H. Li and W. Liu. Nanoprecipitates and Their Strengthening Behavior in Al-Mg-Si Alloy During the Aging Process. *Metallurgical and Materials Transactions A* 48(4) 2017 1990–1998.
- [23] K. Matsuda, Y. Sakaguchi, Y. Miyata, Y. Uetani, T. Sato, A. Kamio and S. Ikeno. Precipitation sequence of various kinds of metastable phases in Al-1.0 mass% Mg<sub>2</sub>Si-0.4 mass% Si alloy. *Journal of Materials Science* 35(1) (2000) 179–189.
- [24] I. Polmear. *Light alloys: metallurgy of the light metals*. Butterworth-Heinemann (2017).
- [25] C.H. Shen and B.L. Ou. Effect of Prestraining on the Natural Ageing and Artificial Ageing of an Al-Mg-Si Alloy AA6022. *Canadian Metallurgical Quarterly* 46(1) (2007) 65–74.
- [26] L. Chen, S. Yuan, D. Kong, G. Zhao, Y. He, and C. Zhang. Influence of aging treatment on the microstructure, mechanical properties and anisotropy of hot extruded Al-Mg-Si plate. *Materials & Design* 182 (2019) 107999.
- [27] A. Cuniberti, A. Tolley, M.C. Riglos and R. Giovachini. Influence of natural aging on the precipitation hardening of an AlMgSi alloy. *Materials Science and Engineering A* 527(20) (2010) 5307–5311.
- [28] O. Engler, C.D. Marioara, Y. Aruga, M. Kozuka and O. Myhr. Effect of natural ageing or pre-ageing on the evolution of precipitate structure and strength during age hardening of Al–Mg–Si alloy AA 6016. *Materials Science and Engineering A* 759 (2019) 520–529.
- [29] S. Esmaeili, X. Wang, D.J. Lloyd and W.J. Poole. On the precipitation-hardening behavior of the Al–Mg–Si–Cu alloy AA6111. *Metallurgical and Materials Transactions A* 34(13) (2003) 751–763.
- [30] S. Esmaeili and D.J. Lloyd. Effect of composition on clustering reactions in AlMgSi (Cu) alloys. *Scripta Materialia* 50(1) (2004) 155–158.
- [31] P.A. Friedman and S.G. Luckey. Failure of Al-Mg-Si alloys in bending. *Practical Failure Analysis* 2(1) (2002) 33–42.
- [32] G.J. Gao, Y. Li, Z.D. Wang, R.D.K. Misra, H.S. Di, J.D. Li, and G.M. Xu. Interaction Between Natural Aging and Pre-Aging Processes and its Impact on the Age-Hardening Behavior of Al-Mg-Si Automotive Sheets. *JOM* 71(12) (2019) 4405–4413.
- [33] Z. Gu, G. Wang and G. Yu. Investigation on Fracture of a 6014-T4 Aluminum Alloy Sheet in the Flanging and Hemming Process Based on Numerical and Experimental Methods. *Metals* 10(1) (2020) 81.
- [34] S.M. Hirth, G.J. Marshall, S.A. Court and D.J. Lloyd. Effects of Si on the aging behaviour and formability of aluminium alloys based on AA6016. *Materials Science and Engineering A* 319 (2001) 452–456.

- [35] Z. Jia, L. Ding, L. Cao, R. Sanders, S. Li and Q. Liu. The Influence of Composition on the Clustering and Precipitation Behavior of Al-Mg-Si-Cu Alloys. *Metallurgical and Materials Transactions A* 48(1) (2017) 459–473.
- [36] A. Klos, S. Kellner, D. Wortberg, P. Walter, C. Bassi and M. Merklein. Forming characteristics of artificial aging Al-Mg-Si-Cu sheet alloys. *AIP Conference Proceedings* 1896(1) (2017) 020020.
- [37] H. Laurent, V.M. Simões, M.C. Oliveira and L.F. Menezes. The influence of warm forming conditions on the natural aging and springback of a 6016-T4 aluminum alloy. *IOP Conference Series: Materials Science and Engineering* 418(1) (2018) 012020.
- [38] B. Mirzakhani and Y. Payandeh. Combination of sever plastic deformation and precipitation hardening processes affecting the mechanical properties in Al–Mg–Si alloy. *Materials & Design* 68 (2015) 127–133.
- [39] T. Ogura, A. Hirose and T. Sato. Effects of Pre-Aging on Bendability of an Asymmetric-Rolled Al-Mg-Si Alloy. In *Materials Science Forum* 706-709 (2012) 377–382. Trans Tech Publications Ltd.
- [40] F. Ozturk, E. Esener, S. Toros and C.R. Picu. Effects of aging parameters on formability of 6061-O alloy. *Materials & Design* 31(10) (2010) 4847–4852.
- [41] F. Ozturk, A. Sisman, S., Toros, S. Kilic and R.C. Picu. Influence of aging treatment on mechanical properties of 6061 aluminum alloy. *Materials & Design* 31(2) (2010) 972–975.
- [42] A. Poznak, V. Thole and P. Sanders. The Natural Aging Effect on Hardenability in Al-Mg-Si: A Complex Interaction between Composition and Heat Treatment Parameters. *Metals* 8(5) (2018) 309.
- [43] R. Prillhofer, G. Rank, J. Berneder, H. Antrekowitsch, P.J. Uggowitzer and S. Pogatscher. Property Criteria for Automotive Al-Mg-Si Sheet Alloys. *Materials* 7(7) (2014) 5047–5068.
- [44] X. Ren, Y. Huang and Y. Li. Effect of Prestraining and Preaging on Properties of Al-Mg-Si Alloys Before and After Plane Baking. *Journal of Materials Engineering and Performance* 28(7) (2019) 4496–4501.
- [45] J. Røyset, T. Stene, J.A. Sæter and O. Reiso. The Effect of Intermediate Storage Temperature and Time on the Age Hardening Response of Al-Mg-Si Alloys. *Materials Science Forum* 519-521 (2006) 239–244.
- [46] D.J. Lloyd. The scaling of the tensile ductile fracture strain with yield strength in Al alloys. *Scripta Materialia* 28(4) 2003 341–344.
- [47] V.M. Simões, H. Laurent, M.C. Oliveira and L.F. Menezes. Natural aging effect on the forming behavior of a cylindrical cup with an Al-Mg-Si alloy. *AIP Conference Proceedings* 1769(1) (2016) 200021.
- [48] V. Simões, H. Laurent, M. Oliveira and L. Menezes. The influence of warm forming in natural aging and springback of Al-Mg-Si alloys. *International Journal of Material Forming* 12(1) (2019) 57–68.
- [49] N. Tian, G. Zhao, L. Zuo and C.M. Liu. Formability and Correlation between Formability Indices of Al-0.9Mg-1.0Si-0.7Cu-0.6Mn Alloy for Automotive Body Sheets. *Materials Science Forum* 638-642 (2010) 356–361.
- [50] Y. Weng, Z. Jia, L. Ding, Y. Pan, Y. Liu and Q. Liu. Effect of Ag and Cu additions on natural aging and precipitation hardening behavior in Al-Mg-Si alloys. *Journal of Alloys and Compounds* 695 (2017) 2444–2452.

- [51] M. Werinos, H. Antrekowitsch, W. Fragner, T. Ebner, P.J. Uggowitzer and S. Pogatscher. Influence of Temperature on Natural Aging Kinetics of AA6061 Modified with Sn. In *Light Metals 2015* (2015) 367-371.
- [52] L. Zhen and S.B. Kang. Deformation and fracture behavior of two Al-Mg-Si alloys. *Metallurgical and Materials Transactions A* 28(7) (1997) 1489–1497.
- [53] H. Zhong, P. Rometsch, L. Cao, F. Guo and B. Muddle. Tensile properties and work hardening behaviour of alloy 6016 in naturally aged and pre-aged conditions. In *Proceedings of the 12th international conference on aluminum alloys* (2010) 2203-2208.
- [54] R.A. Yildiz and S. Yilmaz. Influence of heat treatments on the formability of the 6061 Al alloy sheets: experiments and GTN damage model. *The International Journal of Advanced Manufacturing Technology* 113(7-8) (2021) 2277–2299.
- [55] Z. Gu, Y. Han, Z. Tang, L. Yi and G. Yu. Quantitative Research on the Effect of Natural Aging on the Mechanical Properties and Bake Hardening Properties of AA6014 Alloy within Six Months. *Metals* 11(4) (2021) 673.
- [56] A.R. Loukus, G. Subhash and M. Imaninejad. Optimization of material properties and process parameters for tube hydroforming of aluminum extrusions. *Journal of Engineering Materials and Technology* 129(2) (2007) 233-241.
- [57] Y. Birol. Pre-aging to improve bake hardening in a twin-roll cast Al–Mg–Si alloy. *Materials Science and Engineering: A* 391(1-2) (2005) 175–180.
- [58] H. Zhong, P.A. Rometsch, L. Cao and Y. Estrin. The influence of Mg/Si ratio and Cu content on the stretch formability of 6xxx aluminium alloys. *Materials Science and Engineering A* 651 (2016) 688-697.
- [59] M.S. Remøe, K. Marthinsen, I. Westermann, K. Pedersen, J. Røyset and C. Marioara. The effect of alloying elements on the ductility of Al-Mg-Si alloys. *Materials Science & Engineering A* 693 (2017) 60–72.
- [60] J.E. Hockett and O.D. Sherby. Large strain deformation of polycrystalline metals at low homologous temperatures. *Journal of the Mechanics and Physics of Solids* 23(2) (1975) 87-98.
- [61] H.W. Swift. Plastic instability under plane stress. *Journal of the Mechanics and Physics of Solids* 1(1) (1952) 1-18.
- [62] K. Siegert. *Blechumformung*. Springer Berlin Heidelberg (2015).
- [63] E. Hodžić, J. Domitner, A. Thum, A. Shafiee Sabet, N. Müllner, W. Fragner and C. Sommitsch. Influence of alloy composition and lubrication on the formability of Al-Mg-Si alloy blanks. *Journal of Manufacturing Processes* 85 (2023) 109-121.
- [64] N. Herzig, A.M. Shawky and L.W. Meyer. Experimentelle Ermittlung und Modellierung dynamischer Fließortkurven an Blechwerkstoffen. In *Proceedings of the 9th LS-DYNA forum, Bamberg, Germany* (2010) 12-13.
- [65] Y. Koshino, Y. Aruga, J. Mukai and K. Kaneko. Relationship among elongation and work hardening behavior and dislocation characteristics of Al–Mg–Si series alloys. *Journal of Japan Institute of Light Metals* 68(4) (2018) 201-205.
- [66] E. Doege and T. Hallfeld. Metal working: stretching of sheets. *Encyclopedia of Materials: Science and Technology* (2001) 5518-5521.

- [67] Zwick Roell. Berechnung des n-Werts gemäß ISO 10275 und ASTM E646. [July 05, 2023]; Available from: <https://www.zwickroell.com/de/branchen/werkstoffpruefung-materialpruefung/n-wert-berechnung-nach-iso-10275/#c75763>.
- [68] D.K. Leu. A simplified approach for evaluating bendability and springback in plastic bending of anisotropic sheet metals. *Journal of Materials Processing Technology* 66(1-3) (1997) 9-17.
- [69] X. Wang, M. Guo, J. Luo, C. Xie, Y. Wang, J. Zhang and L. Zhuang. Effect of intermediate annealing time on microstructure, texture and mechanical properties of Al-Mg-Si-Cu alloy. *Materials Characterization* 142 (2018) 309-320.
- [70] F. Barlat and K. Lian. Plastic behavior and stretchability of sheet metals. Part I: A yield function for orthotropic sheets under plane stress conditions. *International Journal of Plasticity* 5(1) (1989) 51-66.
- [71] D. Banabic, H. Aretz, D.S. Comsa and L. Paraianu. An improved analytical description of orthotropy in metallic sheets. *International Journal of Plasticity* 21(3) (2005) 493–512.
- [72] E. Doege and B.A. Behrens. *Handbuch Umformtechnik*. Springer Berlin Heidelberg (2016).
- [73] M. Lenzen and M. Merklein. Improvement of Numerical Modelling Considering Plane Strain Material Characterization with an Elliptic Hydraulic Bulge Test. *Journal of Manufacturing and Materials Processing* 2(1) (2018) 6.
- [74] O. Engler, C. Schäfer and O.R. Myhr. Effect of natural ageing and pre-straining on strength and anisotropy in aluminium alloy AA 6016. *Materials Science and Engineering: A* 639 (2015) 65-74.
- [75] M.B. Gorji and D. Mohr. Predicting shear fracture of aluminum 6016-T4 during deep drawing: Combining Yld-2000 plasticity with Hosford–Coulomb fracture model. *International Journal of Mechanical Sciences* 137 (2018) 105-120.
- [76] A. Rosiak, L.L. Costa, A.M.G. Brito and L. Schaeffer. Determination of Flow Curves by Stack Compression Tests of 22MnB5 Sheets. *American Journal of Materials Science* 9(2) (2019) 29-35.
- [77] L. M. Alves, C.V. Nielsen and P. A. F. Martins. Revisiting the Fundamentals and Capabilities of the Stack Compression Test. *Experimental Mechanics* 51(9) (2011) 1565–157.
- [78] M. Merklein and A. Kuppert. A method for the layer compression test considering the anisotropic material behavior. *International Journal of Material Forming* 2 (2009) 483–486.
- [79] W.F. Hosford and R.M. Caddell. *METAL FORMING: Mechanics and Metallurgy*. Cambridge university press (2011).
- [80] B. Hochholdiger, H. Grass, A. Lipp and P. Hora. Determination of flow curves by stack compression tests and inverse analysis for the simulation of hot forming. 7th European LS-DYNA conference (2009).
- [81] M. Liewald. Deep Drawing (2017). In: P. Laperrière et al. (Ed.) *CIRP Encyclopedia of Production Engineering*. Springer Berlin Heidelberg.
- [82] S. Yuan, W. Cheng, W. Liu and Y. Xu. A novel deep drawing process for aluminum alloy sheets at cryogenic temperatures. *Journal of Materials Processing Technology* 284 (2020) 116743.
- [83] J. Dietrich. *Praxis der Umformtechnik*. Springer Fachmedien Wiesbaden (2018).
- [84] H.E. Friedrich. *Leichtbau in der Fahrzeugtechnik*. Springer Fachmedien Wiesbaden (2017).

- [85] M. Gensamer. Strength and ductility. Transactions of the American Society for Metals 36 (1946) 30–60.
- [86] S.P. Keeler. Plastic instability and fracture in sheet stretched over rigid punches (1961), PhD Thesis, Massachusetts Institute of Technology, Boston.
- [87] G.M. Goodwin. Application of strain analysis to sheet metal forming problems in the press shop. Society of Automotive Engineers No. 680093 (1968) 380–387.
- [88] D. Banabic. Sheet Metal Forming Processes. Springer Berlin Heidelberg (2010).
- [89] S.K. Paul. Controlling factors of forming limit curve: A review. Advances in Industrial and Manufacturing Engineering 2 (2021) 100033.
- [90] K. Nakazima and T. Kikuma. Forming limits under biaxial stretching of sheet metals. Testu-to Hagane 53 (1967) 455–458 (in Japanese).
- [91] K. Nakazima, T. Kikuma and K. Hasuka. Study on the formability of steel sheets. Yawata Technical Report 284 (1971) 678–680.
- [92] W. Muhammad, U. Ali, A.P. Brahme, J. Kang, R.K. Mishra and K. Inal. Experimental analyses and numerical modeling of texture evolution and the development of surface roughness during bending of an extruded aluminum alloy using a multiscale modeling framework. International Journal of Plasticity 117 (2019) 93–121.
- [93] Z. Fan, X. Lei, L. Wang, X. Yang and R.E. Sanders. Influence of quenching rate and aging on bendability of AA6016 sheet. Materials Science and Engineering: A 730 (2018) 317–327.
- [94] A. Davidkov, R.H. Petrov, P de Smet, B. Schepers and L.A.I. Kestens. Microstructure controlled bending response in AA6016 Al alloys. Materials Science and Engineering: A 528(22-23) (2011) 7068–7076.
- [95] F. Bauer. Tribologie. Springer Fachmedien Wiesbaden (2021).
- [96] G. Li, X. Long, P. Yang and Z. Liang. Advance on friction of stamping forming. The International Journal of Advanced Manufacturing Technology 96(1-4) (2018) 21-38.
- [97] Q.J. Wang and Y.W. Chung. Encyclopedia of Tribology. Springer New York Heidelberg Dordrecht London (2013).
- [98] M. Hamel, A. Addali and D. Mba. Employing Acoustic Emission for Monitoring Oil Film Regimes. Lubricants 1(3) (2013) 61–74.
- [99] E. Hodžić, A. Shafiee Sabet, Z. Silvayeh, P. Auer, A. Drexler, C. Sommitsch and J. Domitner. Influence of elevated surface temperature on the formability in cold forming of aluminum alloy sheets. IOP Conference Series: Materials Science and Engineering 1284 (2023) 012032.
- [100] T. Trzepieciniski and H.G. Lemu. Recent Developments and Trends in the Friction Testing for Conventional Sheet Metal Forming and Incremental Sheet Forming. Metals 10(1) (2020) 47.
- [101] A. Shafiee Sabet, J. Domitner, K.I. Öksüz, E. Hodžić, H. Torres, M. Rodríguez Ripoll and C. Sommitsch. Tribological investigations on aluminum alloys at different contact conditions for simulation of deep drawing processes. Journal of Manufacturing Processes 68 (2021) 546-557.
- [102] E.S. de Argandoña, A. Zabala, L. Galdos and J. Mendiguren. The Effect of Material Surface Roughness in Aluminum Forming. Procedia Manufacturing 47 (2020) 591-595.

- [103] M. Ruiz-Andrés, A. Conde, J. de Damborenea and I. García. Wear Behavior of Aluminum Alloys at Slow Sliding Speeds. *Tribology Transactions* 58(5) (2015) 955–962.
- [104] R. Zhou, J. Cao, Q. J. Wang, F. Meng, K. Zimowski and Z.C. Xia. Effect of EDT surface texturing on tribological behavior of aluminum sheet. *Journal of Materials Processing Technology* 211(10) (2011) 1643–1649.
- [105] R. Schneider, R.J. Grant, J.M. Schlosser W. Rimkus, K. Radlmayr, F. Grabner and C.H. Maier. An Investigation of the Deep Drawing Behavior of Automotive Aluminum Alloys at Very Low Temperatures. *Metallurgical and Materials Transactions A* 51(3) 2020 1123–1133.
- [106] Z. Deng and R. Hennig. Influence of material modeling on simulation accuracy of aluminum stampings. *Journal of Physics: Conference Series* 896 (2017) 012025.
- [107] M. Werinos, H. Antrekowitsch, T. Ebner, R. Prillhofer P.J. Uggowitzer and S. Pogatscher. Hardening of Al–Mg–Si alloys: Effect of trace elements and prolonged natural aging. *Materials & Design* 107 (2016) 257–268.
- [108] M. Kasemer, G. Falkinger and F. Roters. A numerical study of the influence of crystal plasticity modeling parameters on the plastic anisotropy of rolled aluminum sheet. *Modelling and Simulation in Materials Science and Engineering* 28(8) (2020) 085005.
- [109] A. Klos, A. Kahrmanidis, D. Wortberg and M. Merklein. Experimental and Numerical Studies on the Forming Behavior of High Strain Al-Mg-Si(-Cu) Sheet Alloys. *Procedia Engineering* 183 (2017) 95–100.
- [110] H. Laurent, J. Coër, P.Y. Manach, M.C. Oliveira and L.F. Menezes. Experimental and numerical studies on the warm deep drawing of an Al–Mg alloy. *International Journal of Mechanical Sciences* 93 (2015) 59–72.
- [111] W.A. Monteiro. Light metal alloys applications. *BoD–Books on Demand* (2014).
- [112] D. Li and A. Ghosh. Tensile deformation behavior of aluminum alloys at warm forming temperatures. *Materials Science and Engineering: A* 352(1-2) (2003) 279–286.
- [113] V. Simoes, H. Laurent, M. Oliveira and L. Menezes. Influence of temperature, strain-rate and aging on the mechanical behaviour of an Al-Mg-Si alloy. *CFM 2015-22ème Congrès Français de Mécanique. AFM, Maison de la Mécanique, 39/41 rue Louis Blanc-92400 Courbevoie* (2015).
- [114] M. Kumar, N. Sotirov, F. Grabner, R. Schneider and G. Mozdzen. Cryogenic forming behaviour of AW-6016-T4 sheet. *Transactions of Nonferrous Metals Society of China* 27(6) (2017) 1257–1263.
- [115] S. Li, L. Li, H. He and G. Wang. Influence of the deformation heating on the flow behavior of 6063 alloy during compression at medium strain rates. *Journal of Materials Research* 34(2) (2019) 309–320.
- [116] J. Bottema, C. Lahaye, R. Baartman, L. Zhuang, P. de Smet and F. Schoepen. Recent Developments in AA6016 Aluminium Type Body Sheet Product. *SAE transactions* (1998) 900–907.
- [117] H. Zhong, P.A. Rometsch and Y. Estrin. The Influence of Si and Mg Content on the Microstructure, Tensile Ductility, and Stretch Formability of 6xxx Alloys. *Metallurgical and Materials Transactions A* 44(8) (2013) 3970–3983.
- [118] S. J. Murtha. New 6XXX Aluminum Alloy for Automotive Body Sheet Applications. *SAE transactions* (1995) 657–666.

- [119] J. Hirsch. Aluminium Alloys for Automotive Application. *Materials Science Forum* 242 (1997) 33-50.
- [120] J. Domitner, Z. Silvayeh, A. Shafiee Sabet, K.I. Öksüz, L. Pelcastre and J. Hardell, J. Characterization of wear and friction between tool steel and aluminum alloys in sheet forming at room temperature. *Journal of Manufacturing Processes* 64 (2021) 774–784.
- [121] T. Rahmaan, J. Noder, A. Abedini, P. Zhou, C. Butcher and M. J. Worswick. Anisotropic plasticity characterization of 6000- and 7000-series aluminum sheet alloys at various strain rates. *International Journal of Impact Engineering* 135 (2020) 103390.
- [122] A.S. Khan and M. Baig. Anisotropic responses, constitutive modeling and the effects of strain-rate and temperature on the formability of an aluminum alloy. *International Journal of Plasticity* 27(4) (2011) 522-538.
- [123] O. Majidi, M. Jahazi and N. Bombardier. Characterization of mechanical properties and formability of a superplastic Al-Mg alloy. *Journal of Physics: Conference Series* 1063 (2018) 012165.
- [124] A.R. Loukus, G. Subhash and M. Imaninejad. Optimization of Material Properties and Process Parameters for Tube Hydroforming of Aluminum Extrusions. *Journal of Engineering Materials and Technology* 129(2) 2007 233–241.
- [125] C. Zhang, L. Leotoing, D. Guines and E. Ragneau. Theoretical and numerical study of strain rate sensitivity on formability of sheet metal. *Numisheet 2008* (2008) 1-5.
- [126] J. Sidor, R.H. Petrov and L.A.I. Kestens. Deformation, recrystallization and plastic anisotropy of asymmetrically rolled aluminum sheets. *Materials Science and Engineering: A* 528(1) (2010) 413–424.
- [127] A.R. Ragab and Ch. A. Saleh. Evaluation of bendability of sheet metals using void coalescence models. *Materials Science and Engineering: A* 395 (1-2) 2005 102–109.
- [128] W. Xiao W, B. Wang and K. Zheng. An experimental and numerical investigation on the formability of AA7075 sheet in hot stamping condition. *The International Journal of Advanced Manufacturing Technology* 92(9-12) (2017) 3299–3309.
- [129] Z. Shi, Y. Wang, J. Lin, T. Dean, D. Balint, M. Stanton and D. Watson. An Investigation, Using Standard Experimental Techniques, to Determine FLCs at Elevated Temperature for Aluminium Alloys. *Proceedings of the 3rd International Conference on New Forming Technology* (2012).

## List of figures

Figure 1 Average aluminum content for European passenger cars [10] .....	1
Figure 2 An example of successful implementation of aluminum components in passenger car design [11] .....	2
Figure 3 A comparison between 4 commercial aluminum alloy blanks used for production of car outer panels [3] .....	8
Figure 4 Schematic illustration of processing of Al-Mg-Si alloy blanks in production of car outer panels [17] .....	9
Figure 5 Phase sequences observable at different stages of precipitation hardening of Al-Mg-Si alloys [18] .....	10
Figure 6 Schematic illustration of a flat sample for uniaxial tensile testing in (a) initial and (b) fractured state .....	12
Figure 7 Stress-strain curves obtained by uniaxial tensile testing .....	13
Figure 8 Determination of $n$ -values using stresses and strains from flow curve (adapted from [67]) .....	14
Figure 9 Determination of $r$ -values using the samples for uniaxial tensile test (adapted from [16]) .....	15
Figure 10 Illustration of loads and stress states necessary for experimental determination of yield surface (adapted from [64]) .....	16
Figure 11 Flow curves obtained by the tensile test and by the stack compression test [64] .....	17
Figure 12 Basic steps in deep drawing procedure and the main parts of a deep drawing tool and [16] .....	19
Figure 13 (a) A cup-shaped tool as an basic example of deep drawing and (b) deformation zones of deep-drawn component [81] .....	20
Figure 14 Deformation zones of deep-drawn components and corresponding strain states [84] .....	21
Figure 15 The most common types of failure related to deep drawing [84] .....	23
Figure 16 Process window for production of wrinkle- and crack-free components [16] .....	24
Figure 17 Schematic illustration of a forming limit curve and characteristic strain states .....	25
Figure 18 (a) Schematic illustration of Nakazima samples and (b) set of 7 formed samples with different geometry for determination of forming limit curve [88] .....	26
Figure 19 Bonding of outer and inner panels through hemming in 3 steps: (a) flanging, (b) pre-hemming and (c) hemming [33] .....	26
Figure 20 Plate bending test according to VDA 238-100 .....	27
Figure 21 Lubrication regimes and Stribeck curve (adapted from [97,98] ) .....	29
Figure 22 Tribological system observable for mixed lubrication regime in a deep drawing operation (adapted from [2]) .....	31
Figure 23 Tribological zones in deep drawing operation (adapted from [2]) .....	32
Figure 24 Schematic illustration of the measurement points for the analysis of surface roughness and lubricant amount .....	33
Figure 25 (a) Tensile test samples with respect to rolling direction and (b) Tensile testing setup .....	34
Figure 26 Stack compression tests (a) at the first contact and (b) at the end of the test .....	35

Figure 27 Plate bending test fixture with an Al-Mg-Si alloy plate at the (a) start and (b) end of the test.....	36
Figure 28 (a) Illustration of setup for the Nakajima test and (b) sample geometries (adapted from [75]) .....	37
Figure 29 (a) A-Tool, (b) Blank component formed with the A-Tool and (c) formability characterization using the A-Tool .....	39
Figure 30 (a) Cross-shaped tool (CS-Tool), (b) component formed with the CS-Tool and (c) determination of maximum drawing depth with the CS-Tool.....	40
Figure 31 3D optical scanning of the components using (a) ARGUS and (b) ATOS.....	41
Figure 32 (a) Test setup for pin-on-plate tribometer and (b) geometry of the steel pin.....	42
Figure 33 Simulation models of active tool parts for (a) the A-Tool and (b) the CS-Tool.....	44
Figure 34 (a) Flow curves and (b) FLC determined after 3 months of NA.....	45
Figure 35 3 mandatory steps in generation and implementation of the TriboForm friction model .....	46
Figure 36 EDT surface of investigated blanks in (a) dry and (b) lubricated condition; (c) surface topography of the tool with MF texture .....	47
Figure 37 (a) NA influence on the yield strength of blanks AF1-AF3 and (b) logarithmic increase of yield strength in RD .....	48
Figure 38 The influence of NA on the ultimate tensile strength for blanks AF1-AF3 .....	50
Figure 39 Influence of NA on the uniform strains of blanks (a) AF1, (b) AF2 and (c) AF3.....	51
Figure 40 Influence of NA on fracture strain of (a) AF1, (b) AF2 and (c) AF3 blanks.....	52
Figure 41 Effect of surface defects observed at tensile test samples after the wire eroding on the fracture pattern .....	52
Figure 42 Post-uniform strain of AF1-AF3 blanks measured in (a) RD, (b) DD and (c) TD.....	53
Figure 43 Strain hardening capacity during the tensile test of blanks AF1-AF3 .....	54
Figure 44 Influence of NA on $n$ -values of blanks AF1-AF3 in RD, DD and TD.....	55
Figure 45 Influence of NA on $r$ -values of blanks AF1-AF3 .....	56
Figure 46 Influence of NA on the average normal anisotropy $r_m$ and the planar anisotropy $\Delta r$ of blanks AF1-AF3 .....	57
Figure 47 Strengthening as function of the true plastic strain (flow curve) for blanks (a) AF1, (b) AF2 and (c) AF3.....	59
Figure 48 Influence of NA on the flow curves of blanks AF1-AF3 .....	61
Figure 49 Effect of elevated strain rates on the strengthening of blanks AF1-AF3 obtained after 15 months of NA .....	62
Figure 50 Strengthening of blanks AF1-AF3 at elevated strain rates with respect to the quasi-static strain rate of 0.001 1/s.....	63
Figure 51 Effect of elevated strain rates on the flow curves of blank AF1-AF3 .....	64
Figure 52 Influence of NA on the formability characterized by maximum blankholder force using the A-Tool and constant forming velocities of (a) 10 mm/s and (b) 100 mm/s .....	65
Figure 53 Influence of BHF on the maximum drawing depth determined using the CS-Tool after 1 month of NA for the forming velocities of (a) 10 mm/s and (b) 100 mm/s .....	66
Figure 54 Change of maximum drawing depth $D_{max}$ during NA with respect to the maximum drawing depth determined after 1 month of NA for the forming velocities of (a) 10 mm/s and (b) 100 mm/s .....	69

Figure 55 The form of convex curved AF3 blank after positioning at the blankholder.....	70
Figure 56 (a) Schematic illustration of standard and reverse decoiling and (b) effect of blank alignment on the initial form of the blank .....	70
Figure 57 (a) Surface roughness $R_a$ and (b) lubricant amount of blanks AF1-AF4.....	71
Figure 58 Effect of blank alignment on the critical blankholder forces of blanks AF1-AF4 at the forming velocity of (a) 10 mm/s and (b) 100 mm/s .....	72
Figure 59 Effect of blank alignment on the maximum drawing depth of blanks AF1-AF4 determined using the CS-Tool, forming velocity of 10 mm/s and BHF of (a) 400 kN and (b) 600 kN .....	73
Figure 60 Actual maximum blankholder forces $F_{max}$ considering blank alignment for the forming velocity of (a) 10 mm/s and (b) 100 mm/s .....	74
Figure 61 Influence of NA on maximum bending angle of blanks (a) AF1, (b) AF2 and (c) AF3 .....	76
Figure 62 Influence of pre-straining on the maximum bending angle of blanks AF1, AF2 and AF3 .....	77
Figure 63 Influence of NA on the forming limits of blanks (a) AF1, (b) AF2 and (c) AF3 .....	78
Figure 64 Cracking of the Nakajima samples close to the clamping area.....	78
Figure 65 Exemplary illustration of CoF profiles as function of the sliding distance for blanks (a) AF1, (b) AF2, (c) AF3 and (d) AF4.....	79
Figure 66 (a) Average CoF as function of the initial contact pressure for blanks AF1-AF4 and	80
Figure 67 Dependency of CoF on contact pressure and sliding velocity in TriboForm friction models for blanks AF1-AF4.....	82
Figure 68 Experimentally and numerically determined FLDs using the A-Tool for blanks (a) AF1, (b) AF2, (c) AF3 and (d) AF4 after 3 months of NA.....	83
Figure 69 Behavior of blank material based on the induced strains for components formed using the A-Tool .....	84
Figure 70 Experimentally and numerically determined FLD using the CS-Tool for blanks (a) AF1, (b) AF2, (c) AF3 and (d) AF4 after 3 months of NA.....	85
Figure 71 Behavior of blank material based on the induced strains for components formed using the CS-Tool .....	86
Figure 72 Experimentally and numerically obtained forming forces for the components formed using the A-Tool.....	87
Figure 73 Experimentally and numerically obtained forming forces for the components formed using the CS-Tool.....	88
Figure 74 Section planes for the analysis of the thickness change at the components formed using (a) the A-Tool and (b) the CS-Tool.....	89
Figure 75 Thickness change at the cross-section of components formed using the A-Tool for blanks (a) AF1 (b) AF2 (c) AF3 and (d) AF4 .....	91
Figure 76 Thickness change at the cross-section of components formed using the A-Tool for blanks (a) AF1 (b) AF2 (c) AF3 and (d) AF4 .....	92
Figure 77 Height different between the experimentally and the numerically formed components using the A-Tool for blanks (a) AF1 (b) AF2 (c) AF3 and (d) AF4 .....	94
Figure 78 Height difference between the components formed using the CS-Tool in experiment and in numerical forming simulation with (a) the TF model and (b) the CF model .....	95

Figure 79 FLD of blanks AF3 formed using the A-Tool, forming velocity of 10 mm/s and BHF of 500 kN after NA of (a) 1 month, (b) 2 months (c) 3 months, (d) 6 months (a) 9 months, (b) 12 months, (c) 15 months and (d) 18 months .....96

Figure 80 Numerically determined FLD at the forming velocity of 100 mm/s for blanks (a) AF1, (b) AF2, (c) AF3 and (d) AF4 .....97

## List of tables

Table 1 Basic information about wrought aluminum alloys .....	5
Table 2 Main alloying elements of cast aluminum alloys .....	6
Table 3 The most frequent tempering conditions of aluminum alloys.....	6
Table 4 Literature overview about the influence of natural aging on properties of Al-Mg-Si alloys .....	10
Table 5 Geometrical parameters for configuration of plate bending setup .....	28
Table 6 Parameters for execution of plate bending test .....	28
Table 7 Typical chemical compositions of investigated blanks .....	33
Table 8 Process parameters for forming of the components used for validation of the numerical forming simulations at quasi-static strain rates .....	44
Table 9 Process parameters used for forming of the components for validation of the numerical forming simulations.....	46
Table 10 Parameters used for describing the logarithmic propagation of yield strength in RD ..	49
Table 11 Parameters used for describing the flow curves of blanks AF1-AF3 determined after 6 months of NA .....	59
Table 12 Influence of NA on the constants used for generating the flow curves .....	60